UNIVERSITY OF SOFIA "ST. KLIMENT OHRIDSKI"
FACULTY OF PHYSICS
ATOMIC PHYSICS DEPARTMENT

Martin Vasilev Makariev

Inclusive production of charged pions in proton-proton and proton-carbon collisions at 158 GeV/c beam momentum

Scientific Code 010305
Elementary particle and high energy physics

A thesis submitted for PhD degree

Supervisor: Assoc. Prof. Dr. L. Litov

Sofia, September 2006

Contents

Chapter 1

Introduction

1.1 Strong interactions and QCD

Till the middle of 20th century over a hundred strongly interacting particles were discovered. In 1964 Gell-Mann and Zweig proposed that these particles are not elementary but they consist of smaller objects called quarks. Scattering of high-energy leptons from hadrons confirmed that there are pointlike constituents in the hadrons identified with quarks and gluons – careers of strong force. Quarks appear in six types or flavours – u, d, s, c, b, t. In addition they have an internal three-valued quantum number called colour. The idea of colour symmetry was introduced to explain several problems: difference between experimental measurements and calculation of the $\pi^0 \rightarrow 2\gamma$ rate; relation between spin and statistics for Δ^{++}; hadron production in e^+e^- annihilation; τ lepton decay. All of this suggest that number of quark colours is $N_c = 3$.

Quantum Chromodynamics(QCD) is a theory of strong interaction. QCD is a gauge theory with an exact local SU(3) colour symmetry. The quark fields transform under a fundamental triplet representation of SU(3) group.

QCD Lagrangian can be written as:

$$\mathcal{L}_{QCD} = \sum_{k}^{n_f} \overline{q}_k (i\gamma^\mu D_\mu - m_k) q_k - \frac{1}{2} tr G_{\mu\nu} G^{\mu\nu}, \tag{1.1}$$

where the covariant derivative D_μ and gluon field tensor $G_{\mu\nu}$ have the form:

$$D_\mu = \partial_\mu - igA_\mu \tag{1.2}$$

$$G_{\mu\nu} = \partial_\mu A_\nu - \partial_\nu A_\mu - ig[A_\mu, A_\nu] \tag{1.3}$$

$$A_\mu = \sum_{a=1}^{8} A_\mu^a \lambda_a / 2, \tag{1.4}$$

where λ_a are Gell-Mann matrices (a=1,...,8), A_μ^a are gauge boson fields and q_k are quark colour triplets.

QCD is Quantum Field Theory and analytical calculation are made using perturbative methods, so called perturbative Quantum Chromodynamics (pQCD). A typical parameter used in pQCD is the coupling constant g. The calculations with Lagrangian from Eq. 1.1 lead to divergences due to the fact that Eq. 1.1 contains bare fields. These fields as well as the coupling constant have to be redefined which is made in such a way that divergent part is subtracted out. This procedure is referred as a renormalization. The

renormalization is applied at a given momentum scale μ which can be chosen arbitrary. Physical quantities should not depend on momentum scale. The invariance under the choice of momentum scale form a group, called renormalization group. As a result the coupling constant is momentum dependent, known as a running coupling constant. It is common to introduce $\alpha_s(Q^2) = \overline{g}^2(t)/4\pi$, with $\overline{g}$ predefined coupling constant and t renormalization group parameter. The running strong coupling constant in one loop approximation can be expressed as:

$$\alpha_s(Q^2) = \frac{4\pi}{(11 - \frac{2}{3}n_f)\ln\frac{Q^2}{\Lambda^2}}, \tag{1.5}$$

where n_f is the number of quark flavours. Here α_s depends on one parameter Λ which is measured experimentally and determined to be $\Lambda \approx 200$ MeV. This formula is perturbative and it breaks down for large couplings. Nevertheless the parameter Λ is useful measure for energy scale where the strong coupling constant become large. It is called the QCD scale parameter. If the number of flavours $n_f \leq 16$ (we believe that $\mathrm{n}_f = 6$) than α_s will decrease with increasing of momentum Q and $\alpha_s \to 0$ as $Q \to \infty$ (this corresponds to small distances) which is known as asymptotic freedom. This property of coupling constant give a possibility to use pQCD at high-energy processes. This domain is known as hard hadronic physics. At low momentum transfer perturbative methods are not applicable. This domain is known as soft hadronic physics.

Calculation of low-energy processes require non-perturbative methods. This can be performed by numerical techniques, where continuous space-time points are replaced with discrete coordinates, the method called lattice QCD.

1.2 Soft hadronic physics

Perturbative methods are not applicable at low momentum transfer processes, since the coupling constant α is too large. A number of phenomenological models have been developed in order to study soft hadronic processes. A more recent approach is based on the parton model, motivated by its success in lepton-hadron deep inelastic scattering.

In general the hadron-hadron interaction is assumed to proceeds in two steps. In first step a quark from one of the hadron interacts with a quark from the other hadron. In the second step the "hadron reminder" fragments into final-state hadrons. The fragmentation function is the same as in e^+e^- and lepton-hadron interactions. A review can be found in [5].

Phenomenological models have a number of free parameters which have to be determined from the measured data.

In the lack of quantitative theoretical predictions, an attempt is made to look at a model independent way of improving understanding of the underlying production mechanism. This requires to exploit all possible types of hadronic interactions, ranging from elementary hadron-hadron (h+h) through hadron-nucleus (h+A) to nucleus-nucleus (A+A) collisions, combined with a large phase space coverage and particle identification.

Multiparticle final states encountered in hadronic interaction form a multidimensional phase space. An inclusive single particle production covers only the simplest surface of the multidimensional phase space. This type of reaction has two independent momentum components. As such are chosen transverse momentum p_T and reduced longitudinal variable Feynman x x_F, defined as:

$$x_F = \frac{p_L}{\sqrt{s}/2}, \tag{1.6}$$

where p_L is longitudinal momentum in the nucleon-nucleon rest frame and s is invariant mass squared of the nucleons.

In the thesis an inclusive production of charged pions in p+p and p+C collisions is examined:

$$\begin{aligned} p + p &\rightarrow \pi^{\pm} + X \\ p + C &\rightarrow \pi^{\pm} + X. \end{aligned} \tag{1.7}$$

Hadron-nucleus interactions give an access to multiple hadronic collision processes. They also give an important link between h+h reactions and A+A interactions. In fact any model independent attempt for understanding the latter processes has to be based on the reference to more elementary h+h and h+A interactions. The light isoscalar nucleus ^{12}C allows to study the evolution from elementary to nuclear interactions for a small number of projectile collisions. In contrast to symmetric p+p reaction p+C is forward-backward asymmetric which necessitates in principle a full phase space coverage.

1.3 Experimental situation

There are several p+p experiments [20–32] which have published particle yields in the range of beam momentum from 100 to 400 GeV/c. These experiments can be divided tentatively in three groups.

The first one concerns bubble chamber experiments where the data samples are very limited with not more than 10 000 events and without particle identification.

The second group are spectrometer experiments. They are characterized with small phase space coverage as the spectrometer measures particles produced at fixed angle at the given momentum. They have a particle identification.

The third group are solid angle spectrometers which feature large phase space coverage and particle identification. Unfortunately, very few of their result have been published.

Only the experiments from the second group give results on double differential pion cross section:

$$\frac{d^2\sigma}{dx_F dp_T^2}. \tag{1.8}$$

The phase space coverage of existing measurements of double differential invariant cross section of identified pions at NA49 energy range is illustrated in Fig. 1.1a. It is seen from the plot that two Fermilab experiments [20, 21] have a limited phase space coverage and the data are very scarce or absent completely in the regions of p_T below 0.3 GeV/c and above 1 GeV/c as well as at x_F below 0.2. In addition to this the experiment [20], as will be shown in Sect. 5.5.1, suffers from large systematic errors which makes it unusable for quantitative reference.

The respective NA49 coverage is presented in Fig. 1.1b. The large acceptance allows for the first time a detailed study at low p_T and low x_F ranges. The p_T limit of 2 GeV/c is entirely due to the decreasing statistics.

Additional data from ISR [50] – [52], measured in $\sqrt{s}$ range from 23 to 63 GeV, where used for comparison in the high x_F range where Feynman scaling is expected to hold.

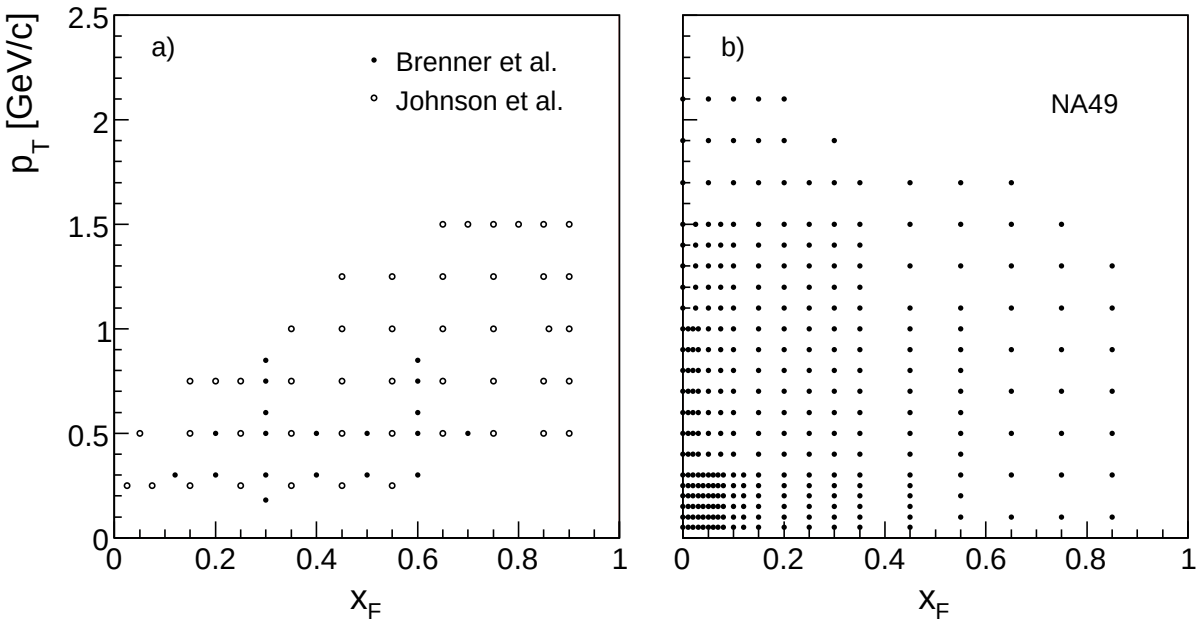

Figure 1.1: Phase space coverage of existing data in p+p: a) Fermilab, b) NA49

In p+C case the situation is even more restricted. There are two Fermilab experiments [35, 36] which give the double differential invariant cross section. The first one covers region in the far forward hemisphere, the second one measures at fixed angles in the far backward region, yielding an important information about the intranuclear cascading. The situation is depicted in Fig. 1.2a which shows the absence of data in the central region -0.2 $< x_F <$ 0.3.

The new NA49 results permit to fill this gap to a large extent, as shown in Fig. 1.2b.

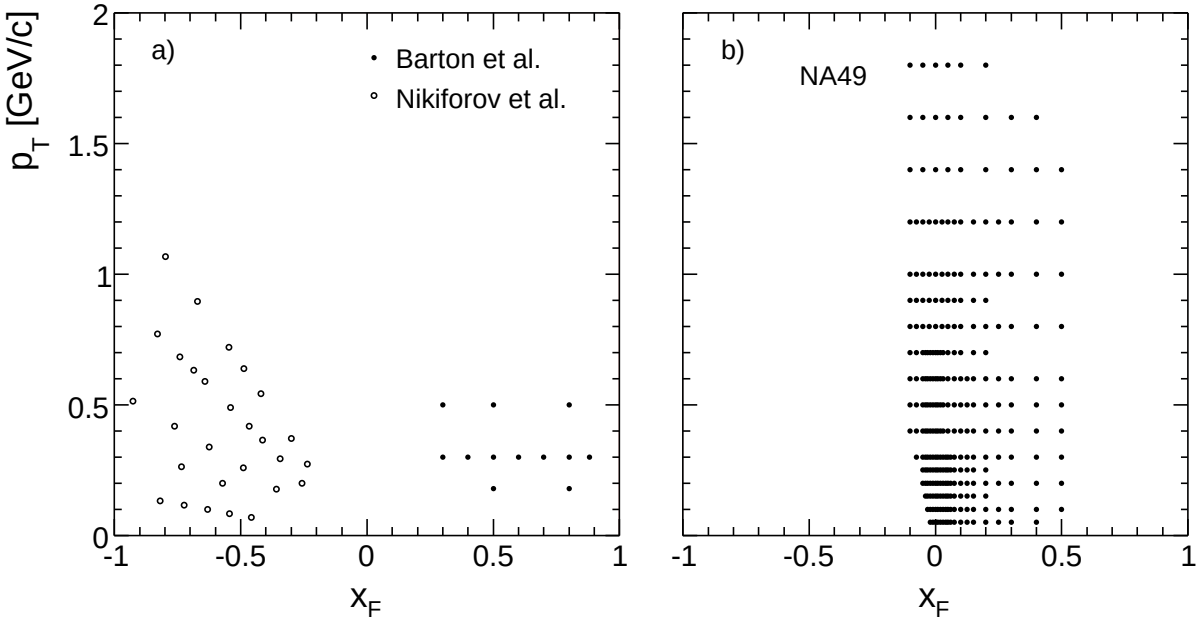

Figure 1.2: Phase space coverage of existing data in p+C: a) Fermilab, b) NA49

Again as in the p+p case they are limited to $p_T < 1.8$ GeV/c and to $x_F < 0.5$ essentially by the modest event statistics. Due to the asymmetric nature of p+C interaction a special effort was invested in exploring the backward hemisphere up to the acceptance limit of the detector. A p_T dependent cut at $x_F >$ -0.1 is imposed both by the NA49 acceptance and by the particle identification via ionization energy loss. Nevertheless an inspection of the important cross-over region between projectile and target hemispheres is possible.

1.4 Capabilities of NA49 experiment

The NA49 experiment has a number of features which allows to make a sizable improvement in the quality of data compared to the previous measurements:

- *Variety of projectiles and targets.* A large set of reactions is needed to observe evolution of physics quantities starting from h+h interaction to more complex system. The NA49 experiment has obtained data with different projectiles and targets, covering h+h, h+A and A+A collisions, all of this performed with same detector.
- *Large momentum phase space coverage.* A large momentum phase space coverage can provide a detailed information about particle production. Even more, studies beyond inclusive particle production like particle correlations, resonance spectroscopy are not possible with a small arm spectrometer. The detector has covered the full forward hemisphere and a small part of the backward region.
- *Particle identification.* Particle identification plays a significant role for obtaining of inclusive particle spectra as well as for correlation measurements. The identification is achieved by measurement of the specific energy loss of the particles.
- *High statistics.* Detailed studies require high statistics samples of about several million events.
- *Centrality control.* More complex reactions, as h+A and A+A, has an additional parameter, namely the centrality of the collision (or impact parameter). The final state changes considerably with the centrality, therefore nuclear collisions have to be studied against this parameter.

1.5 Outline of the thesis

This thesis is organized as follows.

Chapter 2 contains the description of the NA49 experiment.

Chapter 3 presents the data samples obtained by NA49 and phase space coverage of the detector. The event and track selection criteria and particle identification method are discussed.

In Chapter 4 the total inelastic, trigger and invariant double differential cross section are defined. The corrections applied to the measured cross sections and overview of the systematic error are given.

The final double differential and p_T integrated cross sections are presented and tabulated in Chapter 5 and Chapter 6, respectively. A detailed comparison with previous measurements is made.

Chapter 7 deals with p_T integrated x_F distributions of pion production in p+C collision in relation to p+p interactions. The p+p as well as p+C data are discussed in the

framework of simple two-component picture. The intranuclear cascading contribution in p+C collisions is quantified.

In Chapter 8 the p_T behaviour of the double differential cross section in p+C collisions is discussed again in relation to p+p interactions.

Finally, Chapter 9 and Chapter 10 give a summary of results.

The results presented in this thesis are published in [1–3].

Chapter 2

The NA49 experiment

The NA49 is a fix target experiment situated in North Area at the CERN SPS accelerator. It was designed for studying h+h, h+A as well as A+A reactions. The final state hadrons produced can vary typically from 5-7 in $p(\pi)+p$ interactions up to 3000 in central Pb+Pb collisions. It is aimed to produce large data samples for each reaction type with the same apparatus which provide at same time wide acceptance coverage and complete particle identification. In addition the extreme particle multiplicities in heavy ion collisions require extraordinary multi-particle pattern recognition and separation capabilities.

To fulfill these requirements the NA49 experiment uses a set of Time Projection Chambers (TPC). Schematic top view of the detector system is shown in Fig. 2.1. The NA49 tracking system consists of four large volume TPCs. The TPC system provides superior multi-particle pattern recognition and adequate space resolution combined with energy loss measurement.Two of the TPCs (VTPC1 and VTPC2) are placed inside superconducting dipole magnets ensuring momentum measurement. The other two (MTPC L,MTPC R) are placed behind the magnets offering a large volume for tracking.

The NA49 detector system includes also three proportional chambers (BPD 1,2,3) for the beam transverse coordinate determination and a set of scintillator counters (S1,S2,V0,S4) assigning the trigger. A small TPC (GTPC), see Fig. 2.2, placed between VTPC1 and VTPC2 which together with two strip-readout proportional chambers (VPC1 and VPC2), also shown in Fig. 2.2, extend the acceptance up to kinematic limit.

Four walls of Time Of Flight (TOF) scintillator detectors placed behind MTPCs and two arrays of PESTOF counters placed between two magnets ensure independent method of particle identification in the region of minimum ionization, $\beta\gamma \sim 3$.

Two downstream calorimeters, Ring and Veto calorimeter, complete particle detection coverage and serve as a trigger in ion collisions.

2.1 Beam detectors and interaction trigger

Protons from SPS with 400 GeV/c impinged on 10 cm long Be target create a secondary beam, selected at 158 GeV/c momentum. The beam momentum resolution is 0.13%. This secondary beam contains roughly 65% protons which are identified with a CEDAR [6] Ring Čerenkov counter. Upstream scintillators and Beam Position Detectors provide precise timing, charge and position measurement before the proton beam interacts with the target.

Two scintillator counters S1 (5 mm thick) and S2 (2 mm thick) provide timing and beam definition. A ring-shaped veto counter V0 reducing the background from upstream

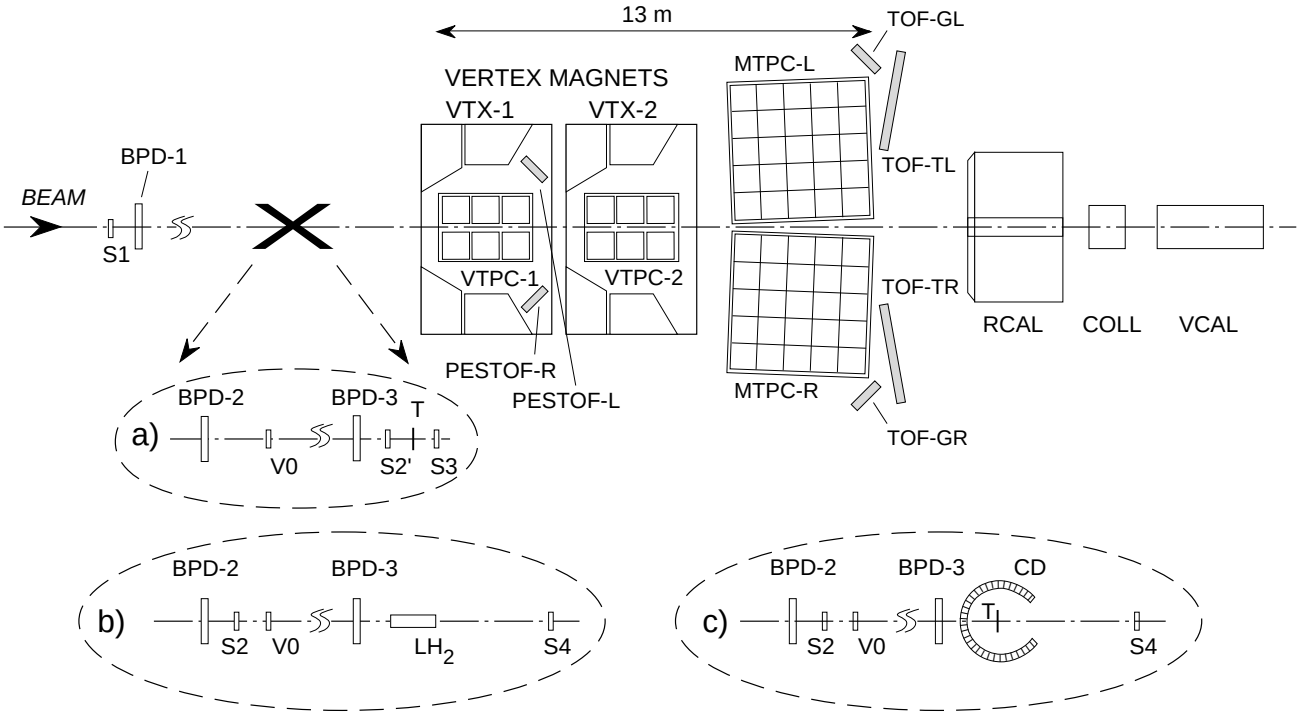

Figure 2.1: The NA49 experiment set-up with different beam definitions and target arrangements: a) A+A, b) h+h, c) h+A

interaction. The beam is defined as $B = C \cdot S1 \cdot S2 \cdot \overline{V0}$. Interaction in the target are selected by anti-coincidence of the beam and a small scintillator S4, with 2 cm diameter placed between the two magnets, $B \cdot \overline{S4}$.

The transverse position of the beam is measured by three small (3×3 cm) proportional chambers with cathode strip readout. They consist of two orthogonal sense wire planes sandwiched between three cathode planes. The 15 μm tungsten wires with 2 mm pitch give 170 μm precision in beam position extrapolated to the target.

2.2 Targets

In p+p interactions a liquid hydrogen target is used while in p+C collisions a graphite cylindrical shaped solid target is employed. Specifications of the targets are given in Table 2.1.

target	proton	carbon
length [cm]	20.29	0.7
diameter [cm]	3	0.6
density [g/cm^3]	0.0707	1.83
atomic mass [g/mol]	1.0079	12.0107
target interaction length [%]	2.8	1.5

Table 2.1: Specifications of the targets

2.3 Grey proton detector

The target in p+A interactions is housed in a grey proton detector which measures the number of "grey" target protons in the momentum range from 0.15 to 1 GeV/c. The grey proton detector has been developed for on-line centrality control of the collision. It is known from emulsion and bubble chamber experiments [7, 8] that this number is correlated with the impact parameter. A more detailed discussion of the physics of grey protons can be found in [9, 10].

This detector is a cylindrical proportional counter of 12 cm diameter which surrounds the target and has a window in forward direction corresponding to the acceptance of the spectrometer inside polar angles of $\pm 45°$. Its surface is subdivided into 256 pads which provides ample granularity for the counting of typically less than 8 grey protons measured per event in light ion applications. A thin (200 μm) copper sheet on the inner surface absorbs nuclear fragments by range, and an electronics threshold placed at 1.5 times the minimum ionization deposit cuts high momentum particles as the grey protons are placed high on the $1/\beta^2$ branch of the Bethe-Bloch energy loss distribution. Grey protons in the momentum range from 0.15 to 1.2 GeV/c reconstructed and identified inside the spectrometer acceptance are added to the number measured in the centrality detector.

Due to the very short available data taking period and to the sharp drop of the event yield as a function of the number of grey protons (less than 30% of all events have a measured grey proton), the on-line triggering capability on grey protons available in the NA49 trigger system could not be used in this analysis.

2.4 The TPC system

The NA49 TPC system is the major part of the NA49 detector. It features precise coordinate measurement and specific energy loss determination. One example of event is shown in Fig. 2.2 where the dots are measured space points and lines represent fitted tracks.

Geometrical dimensions of the TPCs are given in Table 2.2.

dimensions [cm]	VTPC-1,2	MTPC-L/R	GTPC
width	200	390	81.5
length	250	390	30
height	98	180	70
drift length	66.6	111.7	59

Table 2.2: Geometrical dimensions of the TPCs

2.4.1 Basic principles of TPC

A TPC consists of two parts – sensitive volume and readout chambers. The TPC volume is filled with gas. When a high energy charged particle traverses through the sensitive volume, it ionizes the gas atoms along its trajectory. Electrons created by the ionization drift to the top of the TPC influenced by a homogeneous electric field of order 150-200 V/cm and reach the readout chamber, see Fig. 2.4. In the readout chamber the electrons create an avalanche with gain of order 10^4. This induces a voltage pulse on a segmented cathode plane from which the signal is read out.

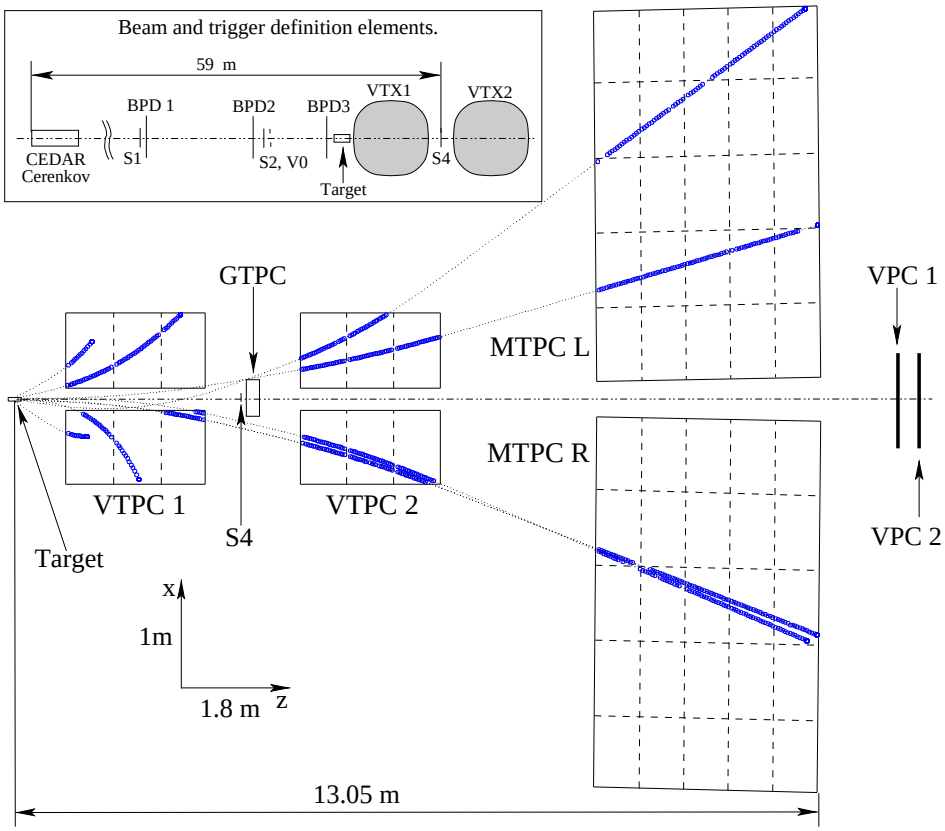

Figure 2.2: NA49 detector layout and a typical p+p event

The two horizontal coordinates are measured by the location of the signal in cathode plane, the third by the drift time of electrons. In this way the measured trajectory of the particle in magnetic field (VTPC-1,2) allows for momentum determination and positive and negative particle separation. The specific energy loss is determined by the charge deposit on the cathode plane ensuring identification of the charged particles.

2.4.2 Alignment and space position

The use of the same detector for the complete range of interactions implies a separation of the sensitive volumes with respect to the beam trajectory. Otherwise, in the case of heavy ion collisions non-interacting beam ions would create excessive chamber loads. The corresponding acceptance loss in low p_T region and large x_F has been remedied by introduction of a small TPC (GTPC), placed on the beam line between the two magnets which is used only with hadron beams.

The space position of the TPC system with relation to the SPS beam coordinates is determined to better than 200 μm accuracy, by optical methods. The consistency of the measurement is checked with muon tracks and multi-target runs.

2.4.3 Gases

The TPCs volume is filled with gas mixture of Ne/CO_2 (90/10) for the VTPCs and GTPC and $Ar/CH_4/CO_2$ (90/5/5) for the MTPCs. These compositions have been chosen taking into account diffusion coefficients, drift velocities and an electron attachment. Diffusion coefficients have been measured to be 200 $\mu m/\sqrt{cm}$ and 270 $\mu m/\sqrt{cm}$ for Ne and Ar

mixture respectively. This corresponds to drift velocities of 1.4 cm/μs in the VTPCs (E = 200 V/cm) and 2.4 cm/μs in MTPCs (E = 175 V/cm). The electron attachment in VTPCs is bigger due to CO_2 content. The attachment losses of 1.2% and 0.6% per ppm of oxygen over the 50 μs drift time have been measured in the two types of detectors. The gas purity and composition is controlled by a gas system. The temperature is stabilized to better than 0.1°C.

2.4.4 Field cages, gas envelopes, support plates

The mechanical construction is designed in such a way to have a minimum amount of material crossed by the particles, a homogeneous electric field, separation of the field cage and gas envelope etc. Basic elements of the field cage are aluminazed Mylar strips of 25 μm thickness and 1/2 inch width. They are suspended on ceramic tubes placed in the corners of the rectangular field cages, with a distance of 2 mm between strip edges, creating a homogeneous electric field. The High Voltage planes are realized using the same type of strips. Schematic drawing of the field cage of the VTPC is shown in Fig. 2.3.

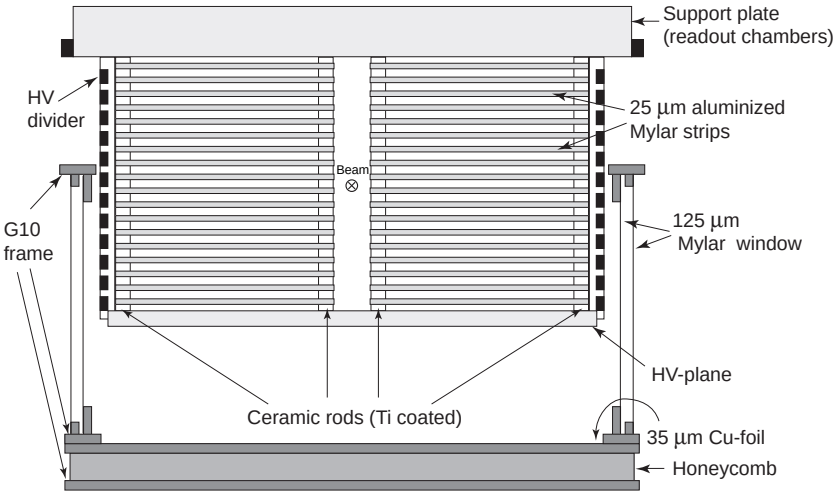

Figure 2.3: Schematic drawing of one of the VTPCs

The gas envelopes are made of double layer of 125 μm Mylar foil glued to a double frame system made of 6 mm thick fiberglass-epoxy. The volume between layers is filled with Nitrogen in order to minimize gas impurity diffusion. The gas envelopes are completely separated from the drift field structure.

The field cages and gas envelopes are carried by support plates which also house the readout chambers.

2.4.5 Readout chambers

The NA49 TPC system has 62 readout proportional chambers each with a surface of 72×72 cm^2. The readout chambers consist of gating grid, cathode plane (Frisch grid), sense and field wire plane and segmented pad plane. Electrons liberated by the charged particle traverse sensitive volume of the TPC driven by the electric field E (Fig. 2.4) reach the gating grid. The gating grid serves to stop the electrons if there is no trigger signal and not to leave the ions produced during the electron gain in the readout chamber, in the case of trigger signal, to enter into the sensitive volume of the TPC. Above the gating

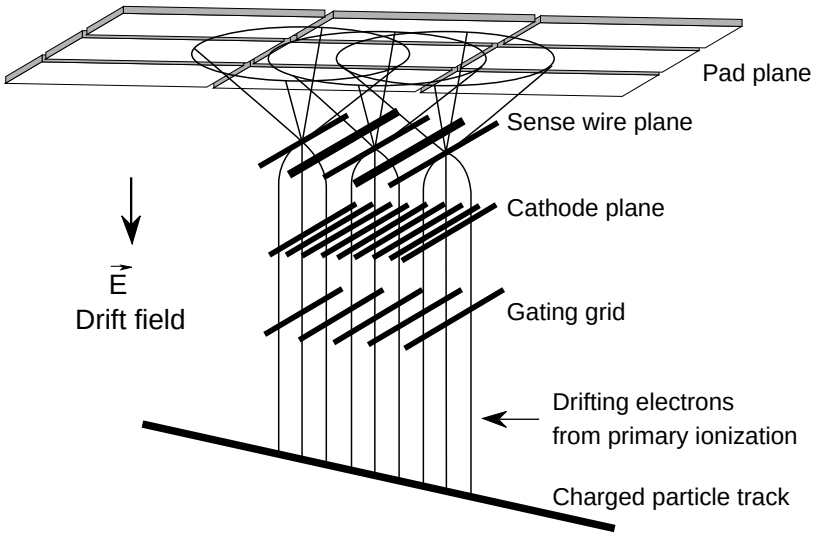

Figure 2.4: Schematic layout of the TPC readout chambers

grid is located the cathode plane which is on the ground potential followed by the sense wires interspaced by the field (zero potential) wires. The sense wires are connected to +1200 V potential and create an electron avalanche. The induced signal on the pad plane is read out. The pads are arranged in rows perpendicular to the beam direction. The numbers of rows are 72 for the VTPCs, 90 for the MTPCs and 7 for the GTPC. The pads are tilted with respect to the beam from 0° to 55° depending on the expected direction of the secondary tracks.

The gas gain is $2{\cdot}10^4$ and $5{\cdot}10^3$ in VTPCs and MTPCs, respectively. Sizes of the elements of the readout chambers are presented in Table 2.3.

dimensions [mm]	VTPC-1	VTPC-2	MTPC-L/R	GTPC	wire material
pad length	16, 28	28	40	28	
pad width	3.5	3.5	3.6, 5.5	3.5	
pad angles	12-55°	3-20°	0°, 15°	0°	
sense wire diam.	0.02	0.02	0.02	0.02	W-Re (gold plated)
sense wire spacing	4	4	4	4	
field wire diam.	0.125	0.125	0.125	0.125	Cu-Be (gold plated)
field wire spacing	4	4	4	4	
Frisch grid wire diam.	0.075	0.075	0.075	0.075	Cu-Be
Frisch grid wire spacing	1	1	1	1	
gating grid wire diam.	0.075	0.075	0.075	0.075	Cu-Be
gating grid wire spacing	1	1	2	1	

Table 2.3: Geometrical dimensions of the readout chambers elements

2.4.6 Electronics and data acquisition

The NA49 readout system comprises 182 000 pads. The signal from each pad is taken by the front-end electronics, connected on the back plane of the readout chambers. The signal is amplified and shaped into Gaussian wave form with 240 ns FWHM. The analog signal is time-sampled by Switched Capacitor Array with frequency of 10 MHz into 512 time

buckets over the maximum drift time of 50 μs. The following digitization is accomplished by the Wilkinson type ADC wit 9 bit resolution. The digital signal is processed in a VME based system which perform noise rejection and zero suppression cutting out the channels with entries below the threshold. In this way the initial event size of 100 MB is compressed to 1.5 MB in p+p reaction and recorded on a tape recorder which can operate at a transfer rate up to 16 MB/s. The event recording rate of 25-30 per SPS spill of 2.4 s in 14 s cycles is realized.

The calibration of the electronics together with the gas gain in the readout chambers is done by injecting the radioactive ^{83}Kr gas [13].

2.4.7 Tracking and event reconstruction

The NA49 event reconstruction proceeds through several steps:

- *Cluster finding.* Two-dimensional clusters are formed by grouping the information from neighboring pads and time buckets in each row. The position of each cluster is taken by the center of gravity over the charged distribution.
- *Local tracks construction.* The clusters in each TPC separately are connected into local tracks. Maximum number of clusters (or points) possible are 72 for each VTPC, 90 for MTPCs and 7 for GTPC.
- *Global tracks construction.* The local tracks in different TPCs are merged into global tracks. For global tracks construction and momentum fitting a minimum of 8 clusters are requested.
- *Main vertex fitting.* All global tracks found in the event are traced back to the target position searching for the closest approach point.
- *Momentum determination.* After a successful reconstruction of the main vertex a momentum fitting is performed including also tracks which have recorded cluster only out of magnetic field.

The space resolution has been measured using muon tracks. A comparison of residual distribution with and without magnetic field has shown that overall precision is of about $\pm$200 μm in both horizontal and vertical direction. The achieved space resolution in MTPCs varies from 120 μm to 270 μm depending on the drift length, with a mean value of 210 μm compatible with the upper result.

The momentum resolution depends on the coordinate resolution, track length and number of measured points. Typical values are $\Delta p/p^2 = 7.0{\cdot}10^{-4}$ (GeV/c)$^{-1}$ for tracks passing through VTPC-1 only (momentum range 0.5-8 GeV/c) and $\Delta p/p^2 = 0.3{\cdot}10^{-4}$ (GeV/c)$^{-1}$ for tracks passing through VTPC-2 and MTPC (momentum range 4-100 GeV/c).

The resolution of main vertex in transverse direction is constraint by the beam position measurement in BPDs (Fig. 2.1) to precision of 170 μm. Longitudinal position of the main vertex is found by an extrapolation of the secondary tracks to about 80 cm upstream of the VTPC1. It should be restricted by the target length. However in low multiplicity events the reconstruction programme can shift fitted vertex far upstream or downstream of the target.

2.4.8 Tracking efficiency

There are two limiting conditions which could lead to track losses in the TPCs, namely high track density regions (Pb+Pb) and "wrong" side tracks with respect to the magnetic field. Tracks with a sizable transverse momentum can reach "wrong" hemisphere of charge. These tracks have large crossing angle with respect to the pad direction which tends to split clusters due to low charge deposit per pad. The corresponding losses are concentrated in the low momentum region where the acceptance of the detector is low anyway.

In h+h and h+A reaction the tracking efficiency is almost 100% with losses being negligible. This is guaranteed by very high local efficiency for cluster formation with a losses below the permille level.

2.5 Time of flight system

The Time of flight (TOF) system covers the lab momentum region from 2 to 12 GeV/c. It has a time resolution of order of 70 ps which allows for separation of protons from kaons and pions in the entire range.

The TOF system consists of three subsystems:

- A pixel scintillator system placed behind the MTPCs (TOF-TL and TOF-TR in Fig. 2.1). The two walls cover total surface of 4.4 m^2 and contain 1782 individual scintillators.
- A grid scintillator system placed at larger angles behind MTPCs (TOF-GL and TOF-GR in Fig. 2.1). The total surface of the walls is 1.24 m^2 and comprise 186 scintillation detectors.
- A system of PESTOF counters installed between the two magnets.

2.6 Ring calorimeter

The Ring Calorimeter is placed 18 m downstream of the interaction target. It is used to measure the neutral particle production in the projectile hemisphere in p+p and p+A collisions.

The calorimeter has a cylinder shape with inner bore of 56 cm and outer diameter of 3 m. It consists of two sections. In the front a lead/scintillator sandwich of 16 radiation lengths measures the electromagnetic particles followed by the hadron part made of 6 interaction length iron/scintillator sandwich. The sensitive area is subdivided into ten radial rings and 24 azimuthal sectors, forming 240 cells. The energy resolution can be parametrized by $\sigma(\mathrm{E})/\mathrm{E} = 1.2/\sqrt{\mathrm{E(GeV)}}$.

2.7 Veto proportional chambers

The NA49 detector was supplemented with two proportional chambers, Fig. 2.2, placed behind the MTPCs, covering the gap between them. They are designed to extend the charged particle detection in the very forward region up to the kinematic limit.

The chambers are realized with cathode strip read out. Each of them consists of horizontal anode wires capacitively coupled to the two cathode planes. The strips in

cathode planes are inclined at 60° in opposite directions. The intersection of the firing strips defines the position of the hit.

The position resolution was tested with the TPC tracks which cross through the VPCs. It was measured to be 2 mm in vertical and 2.7 mm in horizontal direction. The efficiency was found to be above 99% from data taken with a muon trigger.

Together with the GTPC the VPCs provide a precise momentum determination of the fast forward charged particle and in the same time they are used as a veto counter separating in this way the charged from neutral particle measured in the Ring Calorimeter.

Chapter 3

Data analysis

3.1 Selection

3.1.1 Event selection

About 18% of p+p and 30% of p+C events come from interactions of the beam with non-target materials. In both reactions alternate runs with full and empty target were performed and used to reduce these background events with suitable off-line cuts. These cuts concern the beam position close to the target and longitudinal position of the interaction vertex.

The beam position is measured by the three BPDs, see Fig. 2.1. The three independent measurements of the beam over 30 m distance are required to be collinear in both transverse coordinates by imposing that the extrapolation from BPD1 and BPD2 to BPD3 coincides with the measured beam position in BPD3. This is shown in Fig. 3.1 and only events which fall between the two lines are accepted.

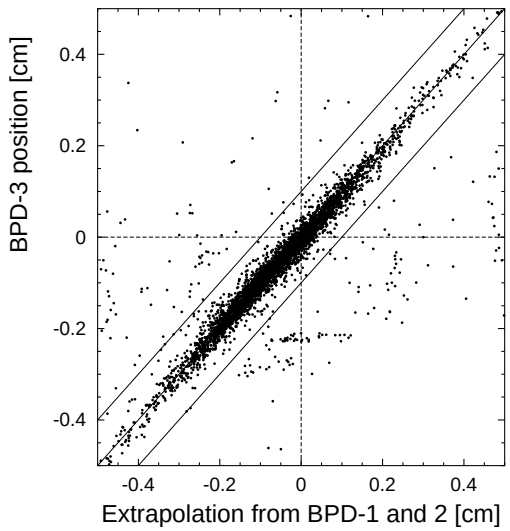

Figure 3.1: Beam position at BPD3 versus extrapolated position from BPD1 and BPD2 to BPD3

The precision of the reconstructed longitudinal position of the interaction point depends strongly on the event multiplicity and configuration. A cut on longitudinal position of the vertex is performed taking into account the number of tracks in the event which

cross a sizable part of the TPC system. Short tracks are not used for vertex determination. Cuts are placed in such a way that no target events are rejected. The normalized distribution of z coordinate of the vertex from full and empty target for different multiplicities is presented in Fig. 3.2.

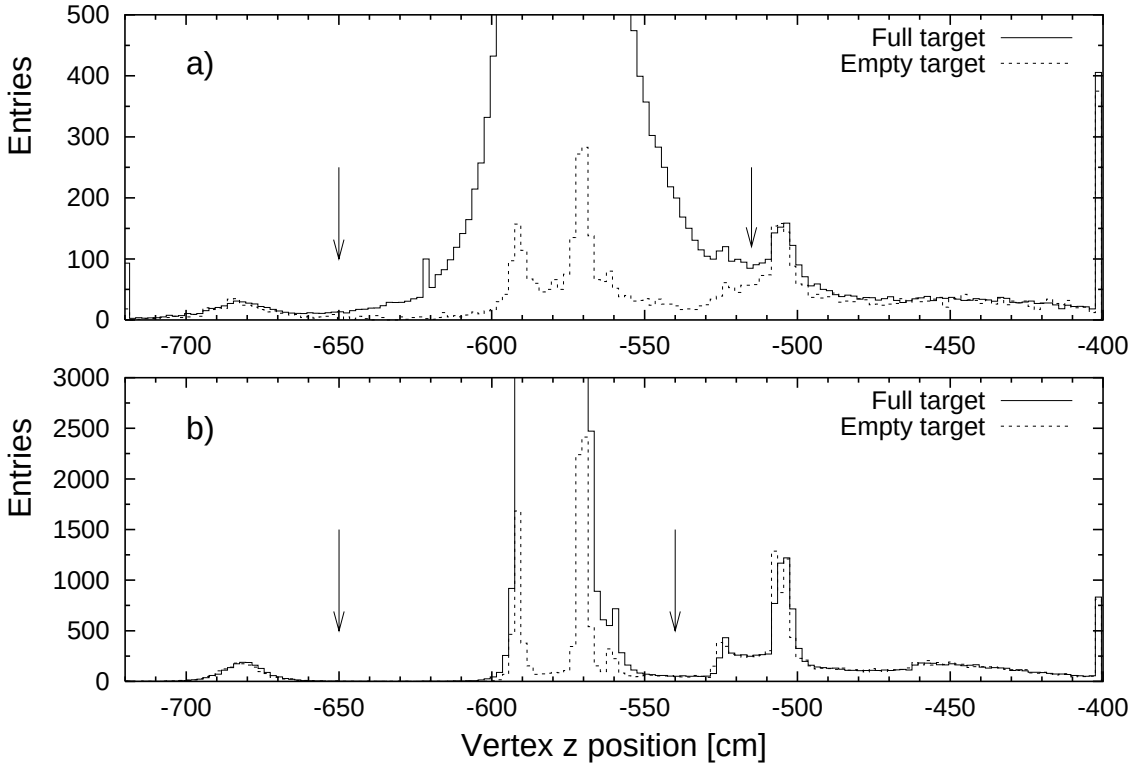

Figure 3.2: Normalized vertex distributions from full (full line) and empty (dashed line) target events with selected track multiplicity a) one and b) five and more. The z-vertex position cuts are indicated with arrows. The walls of the vessel which contains the liquid hydrogen at $\sim$ -590 cm and $\sim$ -570 cm and the entrance of VTPC1 at $\sim$ -505 are clearly visible in the empty target distributions

These cuts decrease the background to 9% and 16% in p+p and p+C interactions, respectively. Most of the remaining empty target contribution is due to empty events where no track in the acceptance of the TPC system have been registered and the other part are low multiplicity events where the vertex fitting failed. Contribution from such event will be treated as a small correction to the particle yields, see Sect.4.4.1.

The statistics available after event selection is $4.8{\cdot}10^6$ events in p+p obtained in three running periods in 1999, 2000, 2002 and $3.8{\cdot}10^5$ events in p+C taken in one running period in 2002. The number of events analyzed are given in Table 3.1.

3.1.2 Track selection

A track in the NA49 detector is defined by the ensemble of clusters (points) in three dimensions that a charged particle leaves in the effective volume of the TPC system. These clusters have a typical spacing in track direction of about 3 cm in the VTPCs and 4 cm in the MTPC regions.

Regions of 100% acceptance can be readily defined in each kinematic bin Δx_F, Δp_T,

reaction type	Year	Events taken		Events after selection	
		Full target	Empty target	Full target	Empty target
p+p	1999	1 211	41.2	906	13.7
	2000	2 648	47.8	2 049	16.9
	2002	2 508	69.0	1 814	21.8
	total	6 367	158.0	4 769	52.4
p+C	2002	535.7	31.2	377.6	11.8

Table 3.1: The event statistics, given in 10^3

and the azimuthal angle wedge $\Delta\Phi$ by inspecting the distribution of points per track in comparison to the expected value. This is achieved by adjusting $\Delta\Phi$ such that this distribution does not show tails beyond a well-defined average. This gives at the same time an experimental handle to stay away from edge regions which show a drop of the number of points.

In addition a minimum of 30 points for each track is required in order to ensure a desired quality of particle identification, see Sect.3.3. This corresponds to a track length of about 90 cm in the detector. The only exception is the high momentum tracks which pass through the GTPC and VPCs and can leave maximum 9 points (7 in the GTPC and 2 in the VPCs) where no particle identification is reliable. In Fig. 3.3 are presented a number of points distributions in a typical analysis bin.

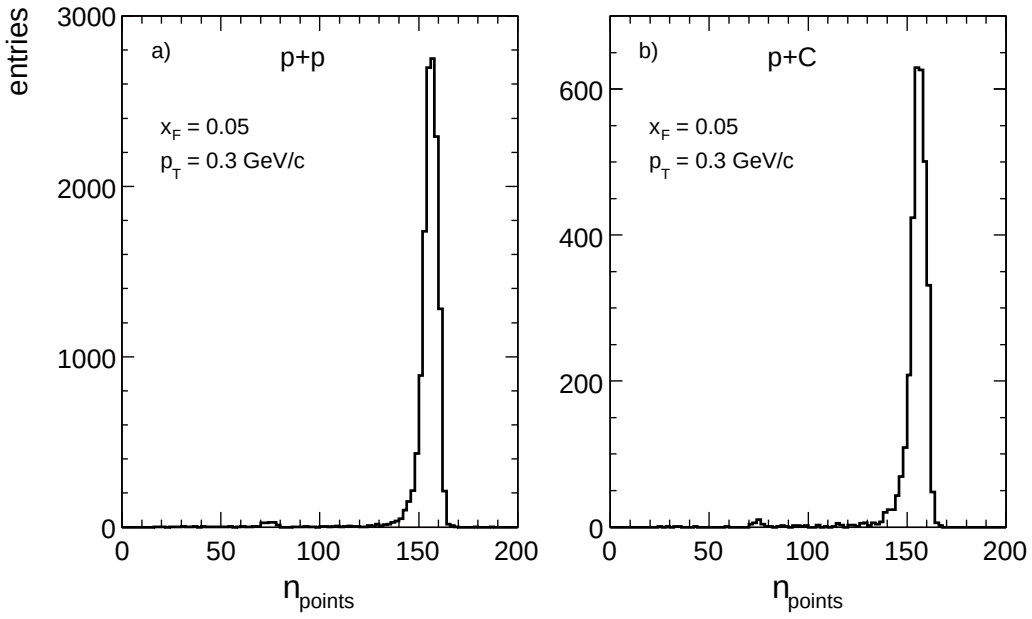

Figure 3.3: Number of points distribution measured at $x_F = 0.05$ and $p_T = 0.3$ GeV/c for a) p+p and b) p+C collisions

The cut on the number of points is co-ordinated with the $\Delta\phi$ wedge in such a way that there is no track losses. The only possibility of track losses are weak decays of pions or hadronic interactions with the detector gas where less than 30 points in the tracks are left. It has been verified by the eye-scans that such shortened tracks appeared by either a decay or a hadronic interaction. In the first case an additional track emerges at an angle with respect to the primary track. In the second case several tracks are visible pointing

at the well defined interaction vertex where the pion disappears. A correction for such cases is applied, see Sect. 4.4.5.

3.2 Binning schemes and Acceptance

Pions produced in p+p and p+C reactions have similar configurations in phase space and similar binning schemes in the (x_F,p_T) plane have been used. The only difference arises from the lower statistics in p+C, which forces us to exclude from analysis high p_T and x_F regions.

The binning schemes have been chosen taking into account several aspects:

- Optimum exploitation of available statistics.
- Definition of bin centers at consistent values of x_F and p_T. This will help a comparison to other data and other reaction types.
- Compliance with the structure of the inclusive cross section. In the regions where the cross section changes rapidly the bins are put densely.
- A relatively small bin in total laboratory momentum for optimum extraction of specific energy loss for particle identification. As the ionization losses depend on momentum in lab system, increasing the lab momentum range of the bin will lead to widening of the dE/dx distribution and worsening of the particle type separation capabilities.
- Avoidance of overlap and minimization of lost regions.

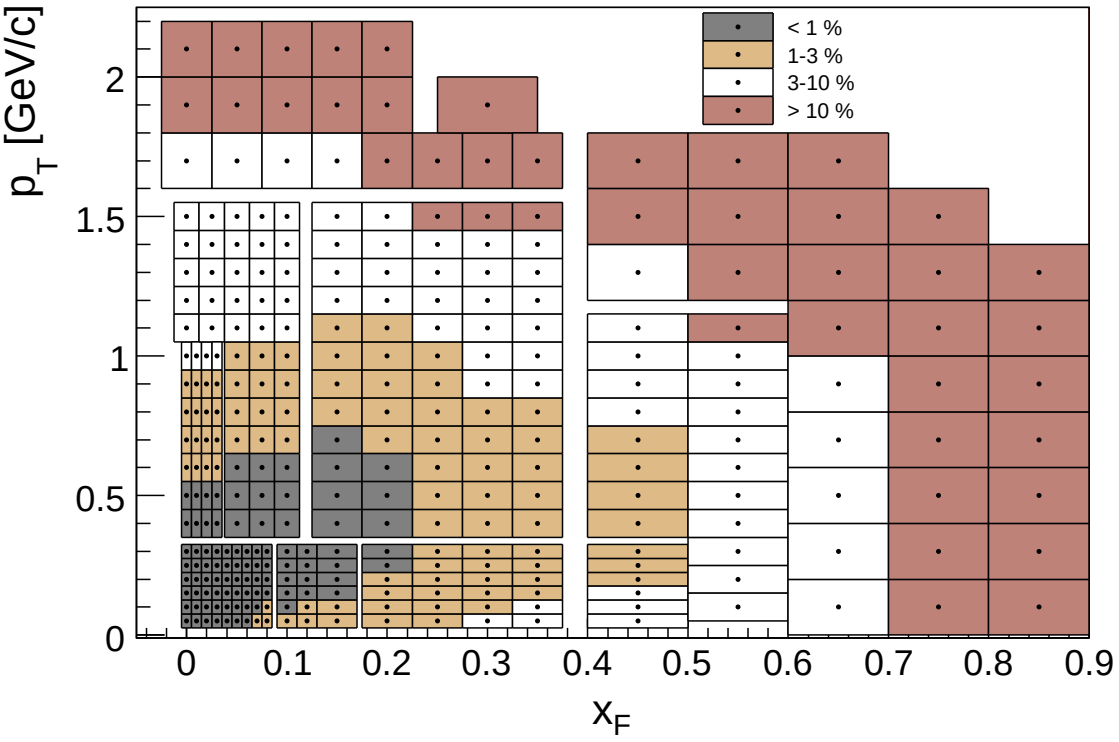

Figure 3.4: Binning scheme in p+p for different x_F and p_T together with the information about bin sizes and statistical error

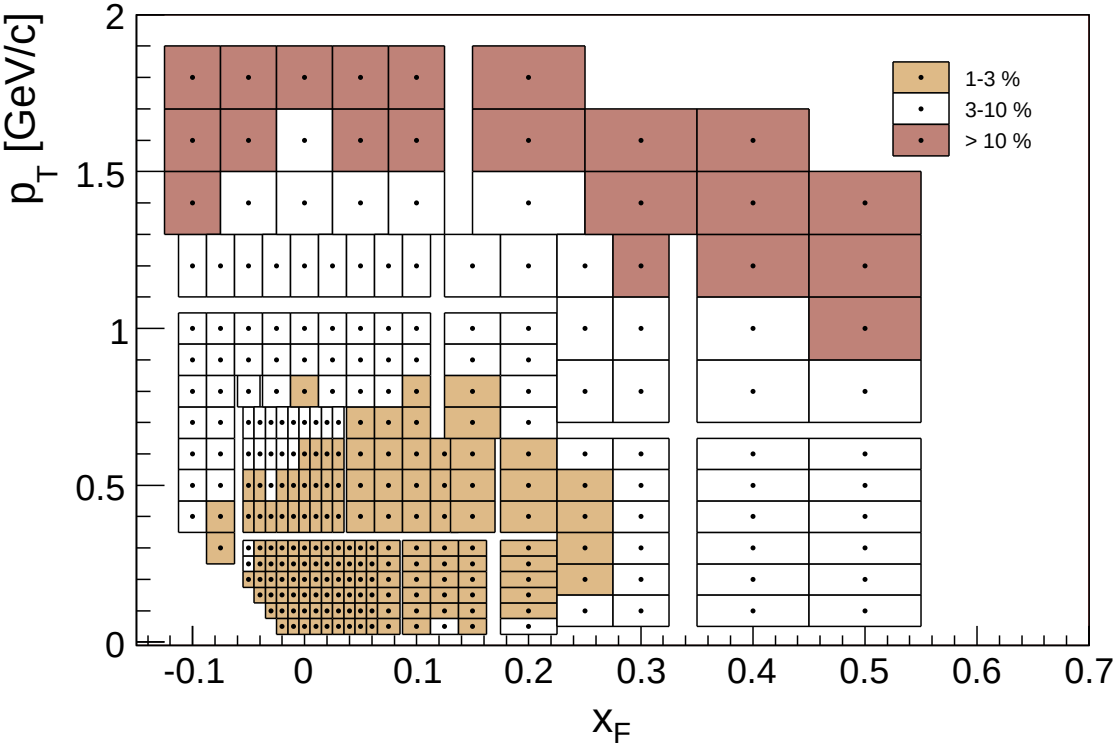

Figure 3.5: Binning scheme in p+C for different x_F and p_T together with the information about bin sizes and statistical error

- Optimization of bin sizes in order to minimize correction for the binning effect, see Sect.4.4.7.

The bin schemes are shown in Fig. 3.4 for p+p and in Fig. 3.5 for p+C.

3.3 Particle Identification

Particle identification on NA49 experiment relies on measurement of the specific energy loss dE/dx in the TPC system.

3.3.1 Bethe-Bloch function

When a charged high energy particle traverses a medium, it losses part of its energy ionizing the atoms, creating free electrons. The energy loss of the particle depends on its velocity which in combination with the measured momentum in a magnetic field allows for identification of the particle. The mean energy loss per unit length is given by the Bethe-Bloch function:

$$\frac{dE}{dx} = \frac{Kz^2}{2}\frac{Z}{A}\frac{1}{\beta^2}\left[\ln\frac{2m_e c^2\beta^2\gamma^2 T_{max}}{I^2} - 2\beta^2 - \delta(\beta)\right] \tag{3.1}$$

Here T_{max} is the maximum kinetic energy which can be obtained by an electron in a single collision, z is the charge of particle traversing medium, Z and A are the atomic number and atomic mass of the medium, I is the mean ionization energy, δ is a density effect

correction to ionization energy loss, K $= 4\pi N_A r_e^2 m_e c^2 = 0.307$ MeV·g^{-1}·cm^2, m_e is the electron mass, r_e is the classical electron radius and N_A is Avogadro number.

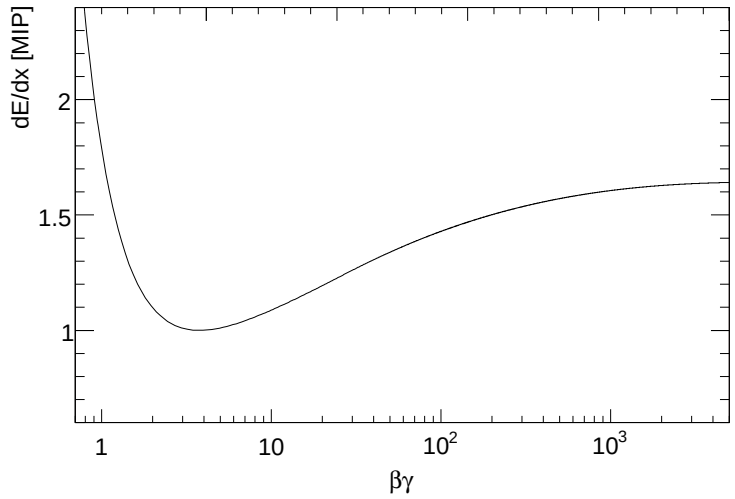

Figure 3.6: Example of Bethe-Bloch function versus $\beta\gamma$

The shape of the Bethe-Bloch function is shown in Fig. 3.6. The main features are the decreasing of the energy losses in the low momentum range as $1/\beta^2$, reaching the minimum at about $\beta\gamma = 3.5 \div 4$ and slow increasing to the saturation value.

3.3.2 dE/dx measurement. Truncated mean. dE/dx resolution

The dE/dx measurement is performed in the TPC system where charge deposits (clusters) along the track in each space point are collected. The track lengths in the gas volume of TPCs reach up to 6 m with a maximum of 234 clusters.

The energy loss by a particle is a random process described by Landau distribution [11] and hence the charge deposits will obey the same distribution. Landau distribution is a wide asymmetric distribution with a long tail to higher values. Therefore the straight forward mean of the charge deposits will not describe good enough the mean energy losses. To improve the dE/dx resolution a truncated mean method is used where 50% of the smallest cluster charges of the track are kept to form the mean energy loss dE/dx. The truncation transform the Landau distribution of the samples into a Gaussian distribution of the mean per track. This truncation produces non-linear transformation of the Bethe-Bloch function which is taken into account by the used distorted approximation of the Bethe-Bloch function, for more details see [12].

If the number of points is above 30 (see Sect.3.1.2) the relative resolution of the specific energy loss is parametrized in the form:

$$\frac{\sigma(N, dE/dx)}{dE/dx} = \sigma_0 \frac{1}{N^b} (dE/dx)^a, \tag{3.2}$$

where dE/dx is the truncated mean, N is the number of points. The parameters σ_0, a, b and dependence of the truncated mean on the number of points $dE/dx(N)$ are determined from the data. To this end, for each of the 62 readout sectors of the TPC system, tracks are binned in laboratory momentum p_{lab} and a preliminary truncated mean distribution is formed with the samples found outside the sector under study. Sharp cuts are performed

on this preliminary dE/dx measurement in order to separate electrons, pions, kaons and protons in each momentum bin. Samples from different, identified tracks in the given sector are then combined into truncated means with an arbitrary number of samples in order to determine the dependences defined above.

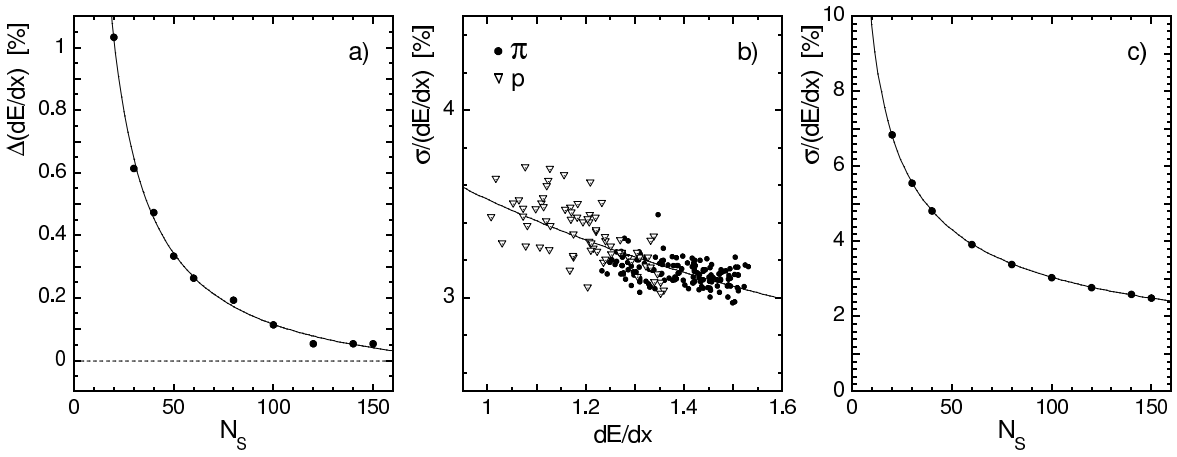

Figure 3.7: a) Deviation of the mean $dE/dx(N_s)$ from $dE/dx(\infty)$ as a function of number of points N_s, b) dE/dx resolution as function of dE/dx, c) dE/dx resolution as function of number of points N_s

The dependence of the dE/dx measurement on the number of samples $dE/dx(N)$ is shown in 3.7a. Parameters a and b are extracted from 3.7b,c:

$$\begin{aligned} a &= -0.39 \pm 0.03, \\ b &= -0.50 \pm 0.01. \end{aligned} \tag{3.3}$$

The function $dE/dx(N)$ and parameters a and b are found independent on the gas type(Ne based in VTPCs and Ar based in MTPCs). The parameter σ_0 also does not depend on the gas type as it has been shown by Lehraus et al. [15] and can be understood by the different behavior of the secondary ionization in various noble gases [16]. The difference in σ_0 comes from the shorter pads in VTPCs (2.8 cm) compared with MTPCs (4 cm). The dependence is given again from parameter a and the results are:

$$\begin{aligned} \sigma_0^{vertex} &= 0.41, \\ \sigma_0^{main} &= 0.352. \end{aligned} \tag{3.4}$$

The truncation introduces a non linearity with relation to Bethe-Bloch function which has a different dependence on particle velocity in the two gases. The difference can reach up to 5% and this has to be taken into account.

If the track has clusters in both chambers (VTPC+MTPC), a truncation is made separately for the clusters in VTPC and for the clusters in MTPC. The truncation value from the MTPC is transformed to the value corresponding to the VTPC using a linear transformation, see [12]. The weighted average is formed taking into account the respective resolutions.

Before forming the truncated mean several corrections to the cluster charge have to be applied to compensate detector effects:

- *Time dependence.* The gas gain of the TPC depends on the variations of the temperature and atmospheric pressure. The TPC gas is under atmospheric pressure and therefore variation in atmospheric pressure are monitored and the gas gain is corrected off-line for this effect. The temperature can be stabilized to a level of $\pm$ 0.1°C by air conditioners. Nevertheless there are still variations in gas gain due to day/night change of temperature, not fully corrected pressure dependence and possible changes in the power. To eliminate these dependences a correction which follows the gas gain during the years of data taking was applied.

- *Track angles.* The pads of the cathode readout plate are tilted with respect to z coordinate up to 55° in order to follow the expected track direction. Despite of this tracks cross the pads with some angle and left less charge on them as they would if they cross the pad in whole its length. A simple geometrical correction for this effect was applied.

- *Drift length.* The drift distance of electrons can reach 110 cm, see Table 2.2. During the drift electrons can be lost due to attachments to O_2 molecules. These losses can reach 1-2% in VTPCs and 3-4% in MTPCs. Other more important loss component arises from the zero suppression threshold at 5 ADC counts. For a bigger drift distance the cluster sizes become larger due to the diffusion and the charge spreads over more pads in the pad raw. In this case the signal in some of the pads could be below the electronic threshold and its contribution to the total charge of the cluster will be lost. A Monte Carlo simulation was developed to correct for these effects which could reach up to 20%.

- *Magnetic effect.* Magnetic field inhomogeneities in the VTPCs lead to appearance of additional force proportional to $E \times B$ which could displaced the charge position up to several cm at the edges of the chamber. A laser system was used to calculate $E \times B$ correction.

The above corrections are applied separately for each readout sector. In total TPC system has 62 sectors, excluding GTPC which is not used for dE/dx measurement. All

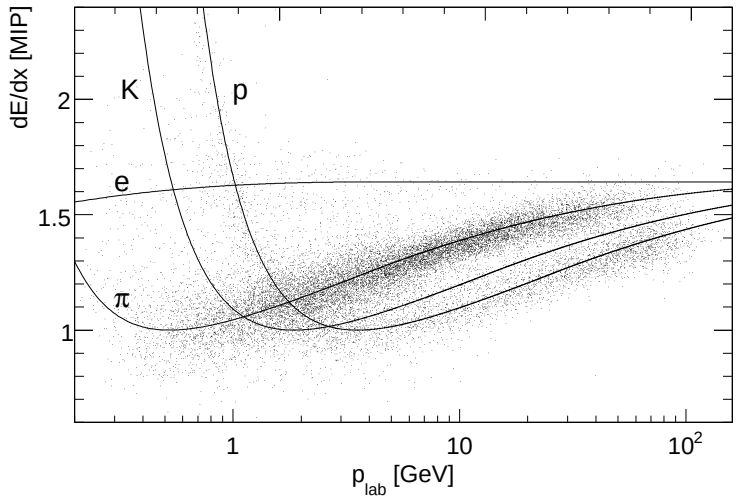

Figure 3.8: Specific energy loss dE/dx with respect to minimum ionization as a function of lab momentum p_{lab}. The lines represent the mean energy loss for different particle types

of the sectors are independent units with separate power supplies which means that gas gain will be different in various sectors. The measured clusters are used to compare gas gain in different sectors, defining a constant (called sector constant) for each sector which characterizes the gas gain in the given sector. An iterative algorithm is developed to equalize the gain in the sectors and normalize cluster charge to parametrized Bethe-Bloch function.

The resulting resolution is typically 3-4% over the most of the phase space and increases to 8% at low x_F and p_T and high x_F due to the smaller number of clusters. A scatter plot of measured dE/dx values, with respect to minimum ionization, versus track momentum is shown in Fig. 3.8. The lines represent the mean response of the detector for the different particle types.

3.3.3 Fit procedure

Particle yields are obtained fitting dE/dx distribution in small momentum bins defined in Sect.3.2. A typical dE/dx distribution is shown in Fig. 3.9.

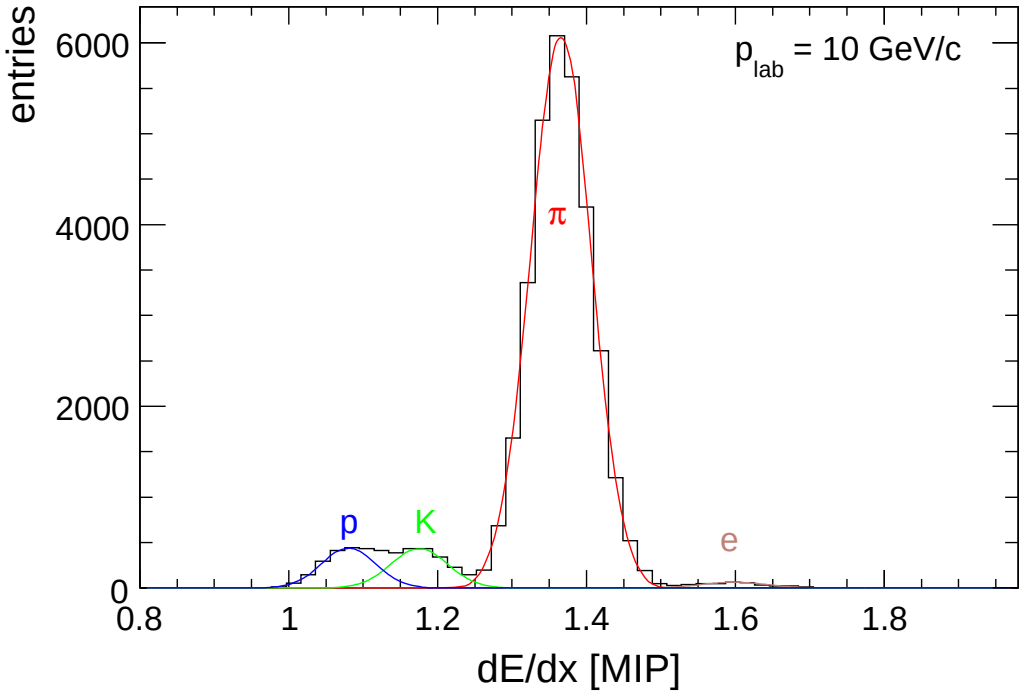

Figure 3.9: A typical dE/dx distribution. The lines represent the fit

The fitting function is based on superposition of Gaussians with form for each track:

$$G(x, x_k^0, \sigma, s_k, r) = \frac{1}{\sqrt{2\pi}(r\sigma)} \exp[-(x - (x_k^0 + s_k))^2/2(r\sigma)^2], \tag{3.5}$$

where with k=1,...,4 is denoted particle type (electrons, pions, kaons, protons), with x the energy loss dE/dx, x_k^0 is the mean energy loss for the particle type i calculated by the parametrized Bethe-Bloch function. The variance σ is derived by using formula 3.2 taking in this way into account proper dE/dx resolution dependence on the number of points N. The parameters s_k (called shifts) with k=1,...,4 and r are extracted from the fit. These five parameters would be determined ($s_k = 0$ and $r = 1$) if the mean energy loss

and σ could be predicted exactly by the Bethe-Bloch and Eq. 3.2, respectively. Due to the complexity of the primary and secondary ionization processes this prediction is, however, not possible on the level of precision needed here. The mean energy loss and resolution are obtained experimentally and some small but significant deviations are present due to imperfections in the dE/dx calibration, like not properly taken out $E \times B$ effect, edge effects, deformations in the parametrization of Bethe-Bloch function. Indeed, in order to keep the systematic error of the extracted yield well below the statistical uncertainty, these shifts have to be and can be determined on the sub-percent level.

The total number of parameters of the fit is nine. The four particle yields in addition to the five parameters mentioned above complete the set. The fitting is performed by minimizing the χ^2 over the dE/dx distribution:

$$\chi^2 = \sum_i^n \frac{(N_i - \sum_{k=1}^4 a_k M_{ik})^2}{\sigma_i^2}, \tag{3.6}$$

where i=1,. . .,n are bins in dE/dx distribution histogram, N_i is measured number of entries in i-th bin, M_{ik} is number of entries defined by Eq.3.5, a_k is the number of the particle of type k divided to the total number of particle in the analysis bin. The parameters a_k are proportional to the particle yields.

3.3.4 dE/dx crossing and backward region

Particle identification based on specific energy loss measurement is not possible in the laboratory momentum range between 1 and 3 GeV/c, due to the cross-over of the energy loss function of the different particle species (π, K, p), see Fig. 3.8. This covers the central region around $x_F = 0$ and low p_T, where the richest pion production is concentrated, as well as a part of the backward hemisphere which can give information for the target fragmentation, especially interesting in asymmetric p+C collisions.

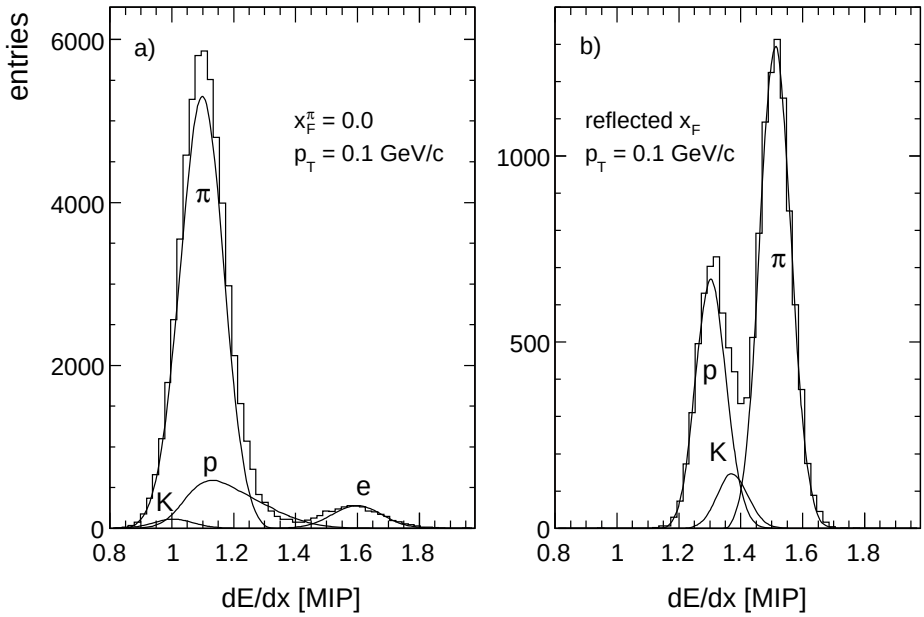

Figure 3.10: dE/dx distribution in a) pion bin (p = 1.6 GeV/c) and b) corresponding reflected proton bin (p = 44 GeV/c)

In order to extract pion yields in this region a reflection technique already used in bubble chamber experiments [45,46] has been adopted. The idea is to measure the number of protons, kaons and electrons and then to subtract them from the total number of particles in the given bin. This is done by transforming the complete pion analysis bin into the lab system, followed by transformation back into the central mass system with proton (or kaon) assumption and reflection of the bin with respect to x_F =0. In the resulting bin the dE/dx fit is performed. The dE/dx distributions for the original pion bin and the corresponding proton-reflected bin is shown in Fig. 3.10.

In the p+p case the reflection technique is used for $p_T < 0.3$ GeV/c at $x_F = 0$ and up to $x_F = 0.02$ at $p_T = 0.05$ GeV/c. In all cases the electrons can be extracted directly from the initial bin as they are separated from the pions. The estimated systematic error from this method is below 1% since the proton and kaon contributions are on the 5-10% level in this kinematic area. The consistency of the method has been tested in bins where both the normal extraction and the reflection method are usable, and its reliability was confirmed.

The extended coverage of the backward hemisphere together with the forward-backward asymmetry of p+C interactions necessitates an extension of the methods developed in [1] for the treatment of the lab momentum region below 3 GeV/c where the energy loss functions of pions, kaons and protons approach each other. The kinematic situation in this region is indicated in Fig. 3.11.

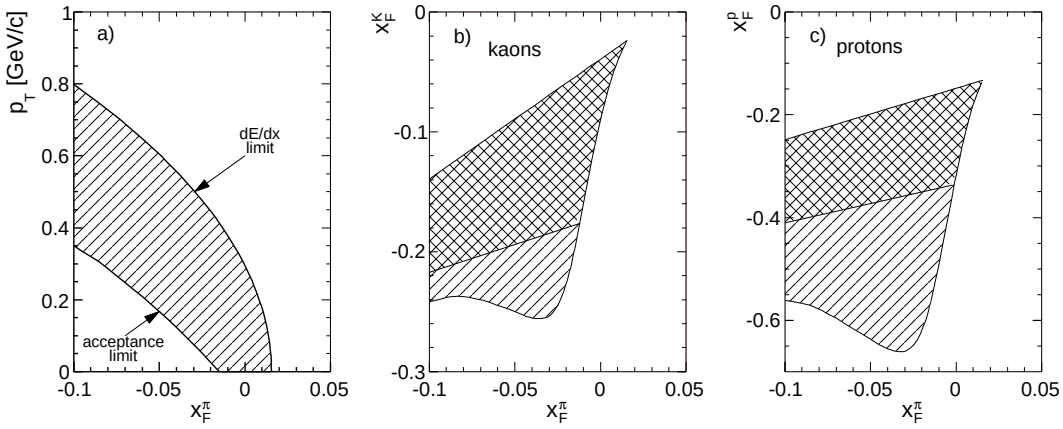

Figure 3.11: dE/dx cross-over region: a) in (x_F,p_T) plane of the pions, b) in (x_F^π,x_F^K) plane, and c) in (x_F^π,x_F^p) plane. The single hatched areas in b) and c) correspond to the regions where pions can be identified due to the $1/\beta^2$ increase of energy loss of the kaons and protons, respectively

Using the pion mass in the transformation from x_F to lab momentum the critical zone is defined by the hatched area in Fig. 3.11a where the upper limit corresponds to $p_{\rm lab}$ = 3 GeV/c and the lower limit traces the p_T cut-off used in the data extraction (Fig. 3.5). This area is mapped into the x_F regions for kaons (Fig. 3.11b) and protons (Fig. 3.11c) as a function of $x_F^{\rm pion}$ when using the proper masses in the corresponding Lorentz transformations.

For protons this ratio is measured in some areas as shown in Fig. 3.12. Three regions are observed – $x_F < 0.2$, $x_F = 0.2 \div 0.4$ and $x_F = 0.4 \div 0.6$. In the low x_F region the specific ionization losses dE/dx of the protons are smaller than pion losses, in the high x_F region is opposite – proton losses are bigger than pion losses. The reflection method is applied in the middle using the interpolation curve.

The $\overline{\rm p}/\pi^-$ and K/π ratios are smaller than 10% for all bins in the critical area. Here

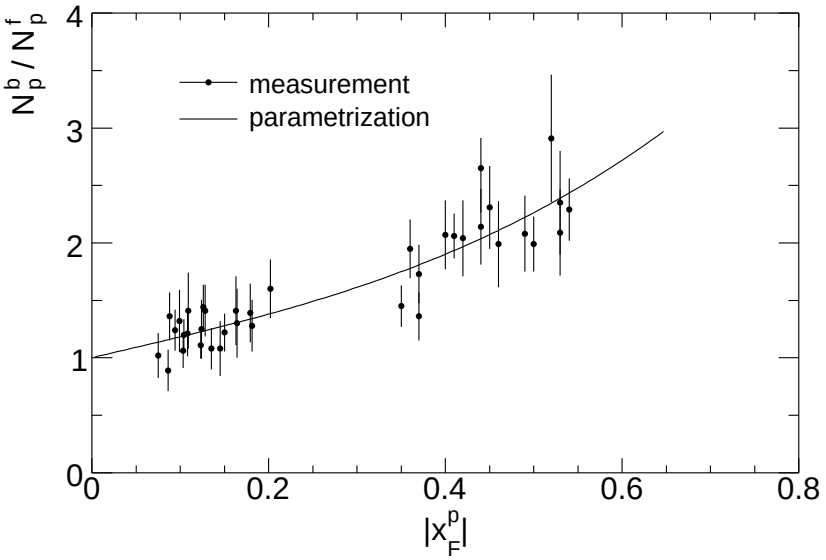

Figure 3.12: Backward-forward ratio for the protons as a function x_F in p+C reaction. No p_T dependence is seen. With the line is presented the parametrization of the data which is used for correction

again the method of bin reflection was used by imposing an extrapolation of the measured yield ratio with respect to p+p interactions into the backward hemisphere as shown in Fig. 3.13 for kaons. In this case the ratio in the far backward region corresponds to the mean number of projectile collisions predicted from the inelastic p+C and p+p cross sections, see Sect. 7.2.2. For kaons the different loss rates from weak decays in the forward and backward hemispheres were taken into account in the yield determination.

The statistical errors given for the data points in the dE/dx overlap region are defined as $\sqrt{\text{number of tracks}}/(\text{number of pions})$ in each bin, thus taking into account possible systematic uncertainties in the yield extraction. These uncertainties are related to the

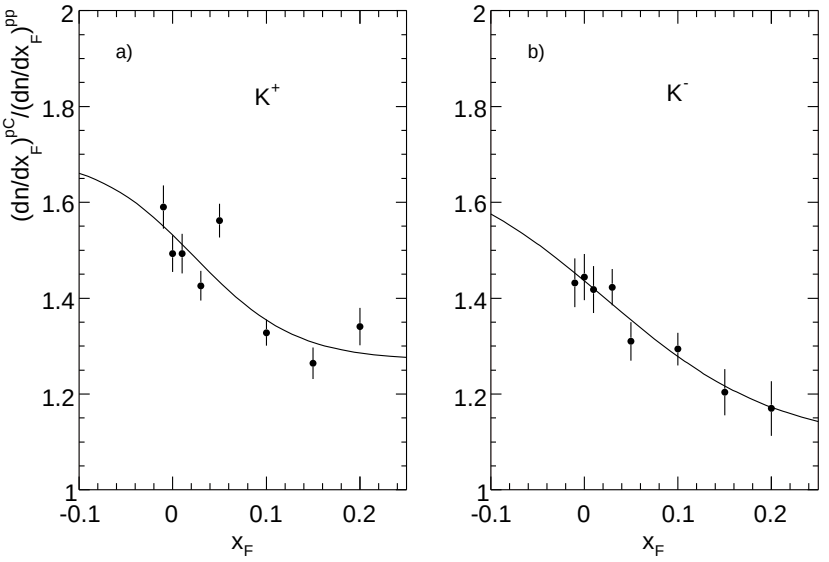

Figure 3.13: $(dn/dx_F)^{\mathrm{pC}}/(dn/dx_F)^{\mathrm{pp}}$ ratio as a function of x_F of the kaons for a) K^+ and b) K^-

K/π and p/π ratios. For negative pions, the K^-/π^- and $\overline{p}/\pi^-$ ratios reach the maximum values of 10% and 2% respectively as given above, at the upper end of the p_T scale in the hatched region in Fig. 3.11a. Here, the extrapolation from the measured region does not allow for noticeable systematic deviations. These ratios decrease rapidly with decreasing of p_T to a few percent for K/π and to zero for $\overline{p}/\pi^-$. This is a consequence of the steep x_F dependence of the yields of these particles, and the large difference in x_F for the different masses, Fig 3.11b,c. Even sizable error limits in the extracted forward/backward behaviour of K^- and $\overline{p}$ will therefore result in systematic deviations within the error estimation given above.

The p/π^+ ratio reaches maximum values between 10% and 40% in the upper p_T range of Fig. 3.11a. Here again the extrapolation from the measured region, the interpolation using the reflection method, Fig. 3.12, the rapid decrease of the ratio as function of p_T and the clean separation of the proton yields in the low momentum region keep the systematic uncertainties below the statistical errors.

3.3.5 Constraints on electrons and kaons at high x_F

At x_F above 0.3 ($p_{lab} \approx 45$ GeV/c) the energy loss of all particle types approach the relativistic plateau which makes independent particle extraction difficult. In addition to this the yields decrease rapidly as x_F increases which progressively reduces the available statistics per bin. Furthermore, the track lengths become shorter which makes dE/dx measurement less precise.

In this region the e/π ratio is typically of order of a few permille. The electron peak lies in the tail of the pion peak and the fit has a tendency to overestimate the electron yield obtaining ratio on the level of few percent. In order to control e/π ratio, a Monte Carlo simulation was constructed assuming that electrons come mostly from π^0 decays. The π^0 cross section is derived by averaging the measured charged pions. The conversion probability is adjusted to the measurement of e/π ratio at $x_F = 0.05$ as shown in Fig. 3.14.

The $(K^-+\overline{p})/\pi^-$ ratio falls steeply with x_F for all p_T values. As dE/dx fits become very unreliable above $x_F = 0.55$ measurement was complemented with values from other experiments [20, 21] which allowed to extend data set for π^- in p+p up to $x_F = 0.85$. Such data sets are not available in the p+C case which in addition with lower statistics

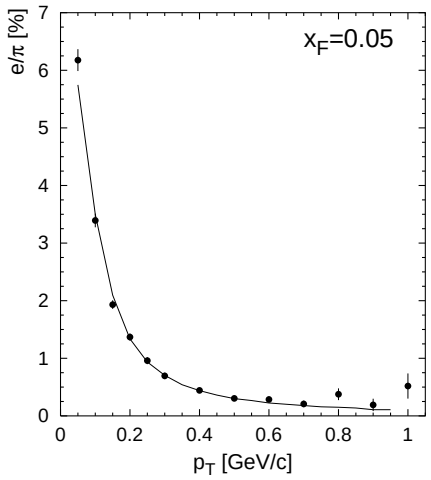

Figure 3.14: The e/π ratio as a function of p_T at $x_F = 0.05$. The line represents the Monte Carlo results

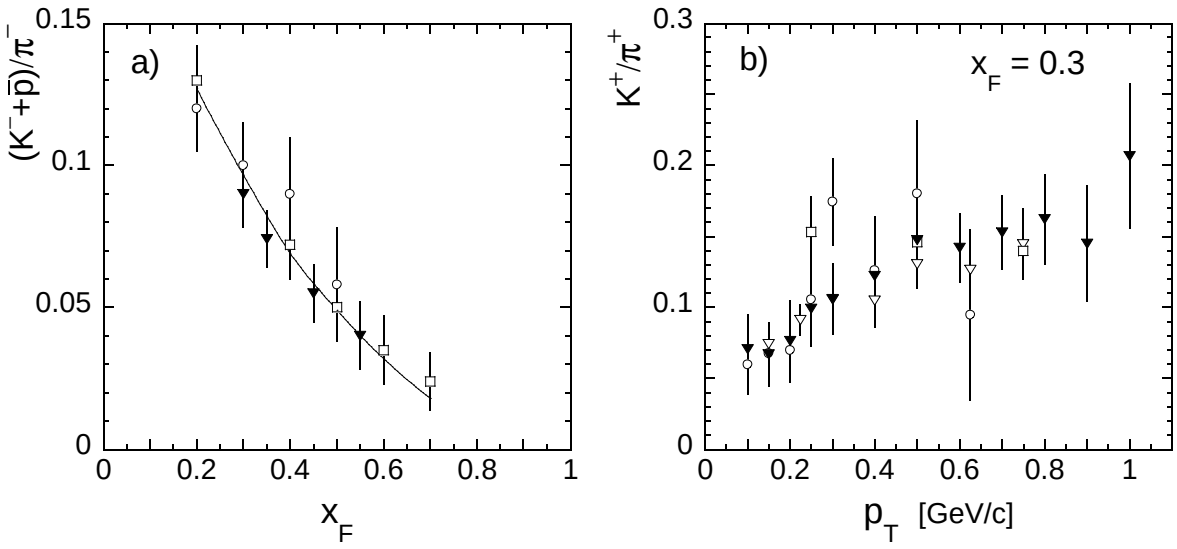

Figure 3.15: a)$(\mathrm{K}^- + \overline{\mathrm{p}})/\pi^-$ ratio as a function of x_F measured by [21](open circles), [20] (open squares) and NA49 (full triangles), b) K^+/π^+ ratio as a function of p_T at $x_F = 0.3$ measured by [21] (open circles and triangles), [20] (open squares) and NA49 (full triangles)

restricts data extraction to $x_F = 0.5$.

In the case of K^+ the situation is even more difficult because of the dominant proton component. The K^+ are situated between two larger peaks of pions and protons and the dE/dx fit tends to find unphysical local minimum of χ^2 displacing kaon position towards pions or protons. In this area K^+ shifts have to be constrained using proton and pion shift values. The resulting ratio K^+/π^+ is in good agreement with other experiments [20, 21].

Chapter 4

Cross section and Corrections

4.1 Total inelastic cross section

In p+p interaction the total cross section $\sigma_{\rm tot}$ is given by the sum:

$$\sigma_{\rm tot} = \sigma_{\rm el} + \sigma_{\rm inel}, \tag{4.1}$$

where $\sigma_{\rm el}$ is the total elastic cross section with no secondary particles produced and $\sigma_{\rm inel}$ is the total inelastic cross section which was measured to be 31.78 mb [37, 38].

In p+C interaction $\sigma_{\rm tot}$ is defined as:

$$\sigma_{\rm tot} = \sigma_{\rm el} + \sigma_{\rm inel} + \sigma_{\rm quasi}. \tag{4.2}$$

Here in contrast to p+p an additional member appears $\sigma_{\rm quasi}$, so called quasi-elastic scattering. This corresponds to scattering of incoming proton on individual nucleons in the carbon nucleus as $\sigma_{\rm el}$ is the scattering of the proton from the whole nucleus. The p+C total inelastic cross section was measured in several experiments [39–43], however in the most of the cases $\sigma_{\rm quasi}$ was not taken into account. After correction for $\sigma_{\rm quasi}$ the mean $\sigma_{\rm inel}$ was found to be 225.8 mb.

4.2 Trigger cross section

The NA49 trigger defines the trigger cross section $\sigma_{\rm trig}$ calculated by the formula:

$$\sigma_{\rm trig} = \frac{P}{\rho \cdot l \cdot N_A/A}, \tag{4.3}$$

where ρ, l, N_A and A are, respectively, the target density, target length, Avogadro number and target atomic number. The specifications of the targets are given in Table 2.1. The interaction probability of the incoming proton with the target is determined by the relation:

$$P = \frac{R_{\rm FT} - R_{\rm ET}}{R_{\rm beam}} \left(1 + \frac{R_{\rm FT} - R_{\rm ET}}{2R_{\rm beam}} + \frac{R_{\rm ET}}{R_{\rm beam}} + \frac{\rho_{\rm ET}}{\rho} \right), \tag{4.4}$$

where $R_{\rm beam}$ is the beam rate defined by the beam condition and $R_{\rm FT}$ and $R_{\rm ET}$ are interaction rates determined by the trigger condition for full and empty target operation, respectively, see Sect. 2.1. The additional members in the brackets appeared to correct for the exponential beam attenuation in the target, the reduction of the beam intensity

due to interactions upstream of the target, the reduction of the downstream interaction probability in the full target operation and the content of the empty target – a gaseous hydrogen in the proton target and air in carbon case. In the expression higher order terms are neglected. The total correction amounts to 2.5% for proton target and 1.3% for carbon target depending on target interaction length, see Table 2.1.

The carbon target has a diameter of 6 mm which makes possible beam particle to bypass the target without hitting S4. The losses were estimated to be 3.3% of the trigger cross section.

From the measured trigger cross section the total inelastic cross section was derived by using Monte Carlo calculation which takes into account the inclusive distributions of protons, kaons and pions in order to determine the loss of events due to produced particles hitting S4 as well as the contribution from the elastic scattering. The resulting cross sections and different components are summarized in Table 4.1.

reaction	p+p	p+C
σ_{trig}	28.23 mb	210.1 mb
loss from p	3.98 mb	17.1 mb
loss from π and K	0.33 mb	2.4 mb
contribution from σ_{el}	-1.08 mb	-3.3 mb
predicted σ_{inel}	31.46 mb	226.3 mb
literature value	31.78 mb	225.8 mb

Table 4.1: Contribution derived by Monte Carlo calculation and determined trigger and inelastic cross section

The systematic errors of these measurements have been estimated to be 1% and 2.5% for p+p and p+C collisions, respectively. The extracted inelastic cross sections are in agreement with literature values to within one percent. The total trigger loss amounts to about 14% in p+p and 9% in p+C. This is explained by the presence of less forward charged particles at high x_F in p+C which can hit S4.

4.3 Double differential cross section

The invariant double differential cross section, given as a function of Feynman variable x_F and transverse momentum p_T, is defined by the formula:

$$f(x_F, p_T) = E(x_F, p_T) \cdot \frac{d^3\sigma}{dp^3}(x_F, p_T), \tag{4.5}$$

where dp^3 is infinitesimal volume element in three dimensional momentum space.

The cross section measurement has to be performed in the finite volume element Δp^3 and $f(x_F, p_T)$ is approximated by the measured quantity:

$$f_{\text{meas}}(x_F, p_T, \Delta p^3) = E(x_F, p_T, \Delta p^3) \cdot \frac{\sigma_{\text{trig}}}{N_{\text{ev}}} \cdot \frac{\Delta n(x_F, p_T, \Delta p^3)}{\Delta p^3}, \tag{4.6}$$

where σ_{trig} is the trigger cross section, N_{ev} the number of events and Δn the number of identified pions in the bin Δp^3. The measured quantities Δn, N_{ev}, σ_{trig}, Δp^3 are biased by several effects:

- The number of pions Δn has to be corrected for secondary interactions of produced particles in the target, weak decay of pions, pion absorption in the detector material, pion produced from weakly decaying strange particles (feed-down).
- The ratio $\Delta n/N_{\text{ev}}$ has to be determined from full and empty target measurement.
- The measured σ_{trig} is not equal to σ_{inel}. This shows that trigger is not 100% effective which is due to non-triggered inelastic events or triggered elastic events.
- As the cross section f has an arbitrary functional shape, the measured quantity f_{meas} depends on bin width Δp^3 via E and Δn. This requires replacing the finite volume element Δp^3 by the infinitesimal dp^3 by introducing binning correction.

These effects lead to seven corrections which are applied to the f_{meas}. The corrections are discussed in more details in Sect. 4.4.

4.4 Corrections

4.4.1 Trigger bias correction

As was already mentioned the trigger is not fully effective for selection of inelastic events. This is due to the fact that secondary produced particles can hit the anti-counter S4. In this way only about 86% of proton-proton and 91% of proton-carbon inelastic events are accepted. The measured cross section will be affected via the expression

$$f_{\text{meas}} \sim \sigma_{\text{trig}} \cdot \frac{\Delta n}{N_{\text{ev}}} \tag{4.7}$$

in a non-trivial way. The correction depends on event topologies. For instance, if there is a very forward particle detected than no other particles can reach S4 by energy-momentum conservation and the correction will be zero. On the other hand, as it has been shown that particle production completely decouples between forward and backward hemispheres [19], the loss in the target region will be entirely felt. A smooth transition from zero at very forward region to maximum correction in backward region can be expected.

Detailed correction table were obtained experimentally by increasing the diameter of the S4 counter off-line and extrapolating the observed change in cross section to surface zero. The method relies entirely on measured quantities because generators are not reliable at the level of precision required. The systematic error in this method is dominated by the statistical error of the evaluation, typically a factor of three smaller than the statistical error of the extracted data.

The resulting trigger bias correction in p+p and p+C collisions as a function of x_F for different values of p_T is presented in Fig. 4.1. Indeed, the general trend is visible increasing from forward to backward region. For small p_T values a significant micro-structure in the x_F dependence appears which is reflection of hadronic two-body correlation driven by resonance decay. The correction is bigger in p+p reaction as there are more very forward particles than in p+C collisions which can hit S4.

4.4.2 Secondary interactions in the target

The produced particles travel through the target material where a secondary interaction can occur. The correction for such secondary interaction in p+p was evaluated using the

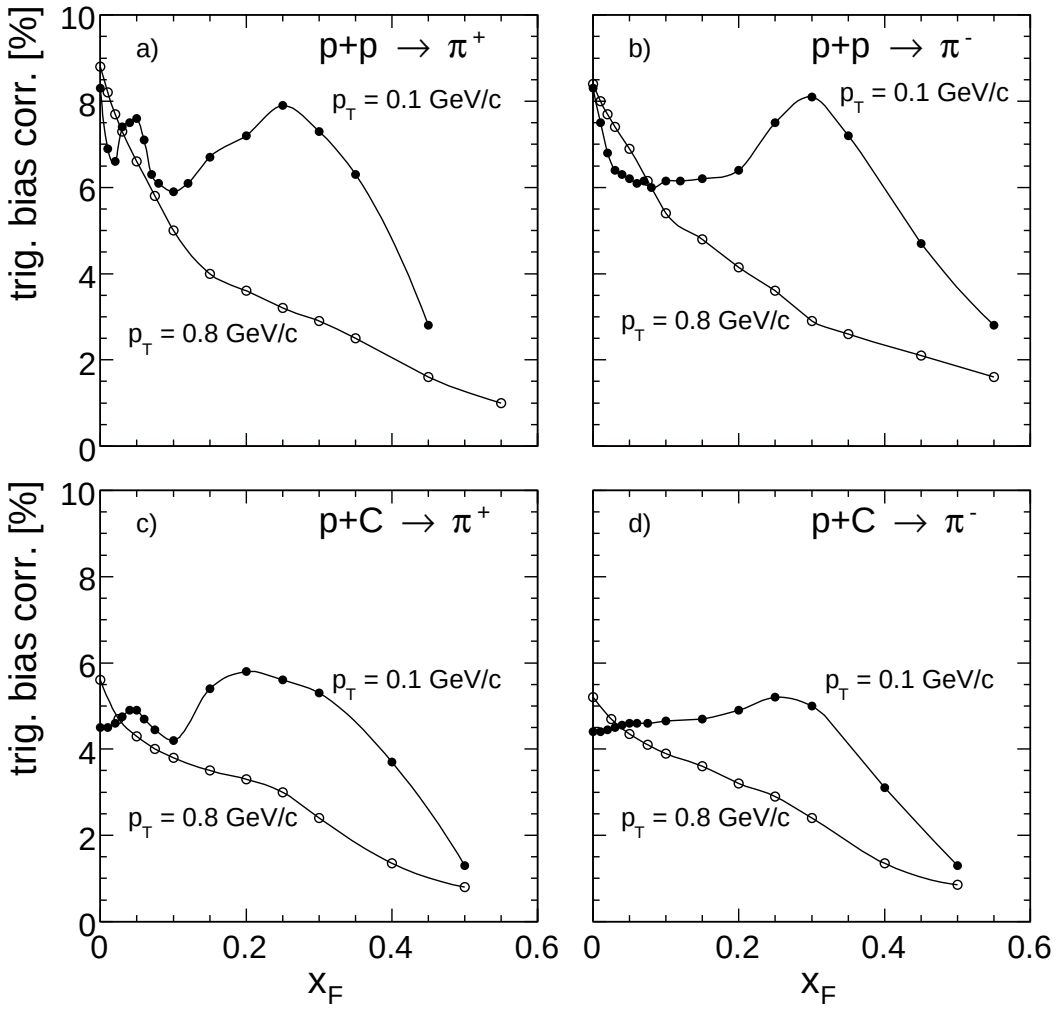

Figure 4.1: Trigger bias correction as a function of x_F at two p_T values: 0.1 GeV/c (full circles) and 0.8 GeV/c (open circles) for a) π^+ and b) π^- in p+p reaction, and c) π^+ and d) π^- in p+C reaction

PYTHIA event generator [44], assuming that all daughter particles from these secondary interactions are reconstructed at the primary vertex. As in this secondary interaction pions do not only vanish but also other pions are produced, the correction factors are bigger than 1 in the high x_F region and smaller than 1 in the low x_F region where pion production dominates. Correction for secondary interactions in the target in p+p collisions is shown in Fig. 4.2. In the case of p+C interaction the correction was estimated, by scaling down p+p correction proportional to the target interaction length, see Table 2.1.

4.4.3 Absorption correction

The absorption of pions in the detector material is studied by using GEANT simulation of the NA49 detector. The correction is determined assuming that all primary pions undergoing hadronic interaction before detection are lost. Even with this assumption which simplifies the analysis and given the small value of the correction itself, an introduced systematic error is small. The detector absorption correction as a function of x_F for two p_T values is shown in Fig. 4.3. At low p_T the x_F dependence exhibits a multiple maxima

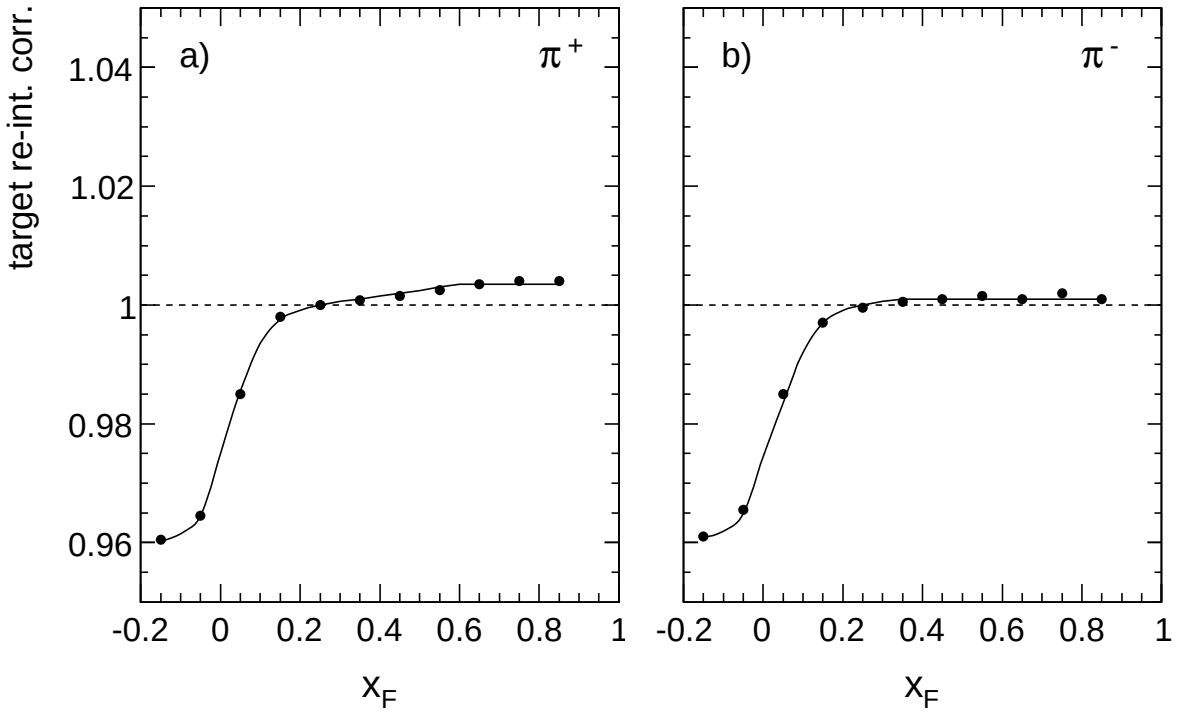

Figure 4.2: Correction factor accounting for the secondary interactions in the target of the produced particles in p+p reaction

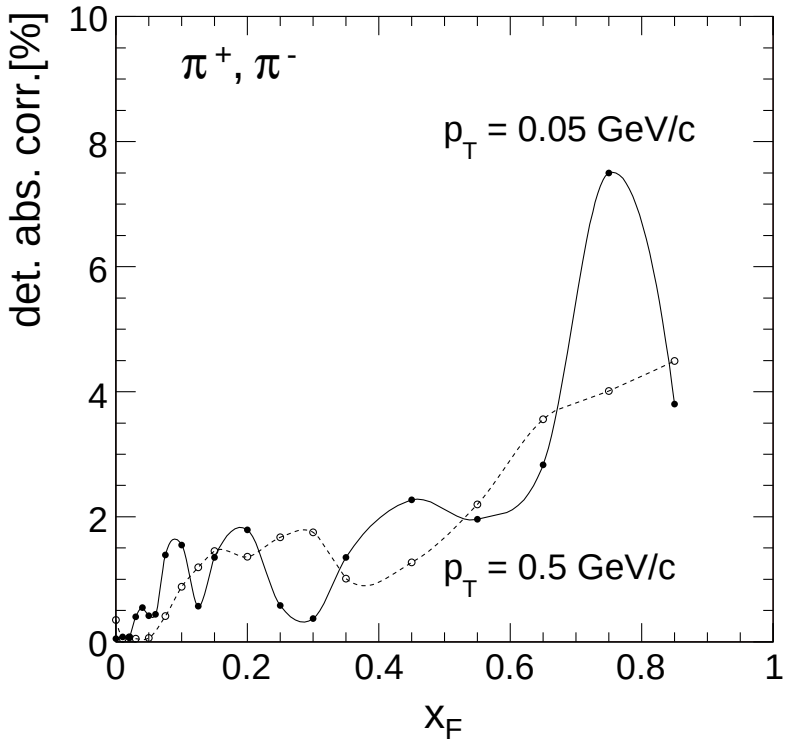

Figure 4.3: Detector absorption correction for pions as a function of x_F

which corresponds to the positions of the ceramic supported tubes of the TPC field cages, see Sect.2.4.4. The correction is equal for positive and negative pions as well as for the p+p and p+C interactions.

4.4.4 Empty target correction

The particle yields ($\sim \Delta n/N_{\rm ev}$) can be measured by determining yields for full and empty target conditions using formula:

$$\left(\frac{\Delta n}{N_{\rm ev}}\right)^{\rm FT\text{-}ET} = \frac{1}{1-\epsilon}\left(\left(\frac{\Delta n}{N_{\rm ev}}\right)^{\rm FT} - \epsilon\left(\frac{\Delta n}{N_{\rm ev}}\right)^{\rm ET}\right), \tag{4.8}$$

where $\epsilon = R_{\rm ET}/R_{\rm FT}$.

Such a method of yield (cross section) evaluation would require a large enough sample of empty target events to comply with statistical precision of the full target data. In addition to this, as empty target rate $R_{\rm ET}$ is much smaller than full target rate $R_{\rm FT}$, there would be identification problems in the regions of low particle production where fits of the energy loss distribution becomes critical anyway. Taking into account these constraints and the relatively small data samples taken with empty target conditions, a more efficient way of normalization was used. With suitable off-line event cuts, described in Sect.3.1.1, the empty/full target event ratio was decreased to 9% in p+p and 16% in p+C. In fact the contribution from empty target events to the track numbers is about twice smaller due to the larger content of empty events ("zero prong"). These makes possible to extract cross section of the full target sample alone and treat the empty target contribution as a small correction. The detailed studies have shown that this correction is the same for π^+ and π^- and there is no measurable p_T dependence in both interactions. The x_F dependence of the correction, defined as the ratio of the derived yields with proper

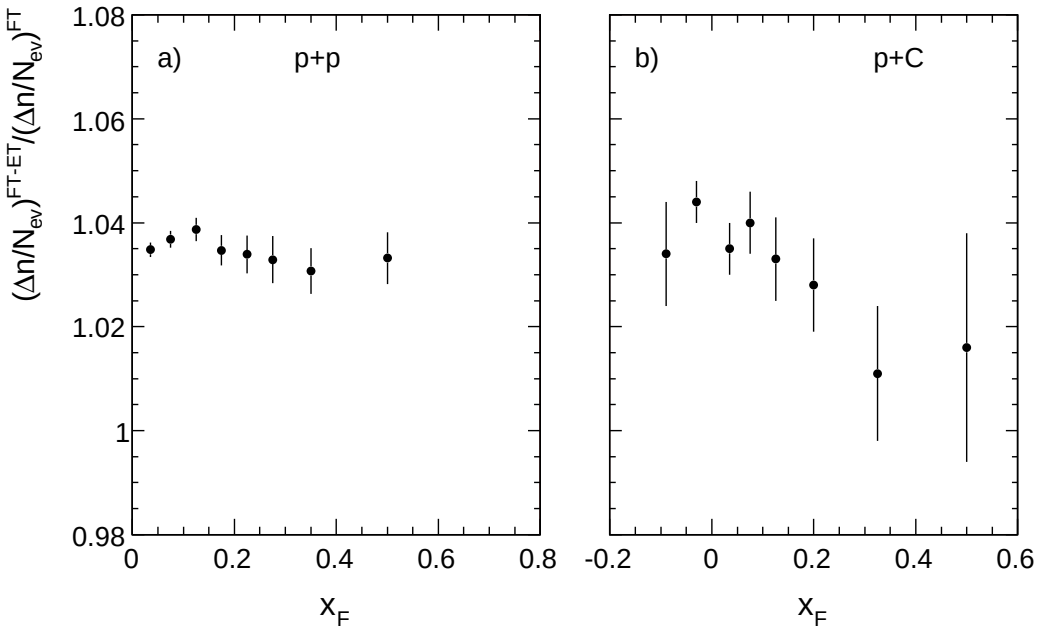

Figure 4.4: Correction factor accounting for empty target contribution as a function of x_F and p_T integrated for average π^+ and π^-

full-empty target subtraction, using Eq. 4.8, and the one measured from full target data only is presented in Fig. 4.4. The correction size in the case of p+p interactions is at the level of 4% and varies less than 1% with x_F while in the p+C case it decreases from 4% to 1% in the forward region.

4.4.5 Pion weak decays

The pions can decay via the weak channel $\pi \rightarrow \mu + \nu_\mu$. Due to the sizable decay length only a small fraction of the pions will decay on their way through the detector, reaching a maximum of 4.2% at the lowest accepted $p_{lab} = 0.5$ GeV/c. Fortunately, most of these decays will not cause track loss or particle misidentification, as the dip angle of the muon track, which is most critical for its reconstruction at the primary vertex, deviates less than 1% from the pion direction at the lowest energy, and the muon taken on average about 80% of the pion momentum. The muons from decay produced before the VTPC1 in the field-free region will be reconstructed at the vertex. The same applies to decays downstream of the VTPC2. The only contribution to the correction will come from decays inside the magnetic field before the primary track has left the 30 points for the dE/dx analysis and the secondary track escapes reconstruction. The tracking inefficiency for this sample, which amounts to 1.5% at $x_F = 0$ and $p_T = 0$, is determined to be 20%±10%, by regarding fraction of tracks with less than 30 points in this momentum range. An extensive eye-scans confirmed that most of this short tracks are caused by secondary hadronic interactions and kaon decay but not pion decay. The resulting correction is shown in Fig. 4.5 which decrease rapidly with increasing laboratory momentum.

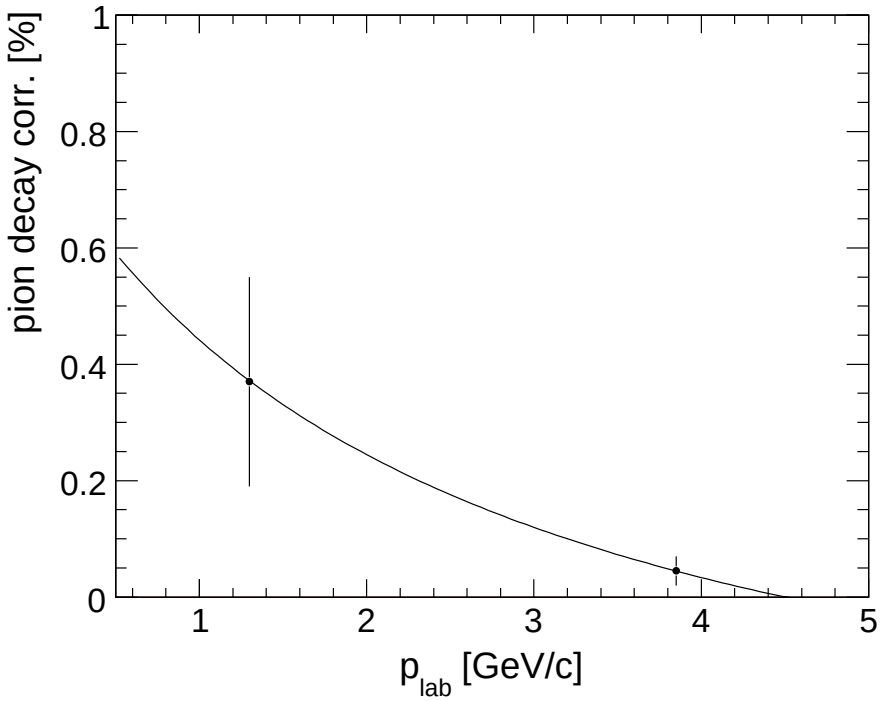

Figure 4.5: Pion decay correction

Concerning particle identification the muon energy losses would be shifted upward with about one standard deviation from the pion position. This small shift will be absorbed in the following fit of the pion peak position and width in each bin.

4.4.6 Feed-down correction

Feed-down is the fraction of particles which are produced via weak decays of the strange particles. Sources for the pion feed-down are: K^0_s, $\overline{\Lambda}$ and Σ^+ for π^+ and K^0_s, Λ and Σ^- for π^-.

In principle it may be a matter of discussion whether the feed-down pions should be subtracted or not into the yield. None of the previous experiments has attempted a feed-down correction, neither bubble chamber experiments nor counter experiments. In fact, in the bubble chambers most of the decay product would not be detected due to small detector size and too long decay lengths. In the counter experiments the situation is less clear as the detectors are long enough to see a sizable fraction of decay products. Nevertheless, as the feed-down is concentrated at low x_F and low p_T, these experiments are save by the fact that they typically don't have acceptance in these regions.

As NA49 fully covers low x_F and low p_T regions, a complete feed-down correction has been performed regarding all possible sources mentioned above.

The correction determination proceeds in three steps. First, the double differential distributions of parents has been obtained using the existing data. Second, using a Monte Carlo calculation the parent particles are consecutively generated, according their distributions, and decayed obtaining in this way the yields of the daughter particles in the x_F/p_T bin of the experiment. Third, the produced distributions are folded with reconstruction efficiency which is derived from a full GEANT simulation of the NA49 detector using a complete generated events containing the strange hadrons.

The distributions of the parent particles as a function of x_F and integrated over p_T are presented in Fig. 4.6. The corresponding p_T distribution are extracted for K^0_s from

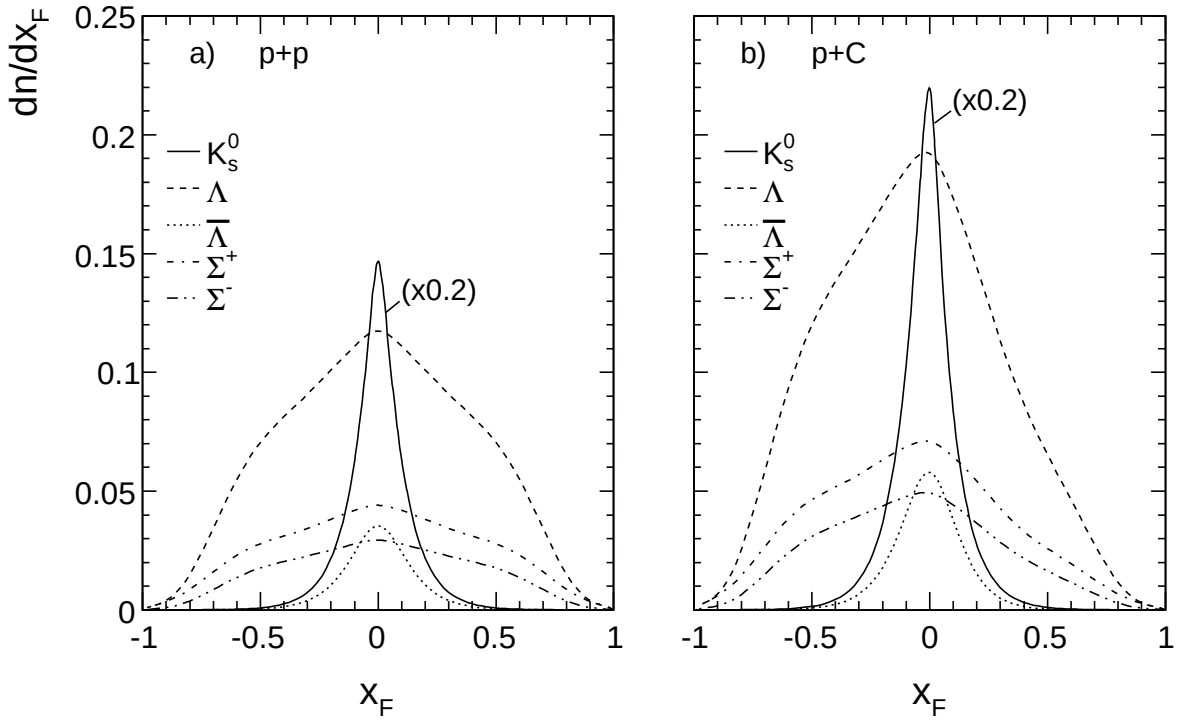

Figure 4.6: The p_T integrated x_F distributions dn/dx_F of parent particles contributing to pion feed-down in: a) p+p interaction and b) p+C interaction. The K^0_s distribution is shrunk 5 times in order to conform with other distributions

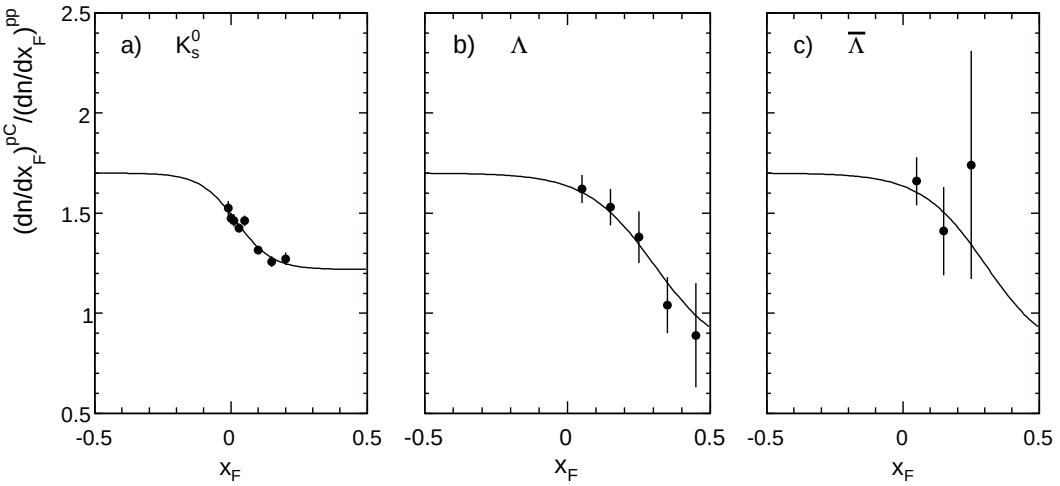

Figure 4.7: The yield ratio of p+C to p+p as function of x_F for a)K^0_s, b)Λ, c)$\overline{\Lambda}$. The dots denote the measurement and lines the parametrization

averaged charged kaon data and for Λ from combined set of bubble chambers, NA49 and ISR [46–49].

The average reconstruction efficiency reaches level of up to 50% in the low x_F regions where the feed-down correction is substantial. It is rather independent of p_T but shows a strong variation with the azimuthal angle which leads to to the restriction of the ϕ window in the bins even the vertex tracks have full acceptance.

The knowledge of the parent distribution is very limited thus this is the main source of the systematic uncertainty. In the case of p+C interactions there is no available measurements. The corresponding yields have therefore been determined from the NA49 data directly using the following yield ratios with respect to p+p interactions:

- The K^0_S yield is extracted from $(K^+ + K^-)/2$ as a function of x_F and p_T. The measured ratio is extrapolated into the backward hemisphere using a two-component superposition picture [17] as shown in Fig. 4.7a for the p_T integrated ratio. As the kaon yields do not suffer from isospin effects [17] this extrapolation is straightforward concerning the target contribution which corresponds to the average number of 1.7 target nucleons hit by the projectile.

- The evolution of Λ and $\bar{\Lambda}$ yields relative to p+p is obtained from p+π^- and $\overline{\mathrm{p}}$+π^+ mass distributions exploiting the event mixing technique described in [83] and using vertex tracks both for the baryon and for the meson involved. The resulting p_T integrated yield ratios are shown in Figs. 4.7b,c. For the extrapolation into the backward hemisphere the two-component superposition picture is again used. No isospin effects are present in this extrapolation.

The yield ratios for $\Sigma^{\pm}$ are derived from the Λ parametrization using the Σ/Λ ratios from p+p in the projectile hemisphere. In the target fragmentation region the expected isospin effects are taken into account. The on-vertex reconstruction efficiency for the daughter pions is obtained by using two-dimensional acceptance tables established from a full GEANT simulation of the NA49 detector.

The resulting feed-down correction as a function of x_F for several p_T values is shown in Fig. 4.8. In the two top panels the feed-down correction in p+p is presented and in the two

bottom panels the feed-down correction in p+C is shown. The correction exhibits very complex structure in x_F and p_T reaching sizable values in the low p_T and extends rather up in x_F. In both reactions the feed-down for π^- is larger than for π^+ corresponding to dominant Λ component over the $\overline{\Lambda}$ (see Fig. 4.6) concentrated in the low p_T and low x_F region. The correction is very similar for p+p and p+C reaction. In the backward region in p+C interaction it keeps growing up and reaches maximum in small negative x_F values. The size of the correction shows that one has to take great care in comparing experiments with undefined feed-down treatment in these areas.

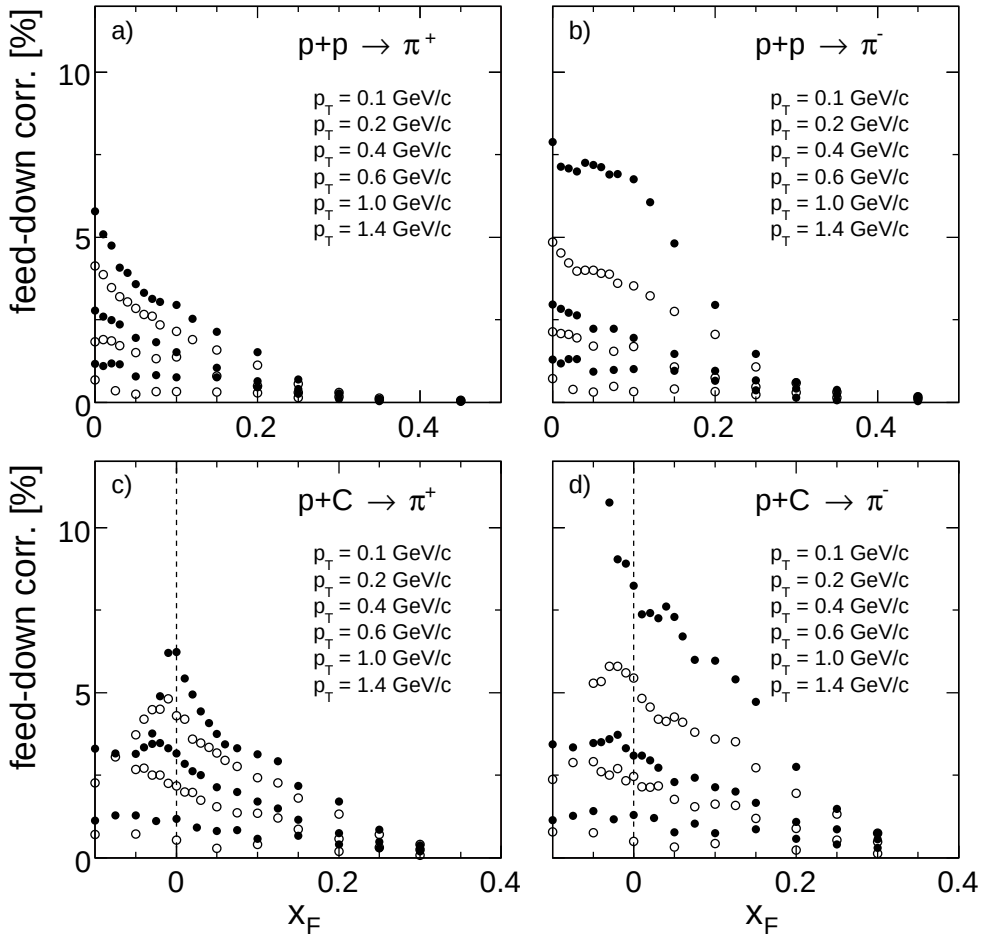

Figure 4.8: Feed-down correction as a function of x_F for different p_T values for a)π^+ in p+p, b)π^- in p+p, c)π^+ in p+C and d)π^- in p+C

4.4.7 Binning correction

The invariant cross section from Eq. 4.5 is defined for the infinitesimal volume dp^3. By necessity the measurement has to be performed in the finite volume element Δp^3. Therefore the extracted yield is integral of the particle density over the phase space element Δp^3. Following from the cylindrical symmetry of the interactions the density function is flat against the azimuthal angle ϕ and no binning effects are present. Thus the problem reduces to a determination of the binning correction as a function of x_F and p_T.

Let's measure density function $\rho(t)$ over the variable t. If we denote the bin width with Δ and the bin center with t_0 than the measured value is:

$$\rho_{\text{meas}}(t_0) = \frac{1}{\Delta}\int_{t_0-\Delta/2}^{t_0+\Delta/2} \rho(t)dt \tag{4.9}$$

After making the Taylor expansion of the function $\rho(t)$ at point t_0 up to the second order terms

$$\rho(t) \approx \rho(t_0) + \rho'(t_0)(t-t_0) + \rho''(t_0)\frac{(t-t_0)^2}{2} \tag{4.10}$$

and substituting it in the Eq. 4.9 we obtain for the $\rho_{meas}(t_0)$ the following approximation:

$$\rho_{\text{meas}}(t_0) \approx \rho(t_0) + \frac{1}{24}\rho''(t_0)\Delta^2. \tag{4.11}$$

Here $\rho(t_0)$ is the real density value at t_0. Hence the binning correction can be defined as the difference between the real density value and the measured one which is proportional to the second derivative and the square of the bin width. This approximation holds if the difference does not exceed a few percent.

In this approximation the second derivative can be determined from the neighbouring data points:

$$\rho''(t_0) \approx \left(\left(\frac{\Delta_1\rho(t_2) + \Delta_2\rho(t_1)}{\Delta_1 + \Delta_2}\right) - \rho(t_0)\right)\frac{2}{\Delta_1\Delta_2}. \tag{4.12}$$

The definition of the variables is sketched in Fig. 4.9 as $\rho_i \equiv \rho(t_i)$ with i = 0,1,2.

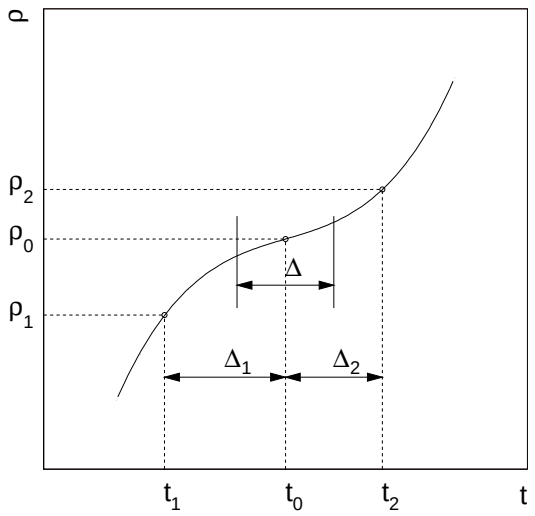

Figure 4.9: Definition of measured variables used in Eqs. 4.9 and 4.12

The generalization of the method for the two independent variables is straightforward as the total correction is the sum of the p_T and x_F corrections.

The systematic uncertainty introduced by this correction is defined by the error of the neighbouring points. It amounts of about 10 times less than the statistical error of the points themselves. The direct application of the correction makes it model or parametrization independent.

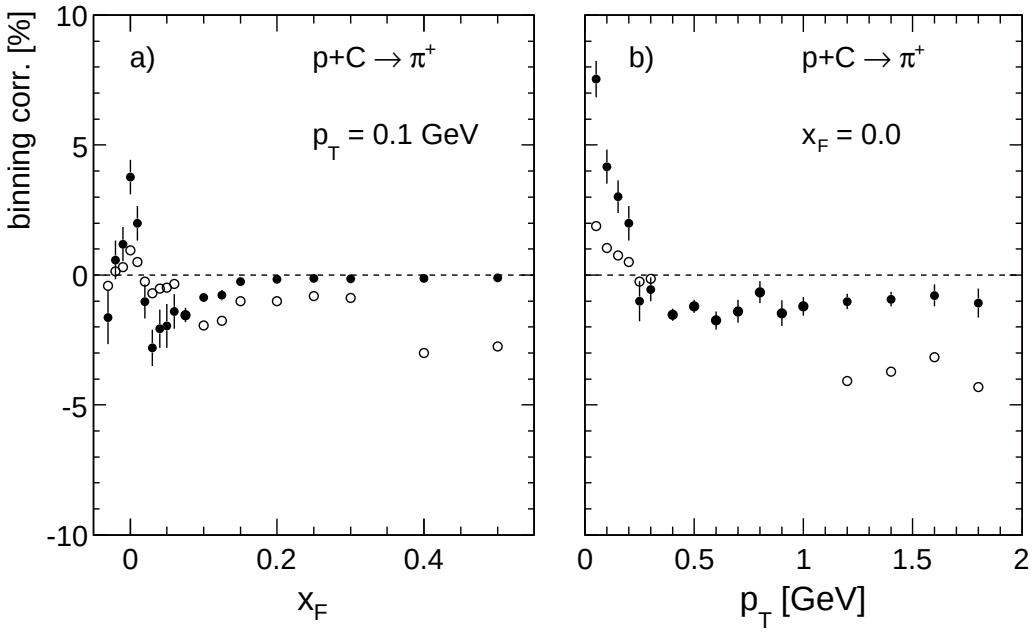

Figure 4.10: Binning correction in p+C in a) x_F and b) p_T. Full circles represent the correction for a fixed bin sizes of $\Delta x_F = 0.02$ and $\Delta p_T = 0.1$ GeV/c, respectively and open circles the correction with actual bin sizes used

The resulting correction reaches up to 5%. In Fig. 4.10 is shown an example of binning correction in p+C. The correction is very similar in both reaction p+p and p+C because the density distributions don't differ much. The remaining systematic error from neglecting the higher order terms is below 0.5% as verified by Monte Carlo.

4.5 Systematic errors

The main source of systematic uncertainty of the cross section is the overall normalization. In addition to this the corrections regarded in the previous sections introduce systematic errors which are estimated allowing appropriate error bands for the underlying physics inputs. The corresponding systematic errors are given in Table 4.2. The upper limit of

Reaction	p+p	p+C
Normalization	1.5%	2.5%
Tracking efficiency	0.5%	0.5%
Trigger bias	0.5%	1%
Feed-down	0.5-1.5%	1-2.5%
Detector absorption Pion decay $\pi \to \mu + \nu_\mu$ Secondary interactions in the target	0.5%	0.5%
Binning	0.3%	0.5%
Total(upper limit)	4.8%	7.5%
Total(quadratic sum)	2.0%	3.8%

Table 4.2: Systematic errors

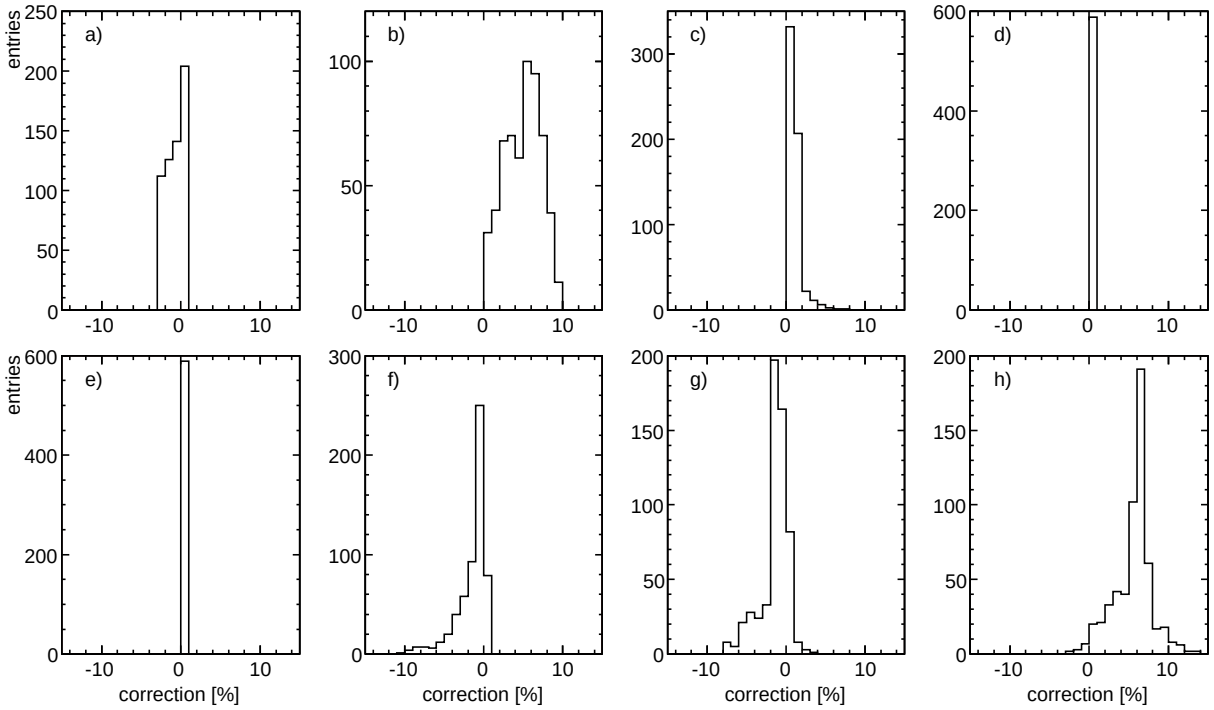

Figure 4.11: Distribution of the corrections in p+p reaction for a) secondary interactions in the target, b) trigger bias, c) absorption in the detector material, d) pion decay, e) empty target contribution, f) feed-down, g) binning and h) total

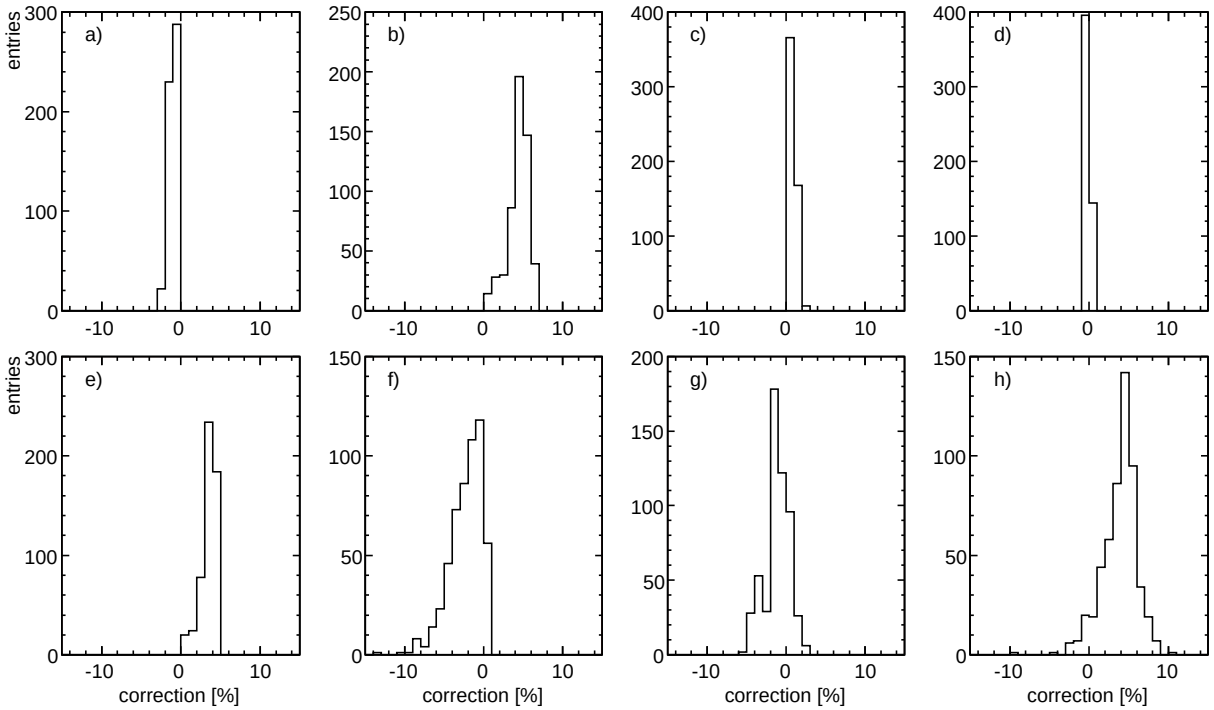

Figure 4.12: Distribution of the corrections in p+C reaction for a) secondary interactions in the target, b) trigger bias, c) absorption in the detector material, d) pion decay, e) empty target contribution, f) feed-down, g) binning and h) total

4.8% and 7.5% for p+p and p+C, respectively, can be claimed, obtained by summing up all contributions.

It should be noted that in high x_F region and in the backward hemisphere in p+C additional systematic uncertainties have to be added. In high x_F region a certain assumption about K/π and e/π ratios have to be made for realistic particle identification which introduce uncertainty between 1 and 3%. In the backward bins in p+C, where the reflection method was used, a systematic uncertainty is between 1 and 3%. This uncertainty is due mostly on the forward-backward correction factor for the protons and kaons and it increases for the more negative x_F with increasing of the proton content.

Further information on the different corrections in p+p and p+C reactions is given in Figures 4.11 and 4.12, respectively, where in each panel the distribution of single corrections and the resulting total correction for the all data points is presented. In both reactions appear that individual corrections compensate to a large extent and the resulting total correction reaches 10% only in few cases.

Chapter 5

Double differential invariant distributions

In this chapter the double differential invariant cross sections for charged pion are presented. The cross section has been extracted following dE/dx fitting and correction procedures described in preceding chapters. The data are given numerically in tables. The measured data points together with interpolation curves are presented in p_T distribution at fixed x_F, in x_F distributions at fixed p_T, and in corresponding π^+/π^- ratio distributions. A comparison with existing measurements at the SPS energy range is made.

5.1 Data tables and interpolation

The double differential invariant cross section for charged pion production in p+p and p+C collisions as a function of x_F and p_T following the binning schemes defined in Sect. 3.2 are given in the tables below. The measured values together with the corresponding errors for π^+ in p+p are summarized in Table 5.1, for π^- in p+p in Table 5.2, for π^+ in p+C in Table 5.4, for π^- in p+C in Table 5.4.

In p+p reaction data cover the x_F region between 0 and 0.55 for all p_T up to 2 GeV/c. The measurement for π^- is extended up to $x_F = 0.85$ which is possible because of the rapidly decreasing ratio $(K^-+\overline{p})/\pi^-$ in the forward region. This ratio has been determined from the previous measurements [20] and [21]. A similar extraction of the π^+ cross section in this region can not be made due to the dominant proton component.

The measurement in p+C was extended as much as possible in the backward hemisphere in order to study the target fragmentation region. The data cover x_F range between -0.1 and 0.5 and p_T range between 0 and 1.8 GeV/c.

Although the bins were chosen in such a way that bin centers correspond to well defined x_f and p_T values, it is desirable to have an internal extension of the data in non-measurable intermediate values which can be used for comparison with other experiments. For this purpose the interpolation scheme which produces smooth overall x_F and p_T dependences was developed. Such a numerical interpolation faces the problem that the dense phase space coverage and small statistical errors of the data reveals a complex micro-structures in both x_F and p_T distributions which makes practically impossible to describe data with analytical expressions. For this reason a multistep interpolation method is selected which relies on local continuity of the cross section in both x_F and p_T. This interpolation complies with statistical accuracy of the data points, as demonstrated in Fig. 5.1.

	$f(x_F, p_T)$ Δf								
$p_T \backslash x_F$	0.0	0.01	0.02	0.025	0.03	0.04	0.05	0.06	0.07
0.05	62.87 0.61	62.79 0.66	59.44 0.65		51.53 0.63	43.29 0.63	37.64 0.75	32.64 0.86	29.78 0.98
0.1	59.66 0.58	58.91 0.62	54.55 0.48		51.49 0.54	45.19 0.54	41.09 0.63	36.46 0.73	32.92 0.81
0.15	51.20 0.55	50.87 0.58	47.98 0.55		45.66 0.58	42.21 0.48	39.68 0.54	36.39 0.59	34.55 0.67
0.2	41.42 0.65	40.78 0.49	39.58 0.51		37.37 0.56	35.33 0.54	33.69 0.50	31.49 0.58	29.16 0.63
0.25	32.00 0.57	31.93 0.53	30.47 0.55		29.47 0.61	27.77 0.53	26.54 0.60	25.04 0.68	23.80 0.63
0.3	24.11 0.49	23.89 0.62	23.03 0.60		22.00 0.67	21.35 0.69	20.37 0.62	19.44 0.71	18.71 0.68
0.4	13.20 0.57	13.21 0.57	12.76 0.58		12.11 0.61		11.56 0.43		
0.5	7.212 0.77	7.297 0.78	7.046 0.80		6.690 0.85		6.423 0.59		
0.6	4.102 1.02	3.920 1.07	3.923 1.06		3.723 1.11		3.585 0.77		
0.7	2.219 1.41	2.233 1.40	2.170 1.43		2.027 1.52		2.007 1.01		
0.8	1.213 1.86	1.259 1.87	1.183 1.89		1.148 1.94		1.156 1.30		
0.9	0.689 2.49	0.681 2.51	0.702 2.43		0.692 2.47		0.652 1.96		
1.0	0.386 3.31	0.397 3.22	0.383 3.33		0.383 3.32		0.379 2.54		
1.1	0.248 2.60			0.236 3.48			0.223 3.35		
1.2	0.136 3.54			0.135 4.57			0.120 4.32		
1.3	0.0797 4.56			0.0750 6.07			0.0729 5.55		
1.4	0.0482 5.99			0.0448 8.04			0.0443 6.97		
1.5	0.0296 7.61			0.0277 9.96			0.0302 8.45		
1.7	0.0122 6.14						0.0115 6.76		
1.9	0.00406 10.2						0.00373 11.9		
2.1	0.00172 15.4						0.00149 18.8		

$p_T \backslash x_F$	0.075	0.08	0.1	0.12	0.15	0.2	0.25	0.3	0.35
0.05		27.71 1.07	24.05 0.92	22.01 1.04	19.13 0.92	17.35 1.08	15.80 1.57	11.80 2.06	7.690 2.75
0.1		29.30 0.91	25.11 0.77	22.98 0.89	20.40 0.78	16.72 0.93	14.59 1.35	11.23 1.81	6.811 2.11
0.15		30.72 0.75	26.17 0.63	23.42 0.75	20.15 0.65	16.16 0.78	12.87 1.16	9.319 1.68	5.970 1.82
0.2		27.80 0.67	24.38 0.59	21.57 0.67	18.40 0.59	13.64 0.73	10.84 1.10	7.535 1.57	5.169 1.67
0.25		22.94 0.66	20.16 0.59	18.06 0.67	15.33 0.57	11.59 0.71	8.601 1.17	6.478 1.55	4.354 1.62
0.3		18.18 0.71	16.19 0.60	14.57 0.67	12.59 0.58	9.413 0.72	7.164 1.14	5.146 1.57	3.659 1.61
0.4	10.89 0.35		10.00 0.42		8.047 0.40	6.189 0.61	4.754 0.85	3.514 1.16	2.590 1.18
0.5	6.033 0.62		5.749 0.50		5.026 0.46	4.040 0.68	3.204 0.93	2.367 1.25	1.812 1.28
0.6	3.356 0.79		3.186 0.64		2.874 0.65	2.561 0.77	2.071 1.06	1.681 1.38	1.313 1.38
0.7	1.924 1.11		1.770 1.02		1.623 0.83	1.452 1.02	1.272 1.25	1.006 1.63	0.863 1.58
0.8	1.082 1.38		1.027 1.45		0.905 1.04	0.806 1.29	0.697 1.58	0.608 1.98	0.490 1.96
0.9	0.607 1.93		0.576 2.03		0.516 1.35	0.471 1.63	0.398 2.01	0.304 2.64	0.281 2.47
1.0	0.368 2.62		0.356 2.40		0.298 1.71	0.252 2.14	0.219 2.56	0.181 3.27	0.158 3.14
1.1	0.219 3.42		0.203 3.67		0.176 2.41	0.155 2.72	0.130 3.18	0.113 3.98	0.0802 4.16
1.2	0.128 4.17		0.125 4.27		0.106 3.36	0.0876 3.49	0.0739 4.11	0.0555 5.46	0.0497 5.09
1.3	0.0734 5.67		0.0701 6.07		0.0653 4.54	0.0530 4.47	0.0482 5.16	0.0405 6.20	0.0274 6.74
1.4	0.0473 6.58		0.0416 7.65		0.0405 5.59	0.0295 7.45	0.0246 6.72	0.0234 7.92	0.0169 8.28
1.5	0.0266 9.20		0.0290 9.23		0.0258 7.49	0.0204 7.79	0.0179 9.45	0.0138 4.93	0.0110 7.01
1.7			0.00981 7.56		0.0114 7.78	0.00720 9.78	0.00615 10.5	0.00527 7.69	0.00448 10.5
1.9			0.00339 12.7		0.00374 13.9	0.00323 13.7		0.00273 10.3	0.00209 17.7
2.1					0.00215 17.3	0.00151 22.6			0.00110 24.5

$p_T \backslash x_F$	0.45	0.55
0.05	3.720 3.18	
0.1	3.734 2.23	
0.15	3.266 1.94	
0.2	2.812 1.82	1.683 2.32
0.25	2.435 1.75	
0.3	1.970 1.79	1.198 2.18
0.4	1.388 1.29	0.853 3.58
0.5	0.949 1.37	0.538 3.94
0.6	0.660 1.49	0.349 4.59
0.7	0.482 1.67	0.227 5.29
0.8	0.305 1.98	0.148 6.20
0.9	0.188 2.39	0.0956 7.24
1.0	0.101 3.10	0.0592 8.74
1.1	0.0514 4.07	0.0326 7.89
1.2	0.0290 5.27	
1.3	0.0189 6.38	0.00724 15.1
1.4	0.0116 7.74	
1.5	0.00612 8.78	0.00214 26.7
1.7	0.00315 11.8	

Table 5.1: Double differential invariant cross section $f(x_F, p_T)$ [mb/(GeV^2/c^3)] for π^+ produced in p+p interactions at 158 GeV/c. The statistical uncertainty Δf is given in %

	$f(x_F, p_T)$ Δf								
$p_T \backslash x_F$	0.0	0.01	0.02	0.025	0.03	0.04	0.05	0.06	0.07
0.05	59.19 0.52	55.36 0.57	49.58 0.69		41.35 0.70	35.72 0.67	30.52 0.81	26.76 0.93	23.79 1.05
0.1	54.40 0.48	52.21 0.52	47.69 0.49		41.32 0.57	35.95 0.59	31.55 0.71	27.53 0.81	24.76 0.91
0.15	46.74 0.47	45.73 0.48	41.85 0.57		37.78 0.63	34.21 0.51	30.42 0.61	27.50 0.68	24.47 0.77
0.2	37.85 0.53	36.91 0.51	34.65 0.55		31.96 0.62	29.26 0.57	26.45 0.55	24.03 0.65	22.16 0.71
0.25	29.00 0.59	28.74 0.55	26.68 0.59		25.41 0.66	23.56 0.58	21.70 0.68	19.90 0.74	18.51 0.69
0.3	22.02 0.68	22.25 0.67	20.62 0.67		19.51 0.70	18.26 0.75	16.87 0.69	15.98 0.79	14.91 0.71
0.4	12.28 0.61	12.05 0.62	11.63 0.55		10.75 0.59		10.05 0.45		
0.5	6.673 0.80	6.371 0.83	6.296 0.84		5.946 0.91		5.697 0.63		
0.6	3.498 1.10	3.542 1.11	3.507 1.12		3.261 1.20		3.147 0.81		
0.7	2.016 1.44	1.959 1.47	1.893 1.51		1.852 1.55		1.705 1.06		
0.8	1.098 1.95	1.089 1.96	1.101 1.94		1.049 2.03		0.982 1.41		
0.9	0.641 2.51	0.616 2.59	0.622 2.57		0.570 2.80		0.567 2.08		
1.0	0.346 3.37	0.372 3.43	0.341 3.43		0.336 3.48		0.318 2.68		
1.1	0.209 3.09			0.215 3.64			0.190 3.35		
1.2	0.122 3.67			0.117 4.91			0.111 4.52		
1.3	0.0784 4.64			0.0686 6.49			0.0597 6.04		
1.4	0.0469 5.91			0.0411 8.23			0.0372 7.76		
1.5	0.0242 8.33			0.0262 10.5			0.0232 9.59		
1.7	0.0102 6.25						0.00785 8.09		
1.9	0.00399 10.3						0.00344 12.2		
2.1	0.00124 27.4						0.00162 17.7		

$p_T \backslash x_F$	0.075	0.08	0.1	0.12	0.15	0.2	0.25	0.3	0.35
0.05		21.27 1.19	17.41 1.04	14.35 1.26	11.31 1.16	7.564 1.55	6.064 2.36	4.669 3.32	3.007 4.44
0.1		21.39 1.06	17.17 0.90	14.49 1.08	11.40 1.02	7.652 1.33	5.802 1.97	4.429 2.94	2.964 3.17
0.15		21.66 0.87	17.62 0.78	14.45 0.96	11.23 0.84	7.367 1.11	5.539 1.63	3.971 2.51	2.712 2.66
0.2		20.30 0.79	16.41 0.71	13.62 0.87	10.63 0.76	6.743 1.00	4.839 1.51	3.453 2.30	2.191 2.57
0.25		17.28 0.80	14.32 0.67	12.03 0.81	9.195 0.73	5.986 0.95	4.334 1.52	2.872 2.31	2.152 2.30
0.3		13.89 0.77	12.27 0.70	10.08 0.75	8.226 0.71	5.279 0.92	3.795 1.47	2.538 2.21	1.689 2.37
0.4	8.853 0.39		7.674 0.48		5.567 0.48	3.892 0.76	2.741 1.06	1.914 1.57	1.286 1.66
0.5	5.069 0.67		4.524 0.57		3.485 0.54	2.646 0.83	1.908 1.14	1.366 1.66	0.927 1.75
0.6	2.849 0.86		2.564 0.71		2.133 0.75	1.670 0.96	1.258 1.28	0.958 1.82	0.676 1.89
0.7	1.616 1.19		1.492 1.15		1.225 0.92	1.010 1.20	0.788 1.50	0.600 2.13	0.441 2.18
0.8	0.940 1.48		0.867 1.60		0.686 1.18	0.590 1.49	0.474 1.84	0.364 2.55	0.265 2.63
0.9	0.529 2.02		0.472 2.25		0.401 1.48	0.328 1.90	0.270 2.29	0.226 3.07	0.165 3.15
1.0	0.307 2.79		0.264 2.81		0.234 1.88	0.181 2.45	0.159 2.86	0.133 3.80	0.0971 3.89
1.1	0.181 3.53		0.174 3.68		0.139 2.69	0.115 2.99	0.0880 3.71	0.0779 4.77	0.0553 4.90
1.2	0.0982 5.38		0.105 5.10		0.0803 3.65	0.0680 3.78	0.0514 4.67	0.0421 6.38	0.0332 6.14
1.3	0.0582 6.39		0.0606 6.51		0.0499 4.99	0.0401 4.80	0.0332 5.63	0.0247 7.93	0.0187 7.93
1.4	0.0329 8.41		0.0420 7.67		0.0320 6.09	0.0225 7.27	0.0186 7.35	0.0136 10.7	
1.5	0.0212 10.5		0.0201 11.1		0.0196 8.76	0.0131 9.13	0.0137 10.5	0.00879 6.22	0.00676 6.13
1.7			0.00868 8.05		0.00885 8.78	0.00488 11.1	0.00466 11.2	0.00338 9.64	0.00276 9.43
1.9			0.00254 14.6		0.00255 16.5	0.00197 17.0		0.00114 16.5	
2.1					0.00071 30.9	0.00101 23.3			

$p_T \backslash x_F$	0.45	0.55	0.65	0.75	0.85				
0.05	1.418 5.09								
0.1	1.494 3.52	0.528 5.91	0.221 7.4	0.0588 15.8	0.0259 25.0				
0.15	1.300 3.07								
0.2	1.191 2.79	0.550 4.20							
0.25	0.978 2.71								
0.3	0.875 2.28	0.432 3.90	0.149 5.1	0.0409 10.6	0.0111 21.8				
0.4	0.637 2.30	0.267 4.23							
0.5	0.429 2.49	0.194 4.46	0.0582 6.3	0.0199 11.5	0.00421 26.7				
0.6	0.305 2.68	0.133 4.88							
0.7	0.211 2.99	0.0821 5.73	0.0282 7.9	0.00742 16.0	0.00236 30.0				
0.8	0.135 3.55	0.0627 6.15							
0.9	0.0840 4.22	0.0345 7.78	0.0142 9.5	0.00250 24.3	0.00116 37.6				
1.0	0.0524 5.34	0.0185 10.1							
1.1	0.0315 5.41	0.0126 8.19	0.00517 14.3	0.00185 25.8	0.00014 100				
1.3	0.0103 6.39	0.00463 12.6	0.00161 23.5	0.00074 37.3	0.00012 100				
1.5	0.00439 8.92	0.00104 24.9	0.00048 41.7	0.00019 68.4					
1.7	0.00127 17.6	0.00052 33.2	0.00014 71.4						

Table 5.2: Double differential invariant cross section $f(x_F, p_T)$ [mb/(GeV^2/c^3)] for π^- produced in p+p interactions at 158 GeV/c. The statistical uncertainty Δf is given in %

$f(x_F, p_T), \Delta f$									
$p_T \backslash x_F$	-0.1	-0.075	-0.05	-0.04	-0.03	-0.025	-0.02	-0.01	0.0
0.05							589.8 2.41	616.9 2.50	652.3 1.59
0.1					584.0 2.62		611.0 1.77	587.3 1.59	581.7 1.68
0.15				445.2 2.80	488.4 1.89		509.8 1.81	502.0 1.66	508.2 1.55
0.2			353.4 2.99	365.7 2.70	385.2 1.93		403.2 1.85	382.1 1.77	411.9 1.65
0.25			268.6 3.20	284.5 2.55	308.2 2.28		287.1 2.14	300.3 1.97	302.2 1.89
0.3		172.2 2.43	214.8 3.82	197.6 3.34	225.8 2.64		222.9 2.37	216.7 2.23	228.4 2.12
0.4	86.5 3.32	106.4 3.33	121.2 3.10	117.8 2.80	118.1 2.41		117.0 2.24	116.9 2.24	121.0 1.81
0.5	53.0 4.63	56.6 4.00	66.6 4.06	65.4 3.69	63.6 3.41		63.0 2.57	71.9 2.38	68.0 2.43
0.6	32.7 5.14	29.7 5.46	35.3 5.54	34.1 3.66	36.7 3.41		37.1 3.31	36.8 3.28	36.6 3.32
0.7	18.3 6.82	19.6 6.43	21.9 5.03	19.30 4.78	20.13 4.59		22.73 4.26	20.11 4.49	21.28 4.28
0.8	11.76 7.85	11.22 7.91	11.39 4.46			11.61 3.82			13.35 3.53
0.9	6.65 9.43	5.91 7.49	6.97 5.71			6.72 4.95			7.43 4.52
1.0	3.92 8.52	3.79 8.19	4.16 6.91			4.43 6.03			4.17 6.42
1.2	1.19 10.5	1.59 9.19	1.80 7.44			1.62 6.91			1.285 7.73
1.4	0.545 10.0		0.530 8.5						0.541 8.47
1.6	0.244 15.3		0.226 13.3						0.275 12.0
1.8	0.096 21.3		0.065 24.7						0.107 18.8

$p_T \backslash x_F$	0.01	0.02	0.025	0.03	0.04	0.05	0.06	0.075	0.1
0.05	620.4 1.75	555.9 2.03		432.9 2.10	390.7 2.01	334.4 2.41	293.4 2.81	249.6 2.34	186.3 2.76
0.1	561.5 1.62	515.0 1.51		451.6 1.69	401.9 1.74	353.7 2.04	311.8 2.39	249.7 2.10	195.6 2.45
0.15	488.0 1.52	451.4 1.59		407.1 1.87	360.3 1.51	324.8 1.76	287.8 2.07	247.8 1.69	197.1 2.03
0.2	377.0 1.62	373.1 1.58		322.5 1.89	300.2 1.74	276.8 1.66	254.2 1.91	222.0 1.59	180.0 1.85
0.25	303.3 1.73	276.3 1.73		263.0 1.90	237.6 1.83	224.7 1.94	211.0 2.19	188.8 1.52	157.5 1.69
0.3	222.1 1.97	209.5 1.98		199.6 2.07	185.9 2.34	174.1 2.13	172.3 2.29	152.1 1.59	127.5 1.76
0.4	122.2 1.79	119.6 1.75		109.7 1.90		98.3 1.39		91.0 1.34	79.4 1.39
0.5	69.8 2.42	64.5 2.54		65.2 2.61		57.4 1.89		53.2 2.01	48.73 1.62
0.6	38.0 3.25	36.8 3.34		35.7 3.44		32.88 2.39		29.98 2.56	28.95 1.98
0.7	21.10 4.28	20.32 4.43		19.74 4.56		19.31 3.06		18.06 3.40	16.10 2.30
0.8			11.28 3.72			12.03 3.84		11.09 4.17	9.69 3.15
0.9			6.82 4.89			5.57 6.32		6.28 5.61	5.61 4.30
1.0			4.30 6.19			3.61 7.93		3.50 8.18	3.45 5.43
1.2			1.228 7.83			1.48 8.21		1.33 8.96	1.220 6.85
1.4						0.512 9.62			0.479 10.8
1.6						0.223 14.3			0.225 15.4
1.8						0.062 32.4			0.113 19.2

$p_T \backslash x_F$	0.125	0.15	0.2	0.25	0.3	0.4	0.5		
0.05	165.1 3.39	140.3 3.11	111.4 3.59	96.9 4.47	77.8 5.33	39.6 7.63			
0.1	160.5 3.00	147.9 2.69	103.1 3.26	83.7 3.26	63.5 5.38	36.7 5.56	20.5 8.14		
0.15	161.6 2.48	131.2 2.36	104.3 2.80						
0.2	146.8 2.28	124.3 2.16	86.0 2.58	62.4 2.76	45.1 4.36	25.4 4.61	14.54 6.79		
0.25	130.8 2.04	108.7 1.99	72.9 2.52						
0.3	104.7 2.16	90.2 2.00	67.8 2.38	46.1 2.79	30.9 4.32	17.19 4.53	9.73 6.74		
0.4	68.7 1.64	62.34 1.50	45.50 2.06	33.00 2.84	23.63 4.21	12.21 4.61	6.98 6.93		
0.5	41.95 1.95	39.51 1.68	29.98 2.28	22.82 3.11	14.82 4.76	9.29 4.73	3.21 9.15		
0.6	24.95 2.29	23.46 2.35	18.43 2.62	16.02 3.29	11.81 4.84	5.86 5.67	2.85 8.76		
0.7		13.76 2.55	10.88 3.44						
0.8		8.33 3.17	6.72 4.28	6.30 3.32	4.51 4.87	2.56 5.18	1.49 7.43		
0.9		4.55 4.07	4.28 4.97						
1.0		2.95 4.87	2.43 6.37	2.11 5.14	1.52 7.57	0.812 8.23	0.496 11.6		
1.2		0.992 6.32	0.936 6.68	0.639 8.72	0.585 11.4	0.313 12.0	0.190 17.4		
1.4			0.358 8.33		0.268 11.2	0.136 17.2	0.078 25.3		
1.6			0.187 11.4		0.093 18.0	0.036 32.0			
1.8			0.059 23.6						

Table 5.3: Double differential invariant cross section $f(x_F, p_T)$[mb/(GeV^2/c^3)] for π^+ in p+C interaction at 158 GeV/c. The statistical uncertainty is given in %

$f(x_F, p_T), \Delta f$									
$p_T \backslash x_F$	-0.1	-0.075	-0.05	-0.04	-0.03	-0.025	-0.02	-0.01	0.0
0.05							541.6 2.35	646.3 2.19	602.6 1.57
0.1					525.3 2.11		595.9 1.74	601.7 1.48	579.8 1.43
0.15				426.5 2.81	481.8 1.88		511.6 1.69	469.1 1.60	498.6 1.39
0.2			345.9 3.01	364.0 2.74	372.4 1.97		373.7 1.80	374.9 1.68	367.2 1.66
0.25			250.1 3.30	275.0 2.53	294.5 2.00		289.2 1.96	285.9 1.91	296.1 1.78
0.3		160.4 1.77	194.6 3.50	197.4 2.89	215.5 2.34		217.1 2.22	210.9 2.18	214.0 2.06
0.4	86.2 3.33	103.3 2.58	112.8 2.75	115.3 2.49	115.2 2.09		110.7 2.17	118.6 2.03	125.7 1.75
0.5	52.8 3.62	55.8 3.24	64.6 3.53	63.0 3.29	63.3 2.80		64.7 2.54	63.5 3.03	64.4 2.50
0.6	31.2 3.99	31.7 4.10	32.7 4.91	35.5 3.61	36.6 3.43		34.2 3.47	35.5 3.35	32.1 3.51
0.7	18.5 5.01	19.4 5.14	19.0 5.45	19.31 4.79	20.88 4.44		20.31 4.44	20.02 4.42	20.30 4.48
0.8	10.64 6.32	10.38 6.41	11.76 4.68			11.74 3.77			11.12 3.81
0.9	5.98 7.84	6.63 7.38	6.64 5.63			6.66 4.98			6.72 4.95
1.0	3.84 8.72	3.83 8.14	3.79 7.56			4.21 6.32			3.78 6.43
1.2	1.29 10.2	1.46 9.30	1.26 8.87			1.30 7.78			1.246 8.62
1.4	0.491 10.6		0.506 8.94						0.582 8.21
1.6	0.205 15.8		0.189 14.8						0.184 14.3
1.8	0.093 21.4		0.101 19.7						0.075 22.4
$p_T \backslash x_F$	0.01	0.02	0.025	0.03	0.04	0.05	0.06	0.075	0.1
0.05	576.1 1.71	469.0 2.17		387.0 2.13	336.6 2.15	265.9 2.63	225.5 3.11	200.6 2.60	150.2 3.06
0.1	539.5 1.58	464.9 1.54		387.9 1.79	316.2 1.93	275.2 2.30	246.7 2.58	205.1 2.28	146.6 2.76
0.15	445.0 1.50	407.0 1.64		353.7 2.00	314.0 1.64	262.3 1.96	238.0 2.17	187.4 1.95	148.8 2.18
0.2	362.0 1.56	320.5 1.69		294.7 1.98	269.1 1.85	230.8 1.87	205.8 2.11	180.8 1.80	131.7 2.14
0.25	274.0 1.75	256.7 1.86		235.6 2.03	210.3 1.85	192.3 2.15	171.8 2.41	147.1 1.78	109.4 1.99
0.3	218.1 2.01	189.2 2.07		173.0 2.26	163.8 2.53	150.6 2.32	132.1 2.64	125.0 1.75	96.1 2.03
0.4	113.0 1.93	107.0 1.85		101.8 1.97		91.7 1.45		74.2 1.50	62.1 1.59
0.5	61.0 2.58	59.1 2.66		58.6 2.76		52.5 1.99		44.9 2.20	38.85 1.81
0.6	35.2 3.37	33.4 3.53		28.5 3.91		28.46 2.61		26.50 2.65	23.85 2.22
0.7	18.92 4.53	18.74 4.68		17.40 4.91		17.13 3.32		15.10 3.77	13.10 2.66
0.8			10.58 3.96			9.07 4.35		8.98 4.65	7.62 3.43
0.9			6.44 5.14			5.64 6.23		5.06 6.06	4.36 5.00
1.0			3.28 6.71			3.84 7.43		2.83 9.23	2.63 6.22
1.2			1.376 7.42			1.03 9.86		1.06 10.1	1.007 7.38
1.4						0.440 10.6			0.449 11.0
1.6						0.150 18.3			0.197 16.3
1.8						0.050 36.2			0.064 28.7
$p_T \backslash x_F$	0.125	0.15	0.2	0.25	0.3	0.4	0.5		
0.05	111.9 3.92	86.1 3.94	55.1 5.14	41.4 6.81	33.3 8.22	12.1 13.6			
0.1	117.8 3.44	81.8 3.66	58.1 4.55	41.8 4.75	29.4 7.69	10.8 10.2	5.1 16.2		
0.15	111.0 2.92	83.1 2.86	51.4 3.80						
0.2	98.8 2.64	81.9 2.54	53.5 3.27	30.7 3.96	22.7 6.11	9.6 7.61	4.34 12.4		
0.25	90.7 2.42	72.7 2.41	42.6 3.28						
0.3	73.4 2.57	58.2 2.49	39.3 3.09	25.9 3.72	17.2 5.71	7.69 6.83	3.23 11.8		
0.4	50.5 1.92	42.19 1.79	28.69 2.55	18.31 3.77	12.21 5.83	5.33 7.03	2.10 13.0		
0.5	31.78 2.23	27.36 2.03	21.15 2.72	14.13 3.93	9.79 5.88	3.83 7.61	1.57 13.3		
0.6	19.02 2.67	17.09 2.71	12.00 3.30	9.28 4.51	6.12 6.83	3.07 7.43	0.97 15.1		
0.7		10.30 2.99	7.40 4.17						
0.8		5.97 3.68	5.12 4.74	3.75 4.29	2.60 6.45	1.20 7.56	0.56 12.0		
0.9		3.60 4.57	2.65 6.31						
1.0		2.28 5.58	1.73 7.50	1.45 6.22	0.95 9.62	0.588 9.57	0.189 15.2		
1.2		0.727 7.42	0.674 7.96	0.540 9.49	0.392 13.7	0.173 16.9	0.077 27.1		
1.4			0.293 9.42		0.150 14.3	0.063 25.7	0.031 39.6		
1.6			0.106 14.0		0.064 21.6	0.026 32.3			
1.8			0.037 24.4						

Table 5.4: Double differential invariant cross section $f(x_F, p_T)$[mb/(GeV^2/c^3)] for π^- in p+C interaction at 158 GeV/c. The statistical uncertainty is given in %

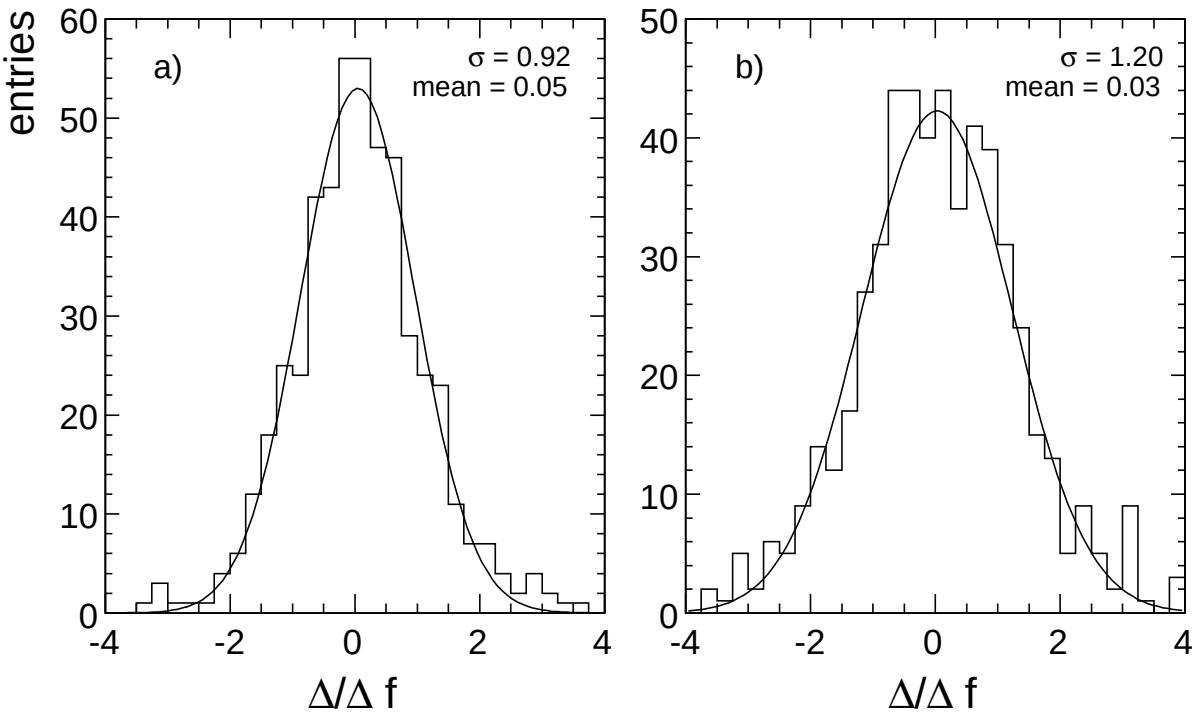

Figure 5.1: Histogram of the difference Δ between the measured invariant cross section and the corresponding interpolation values (combined for π^+ and π^-) divided by the experimental uncertainty Δf for a) p+p and b) p+C

5.2 Invariant p_T and x_F distributions

The invariant cross sections as a function of p_T at several fixed x_F values are presented in Fig. 5.2 for p+p interactions and Fig. 5.3 for p+C collisions. The lines show the interpolated curves.

The p_T distributions in both p+p and p+C reaction can not be described with simple exponential parametrization at any x_F value, as the slope changes with transverse momentum. In addition to this the structure appeared in low p_T region and $x_F < 0.3$ and in the p_T region from 0.5 to 1 GeV/c for $x_F > 0.25$. The structures in low p_T region are presented in more details in the linear scale of Fig. 5.4 where a maximum at $p_T = 0.15$ GeV/c is found to develop in the x_F region between 0.03 and 0.2 for both reactions. This maximum is more pronounced for π^+ than for π^- and in p+p than in p+C interactions.

In the next two figures the x_F invariant distribution at fixed p_T values are presented. In Fig. 5.5 the x_F distribution of produced pions in p+p interactions are shown starting from $x_F = 0$ up to the measuring limit of the experiment. The x_F distributions of produced pions in p+C interactions are shown in Fig. 5.6. In contrast to p+p the p+C reaction is not forward-backward symmetric and for this reason the measurement is extended in the backward region as much as possible. The maximum of the distribution is displaced into the backward region for all p_T values which can be explained by the bigger target component. Again structures in the distributions are found to develop for both interactions in the low p_T region. A complicated pattern is seen as the p_T distribution below 0.3 GeV/c cross each other in the x_F region between 0.03 and 0.2. The cross-over can be connected with the maxima seen in the p_T distributions.

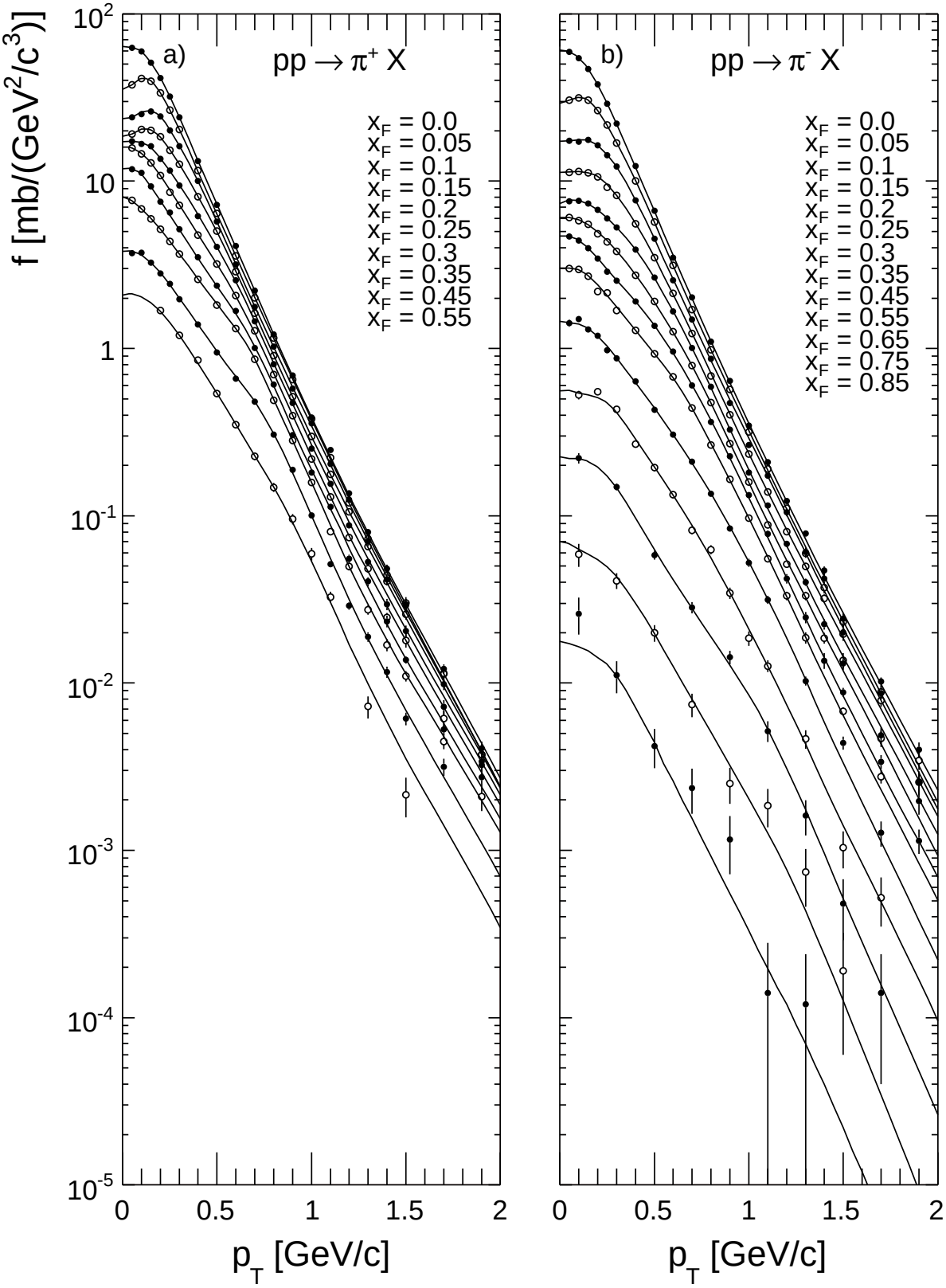

Figure 5.2: Invariant cross section in p+p at 158 GeV/c beam momentum as a function of p_T at several fixed x_F values for a) π^+ and b) π^-

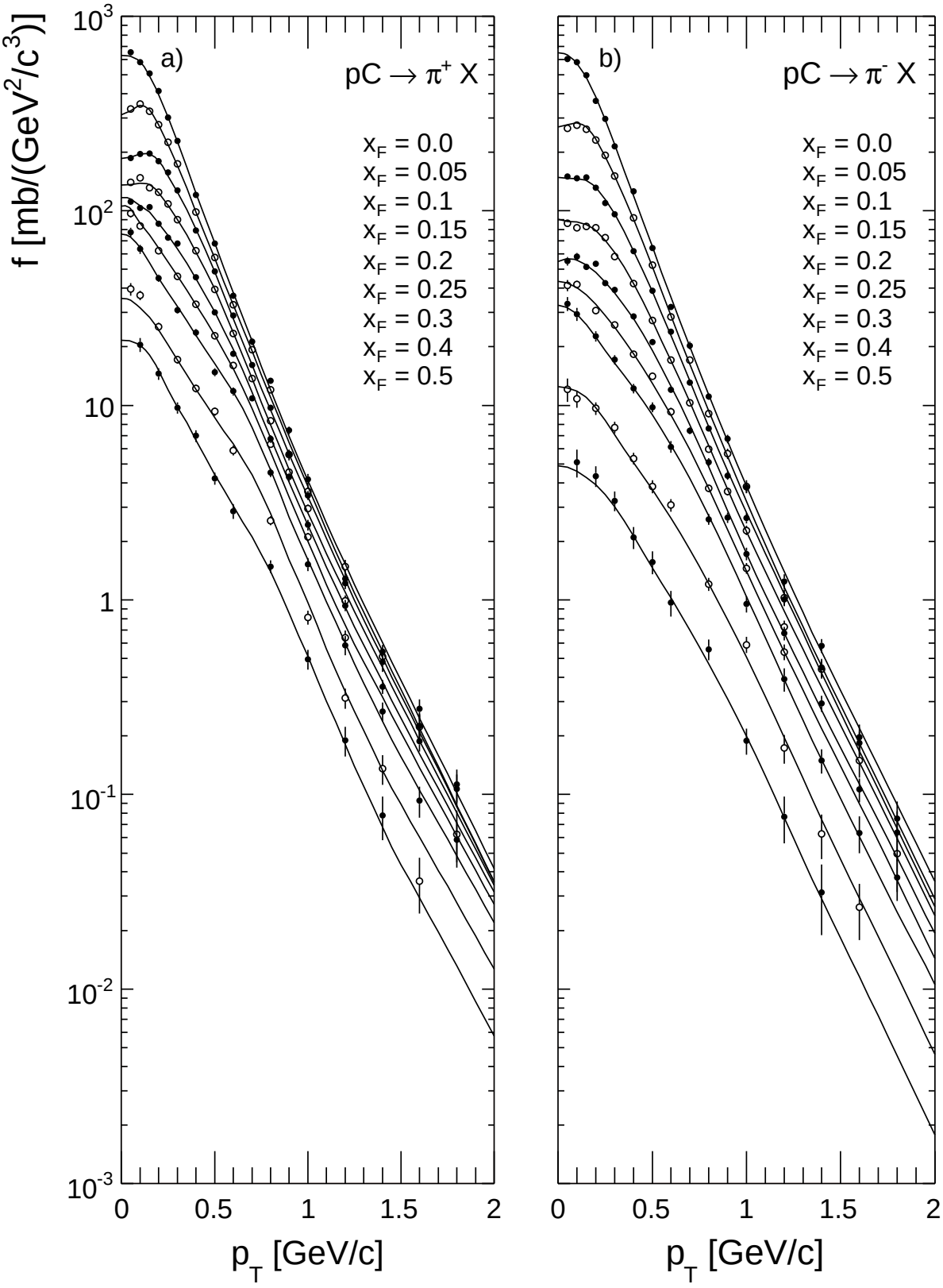

Figure 5.3: Invariant cross section in p+C at 158 GeV/c beam momentum as a function of p_T at several fixed x_F values for a) π^+ and b) π^-

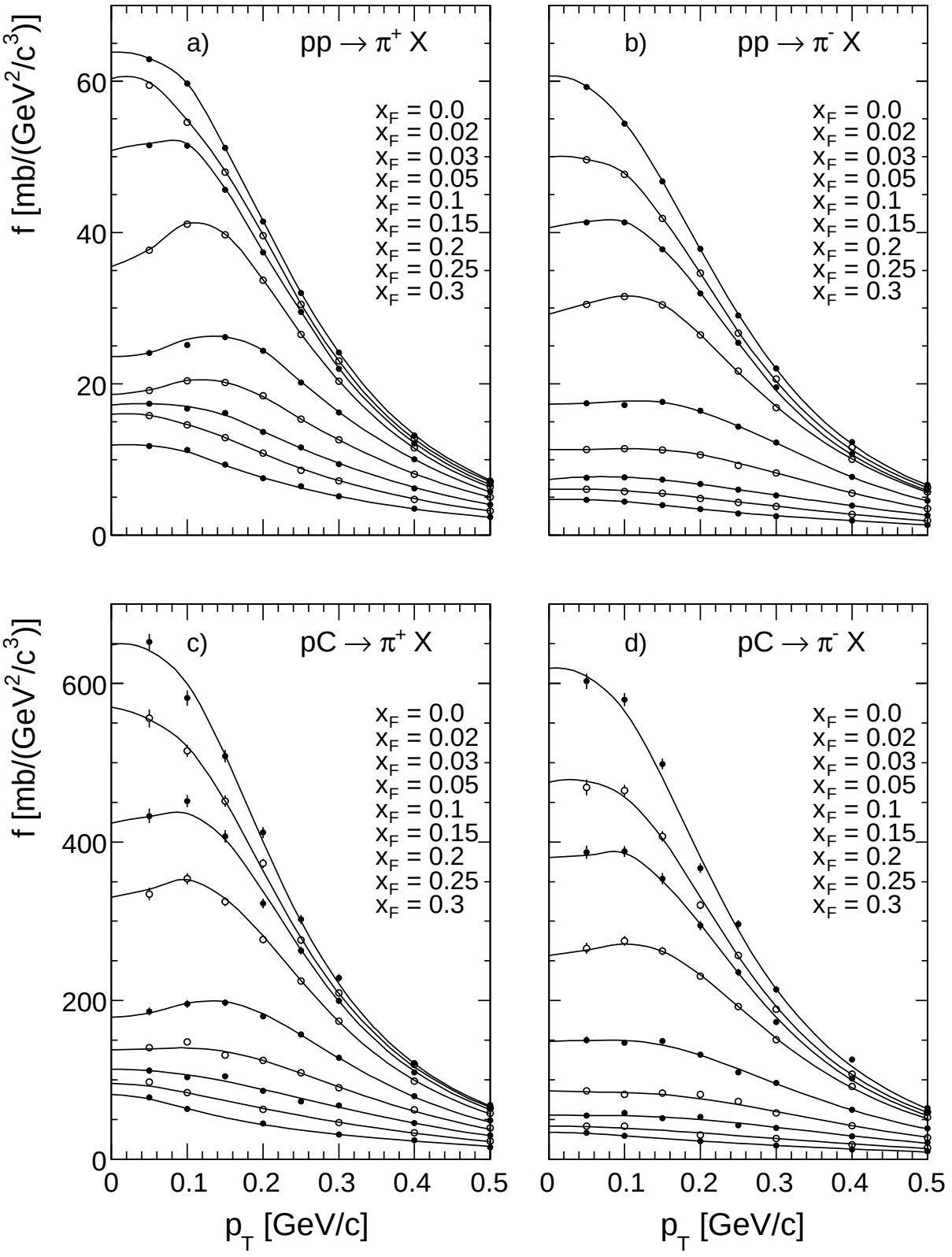

Figure 5.4: Invariant p_T distributions at low p_T region in linear scale at several fixed x_F values for a) π^+ in p+p, b) π^- in p+p, c) π^+ in p+C and d) π^- in p+C

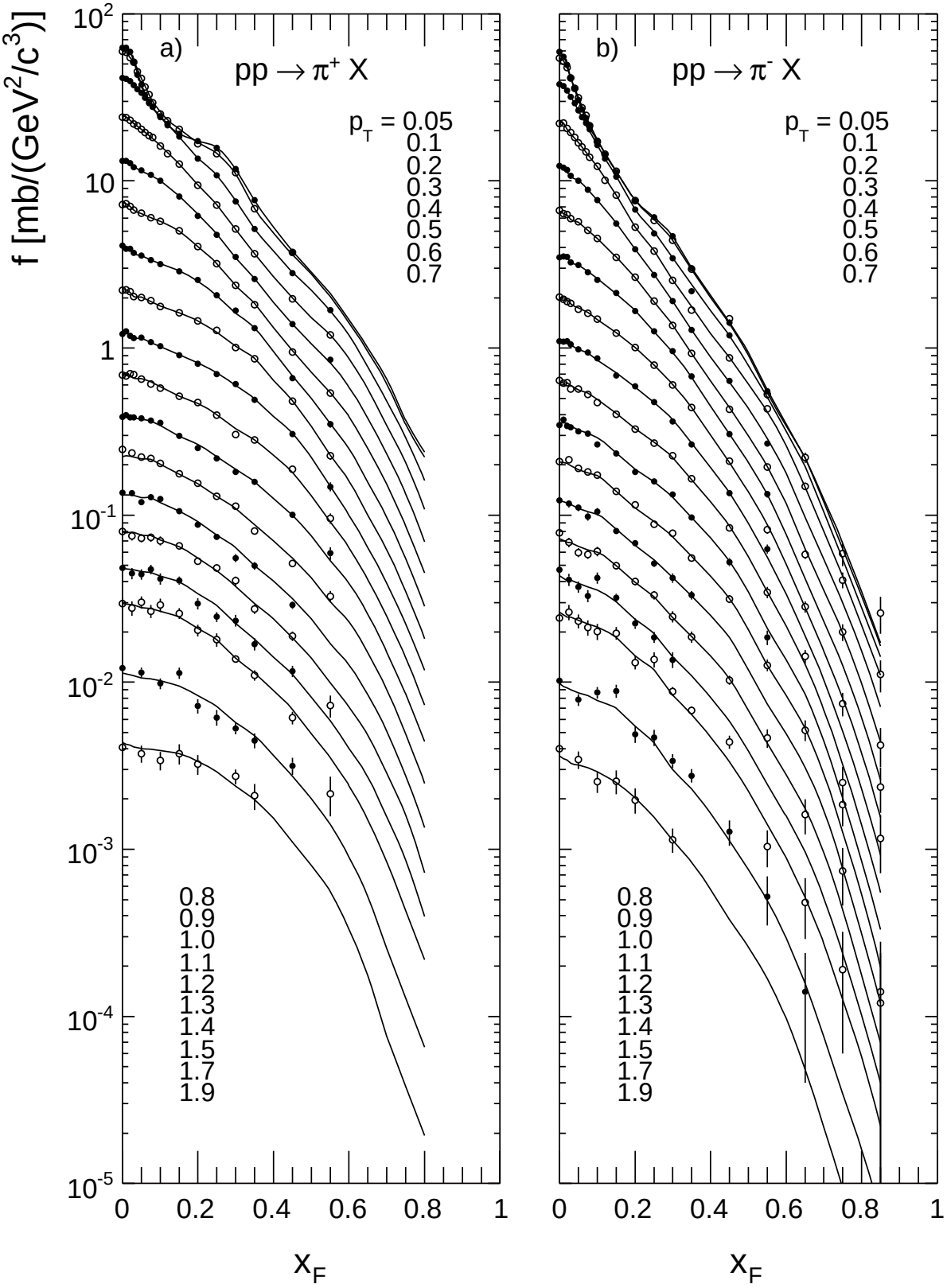

Figure 5.5: Invariant cross section in p+p at 158 GeV/c beam momentum as a function of x_F at several fixed p_T values for a) π^+ and b) π^-. The p_T values are given in GeV/c

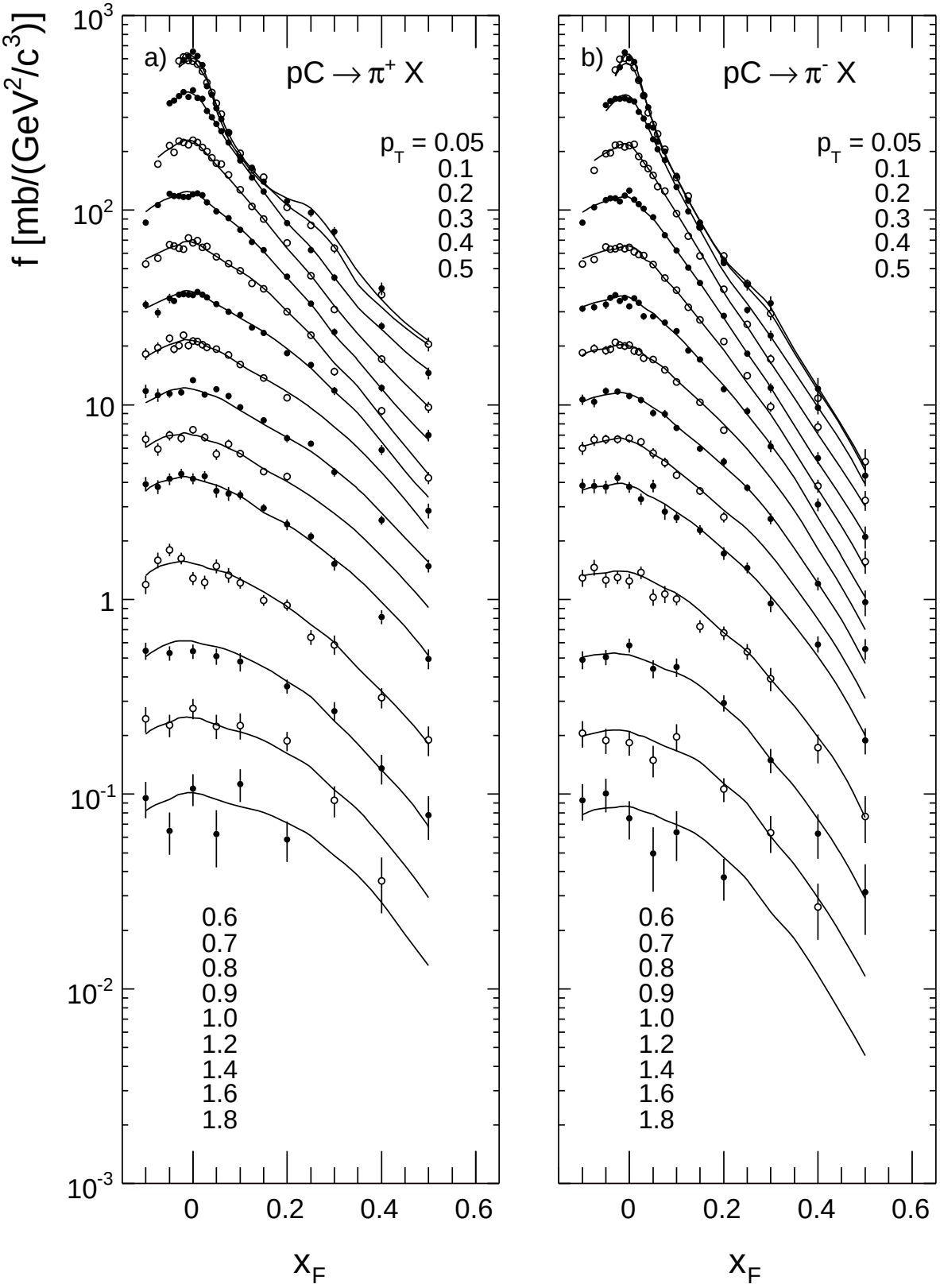

Figure 5.6: Invariant cross section in p+C at 158 GeV/c beam momentum as a function of x_F at several fixed p_T values for a) π^+ and b) π^-. The p_T values are given in GeV/c

5.3 π^+/π^- ratio

The observed differences in the invariant distributions of π^+ and π^- reflects in a complex behaviour of the corresponding π^+/π^- ratio. The p_T dependences for fixed x_F values are shown in Fig. 5.7 and 5.8 for p+p and p+C interactions, respectively.

In p+p case a very week p_T dependence is found at $x_F < 0.15$ where a local maximum is developed at low p_T which is connected to low-mass resonance decays. With increasing x_F the π^+/π^- ratio increases and in low p_T it reaches values above 3 at $x_F = 0.55$. Similar increase with x_F is seen in p+C collisions. The low p_T maxima are also present but much smaller. The other feature of π^+/π^- ratio in p+C interactions is that it tends to 1 at the negative x_F for all p_T values as it is expected from the isospin symmetry of the carbon nucleus.

The x_F distributions of π^+/π^- ratio for fixed p_T values are presented in Fig. 5.9 for p+p and in Fig. 5.10 for p+C collisions.

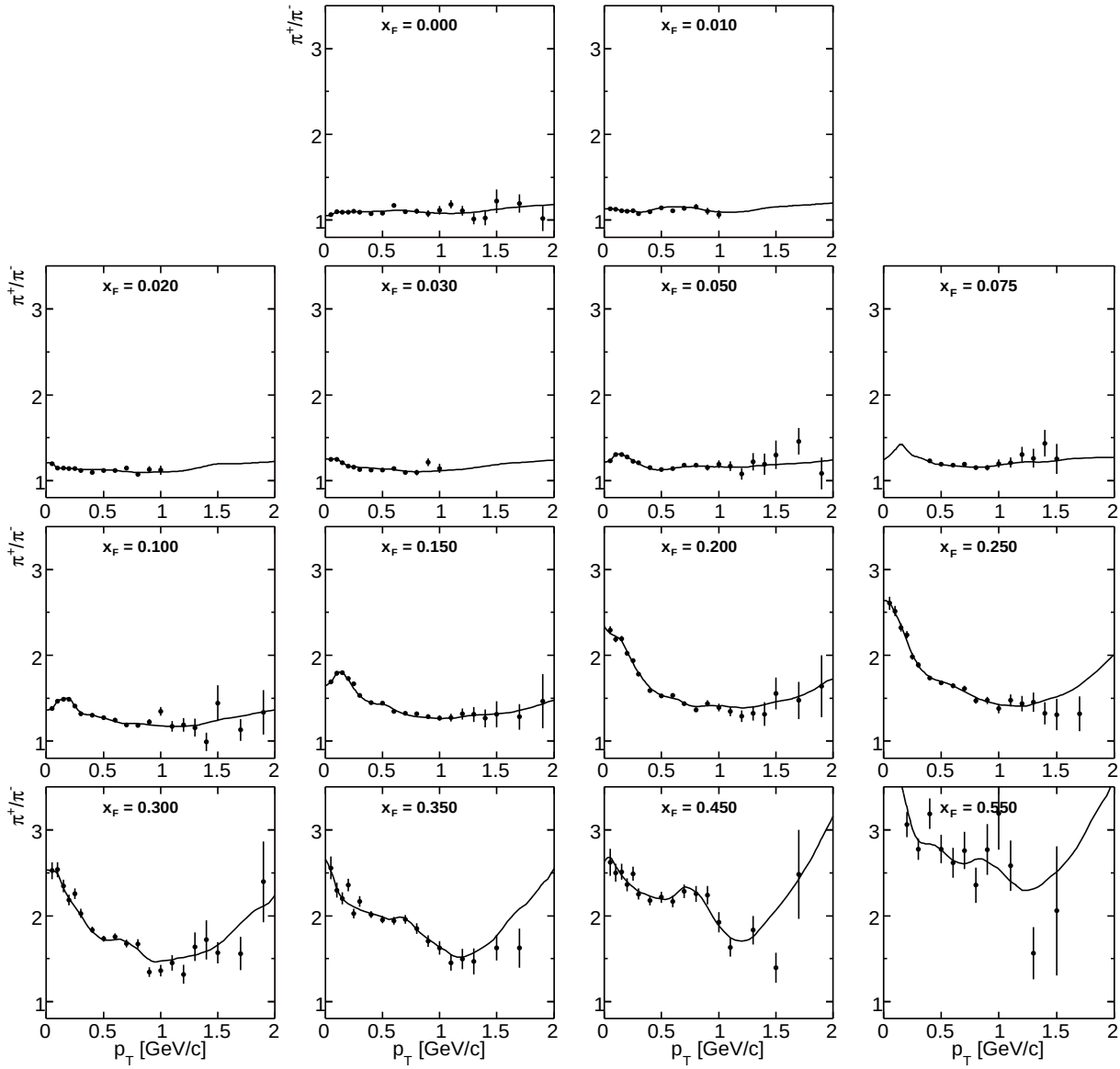

Figure 5.7: The π^+/π^- ratio in p+p as a function of p_T for fixed x_F

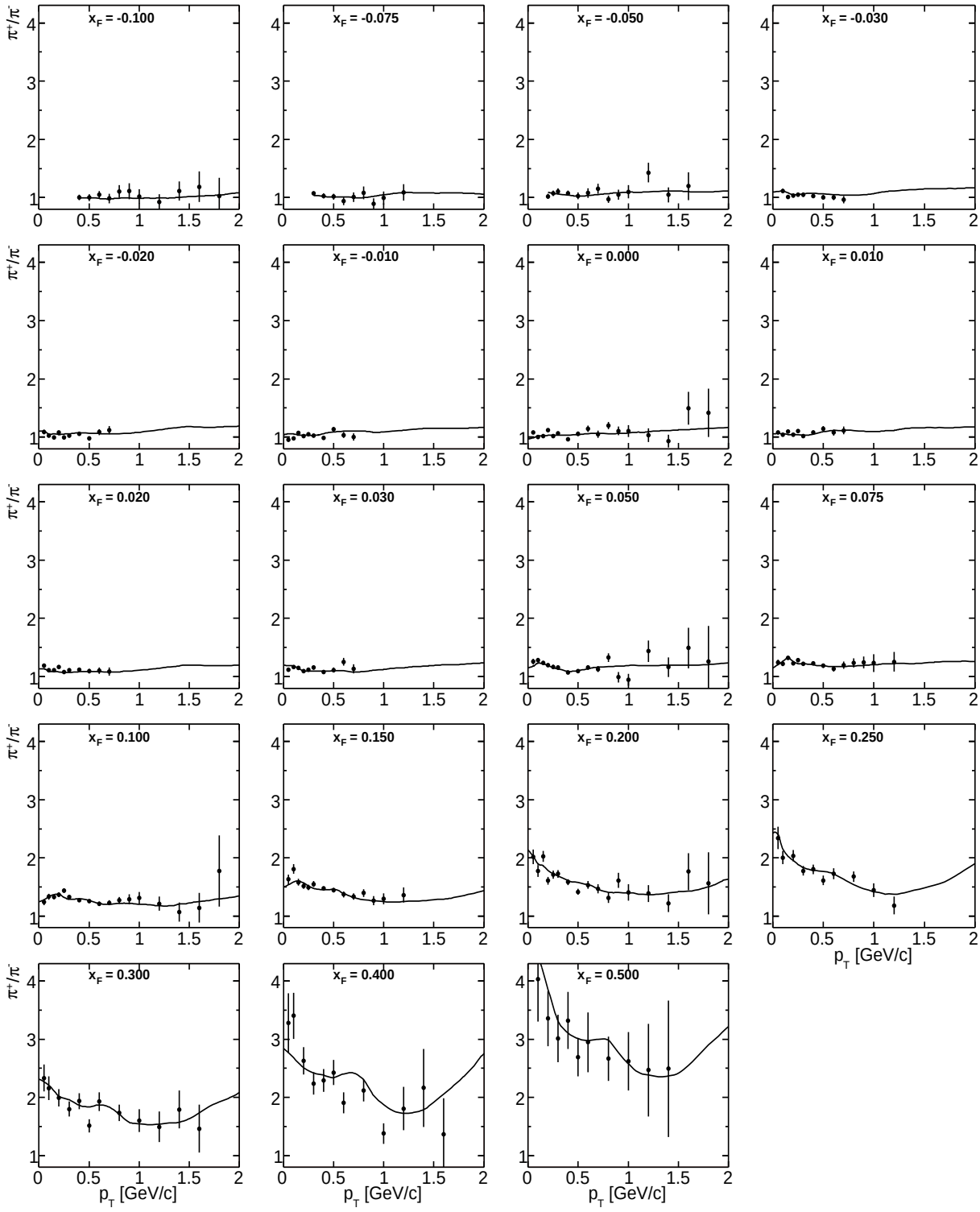

Figure 5.8: The π^+/π^- ratio in p+p as a function of p_T for fixed x_F

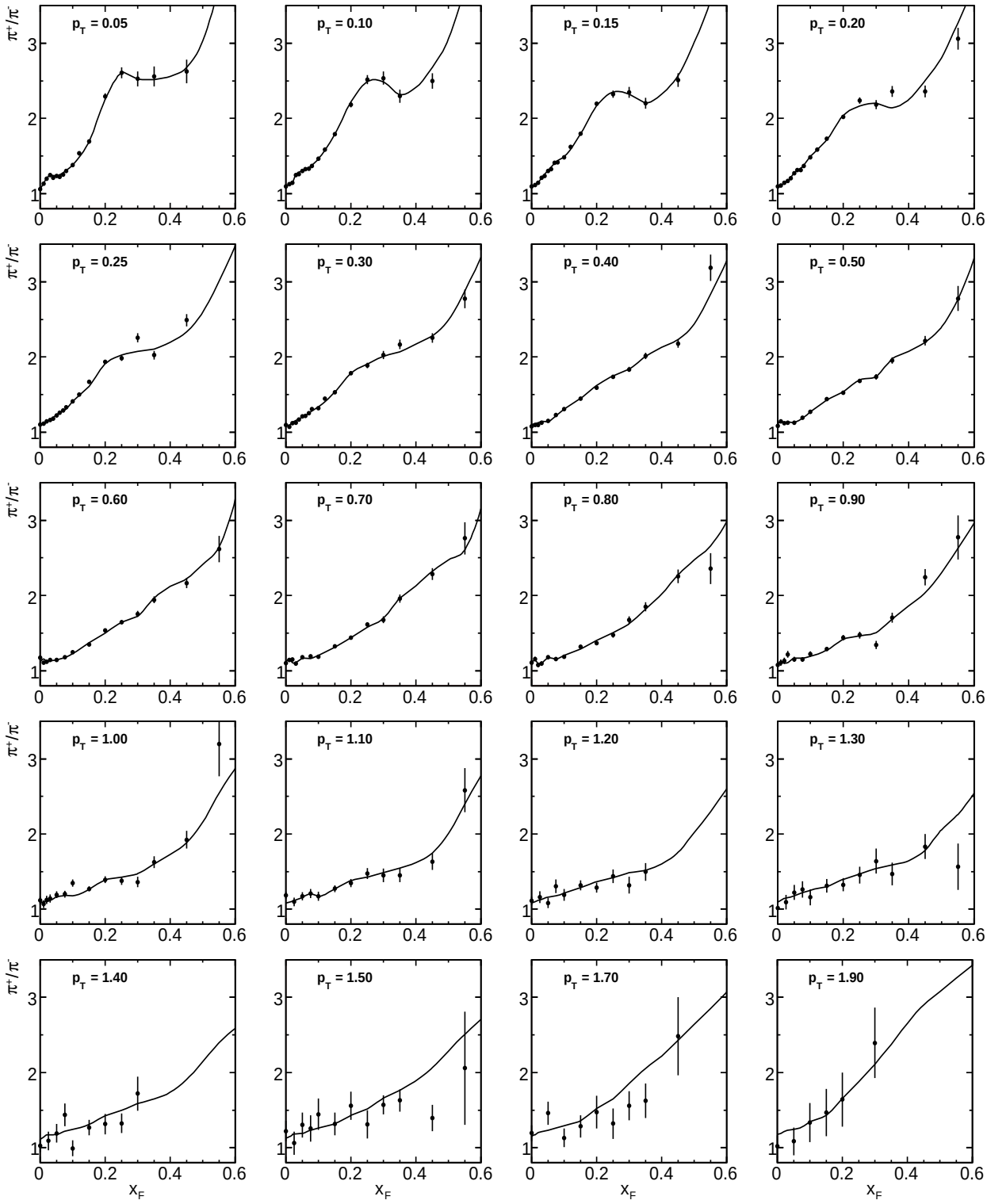

Figure 5.9: The π^+/π^- ratio in p+p as a function of x_F for fixed p_T. In all the plots p_T values are given in GeV/c

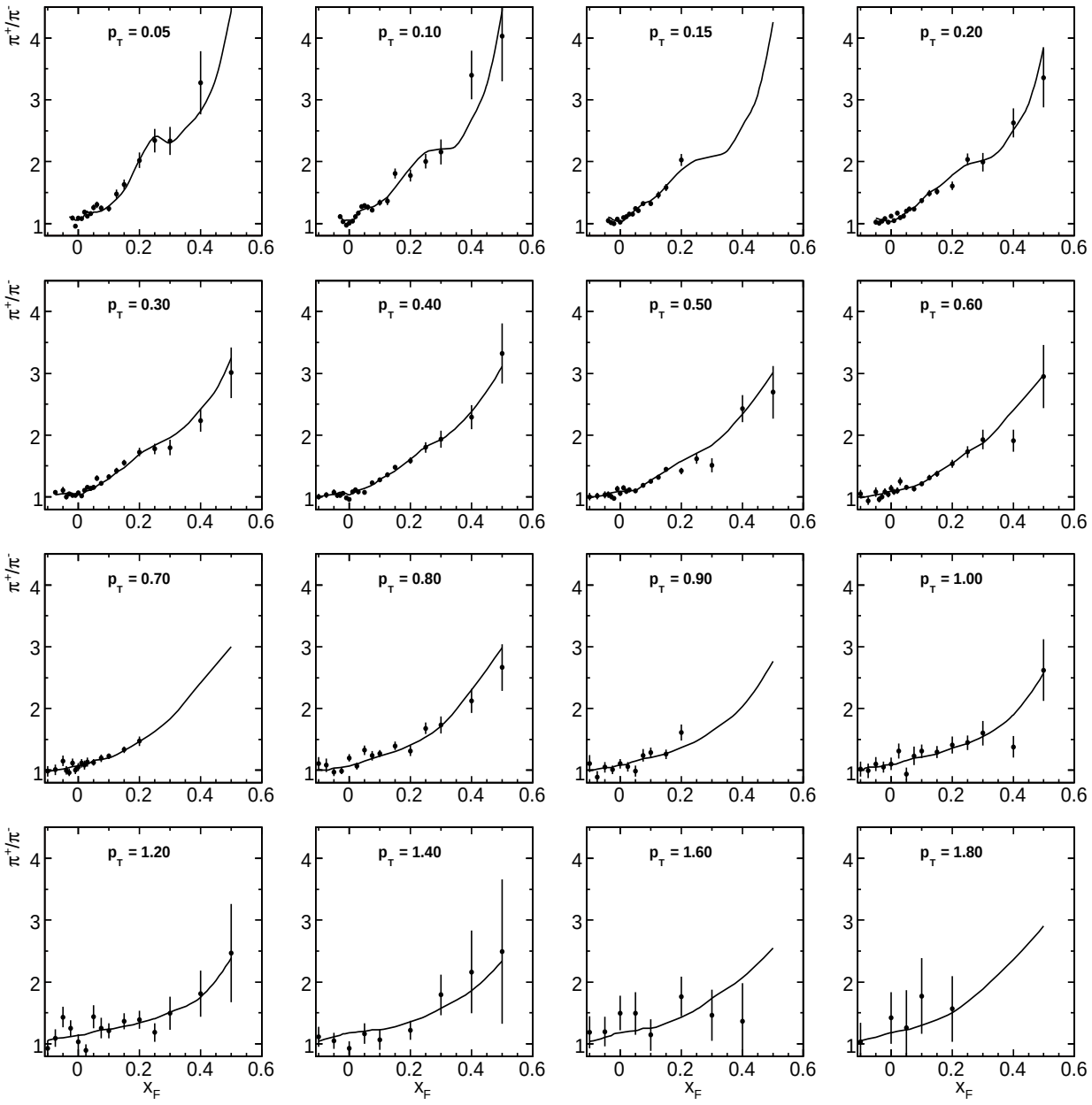

Figure 5.10: The π^+/π^- ratio in p+C as a function of x_F for fixed p_T. In all the plots p_T values are given in GeV/c

5.4 Rapidity and transverse mass distributions

It is customary to obtain the double differential invariant cross section also in the phase space of rapidity y and transverse momentum p_T although these two variables are not orthogonal in momentum space. The rapidity is defined as:

$$y = \frac{1}{2} \ln \frac{E + p_L}{E - p_L}, \tag{5.1}$$

where E and p_L are the energy and longitudinal momentum of the particle. The rapidity distributions at fixed p_T are presented in Fig. 5.11 (p+p) and Fig.5.12 (p+C). The structures observed in x_F distributions are also seen here.

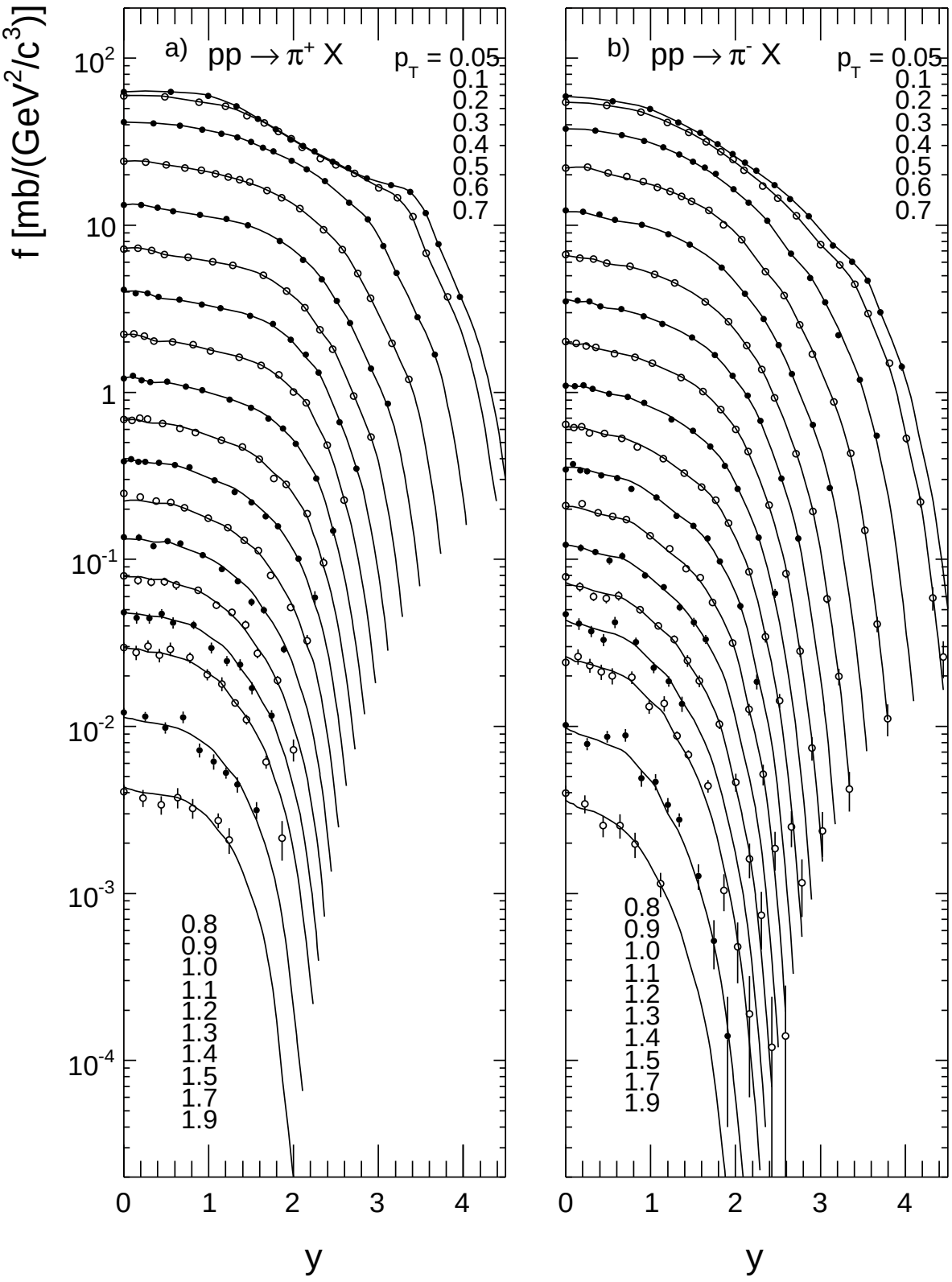

Figure 5.11: Invariant cross section in p+p at 158 GeV/c beam momentum as a function of y at several fixed p_T values for a) π^+ and b) π^-. The p_T values are given in GeV/c

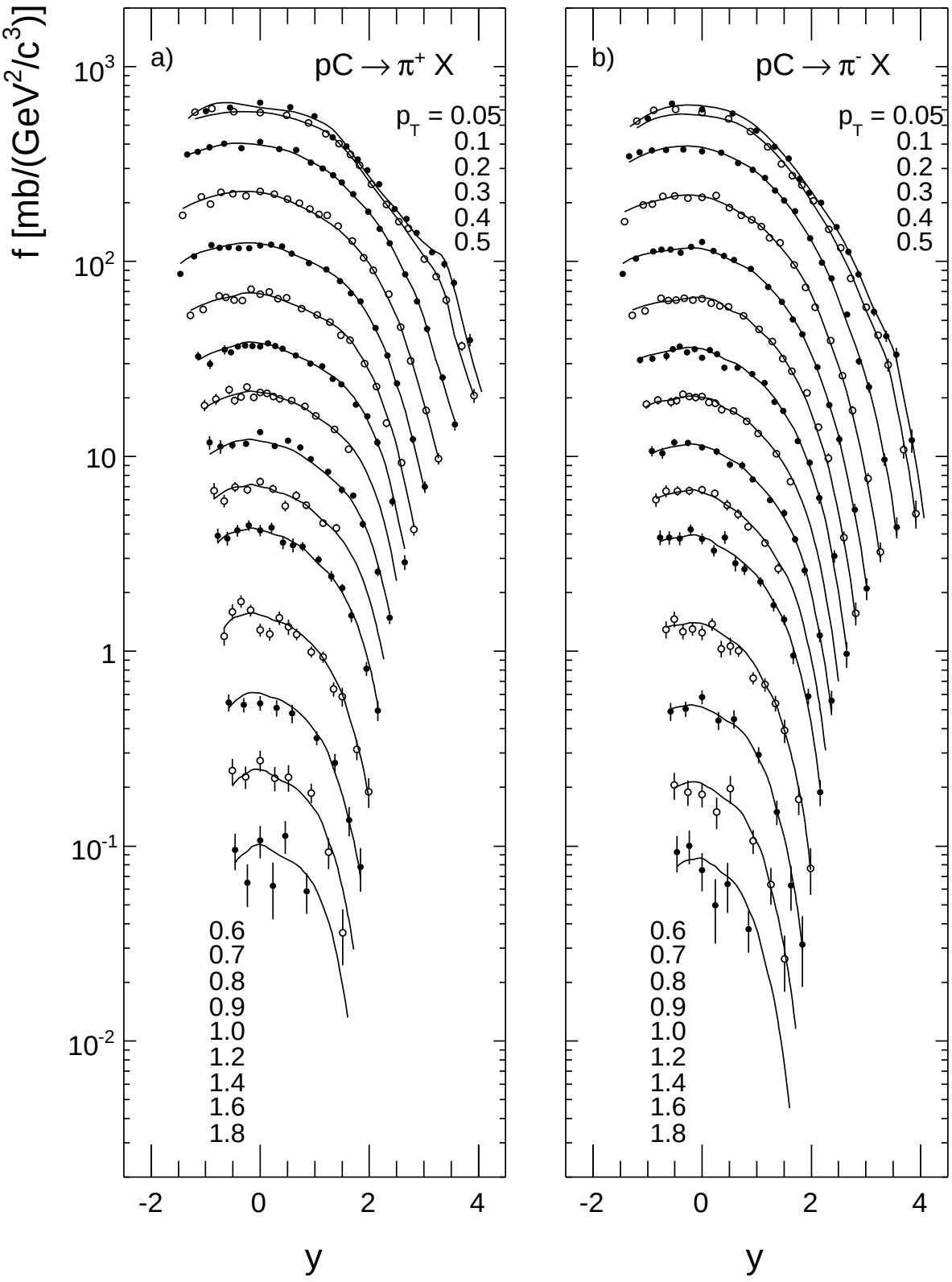

Figure 5.12: Invariant cross section in p+C at 158 GeV/c beam momentum as a function of y at several fixed p_T values for a) π^+ and b) π^-. The p_T values are given in GeV/c

Another frequently used variable is the transverse mass $m_T = \sqrt{p_T^2 + m_\pi^2}$. The $m_T - m_\pi$ distributions at $y = 0$ are shown in Figs. 5.13 in p+p and 5.14 in p+C collisions. It is often claimed that m_T distribution is close to exponential with the inverse slope parameter T as predicted for particle emission from a thermal source.

The high precision of the data allows to demonstrate that it is impossible to achieve a satisfactory approximation using single exponent with constant T. The distributions are

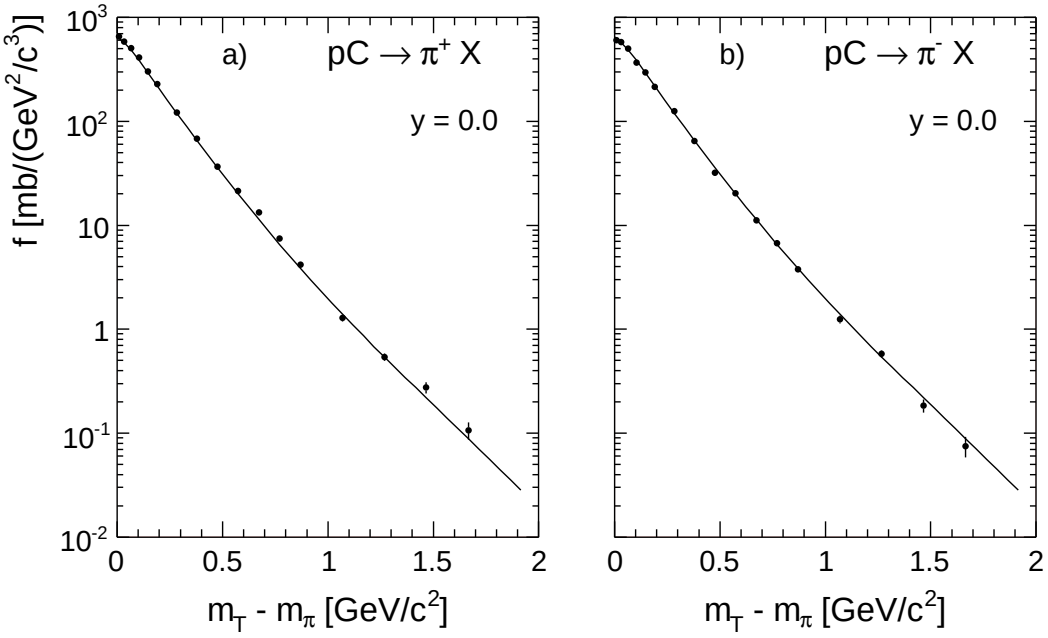

Figure 5.13: Invariant cross section in p+p as a function of $m_T - m_\pi$ for $y = 0.0$ at a) π^+ and b) π^-

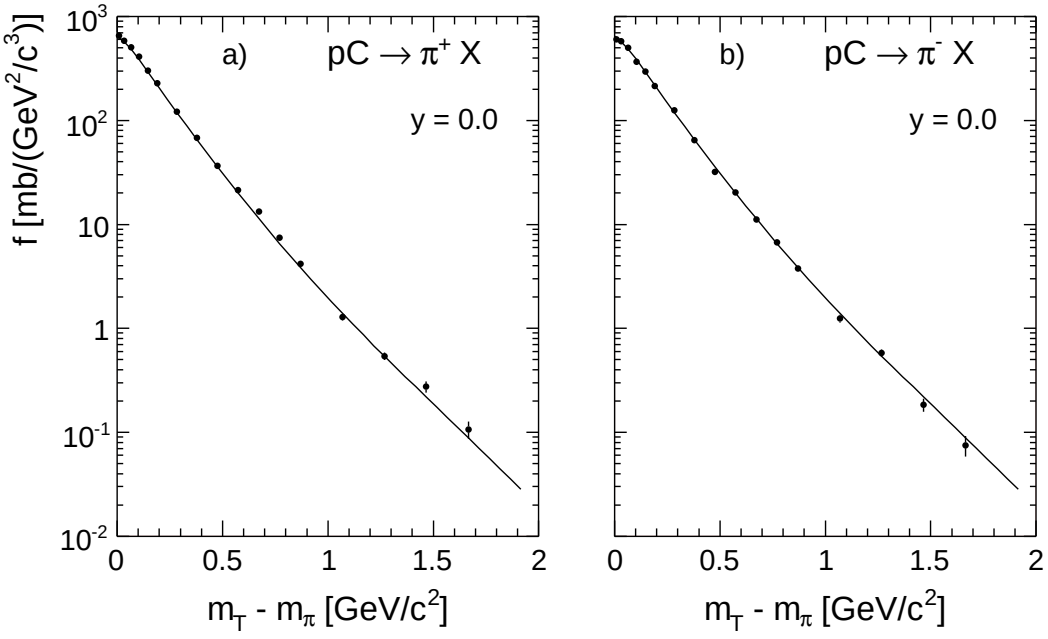

Figure 5.14: Invariant cross section in p+C as a function of $m_T - m_\pi$ for $y = 0.0$ at a) π^+ and b) π^-

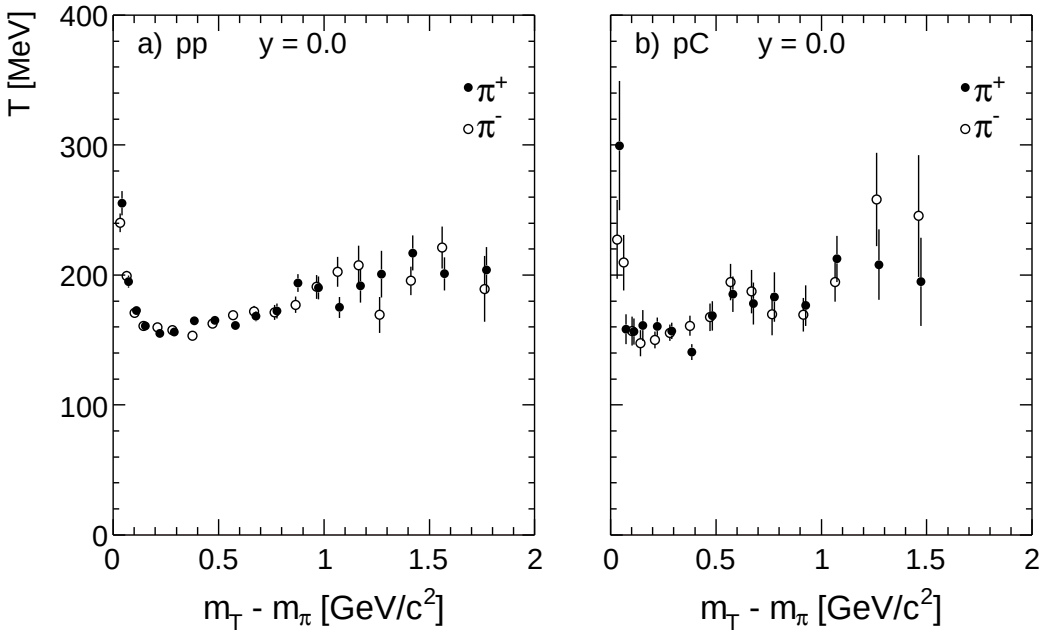

Figure 5.15: Local slope of the m_T distribution as a function of $m_T - m_\pi$ in a) p+p and in b) p+C interaction

described well when the inverse slope T is determined as a function of the transverse mass $(m_T - m_\pi)$. This dependence is presented in Fig. 5.15. In both reactions a smooth variation of T with $(m_T - m_\pi)$ is observed with local minimum around $(m_T - m_\pi) \backsimeq 250$ GeV/c^2. The variation in p+C reaction is more pronounced than in p+p one.

5.5 Comparison with other experiments

5.5.1 Comparison of π^+ and π^- invariant distribution

As was already mentioned in Sect.1.3, there are two preceding experiments which have measured pion invariant cross section in p+p for identified pions at NA49 energy range. The data from Brenner et al. [21] offer 107 data points measured at beam momenta of 100 and 175 GeV/c, the data from Johnson et al. [20] contain 241 data points at 100, 200 and 400 GeV/c beam momenta. The comparisons are presented in Fig. 5.16 and Fig. 5.17 where the interpolated NA49 data are shown as reference at those values of x_F and p_T where the direct comparison is feasible.

The NA49 measurements show a very good overall agreement with data from [21] while comparison with [20] reveals very sizable deviations with a complicated x_F and p_T dependence. This situation is quantified in the statistical analysis presented in Fig. 5.18.

In Fig. 5.18a,d the distributions of the point-by-point statistical error of the cross section difference are given. The errors have the most probable values around 6 and 4%, respectively. The long upwards tails are reflecting the decreasing of the cross section at high p_T and/or x_F. Fig. 5.18b,e show point-by-point cross section difference in percent with respect to NA49. In Fig. 5.18c,f are shown the cross section difference divided by the statistical error which should obey the Gaussian distribution with unity variance if it is governed by the statistical fluctuations only. This is indeed the case for data [21] demonstrated with the Gaussian fit in Fig. 5.18c. In fact the mean difference is less

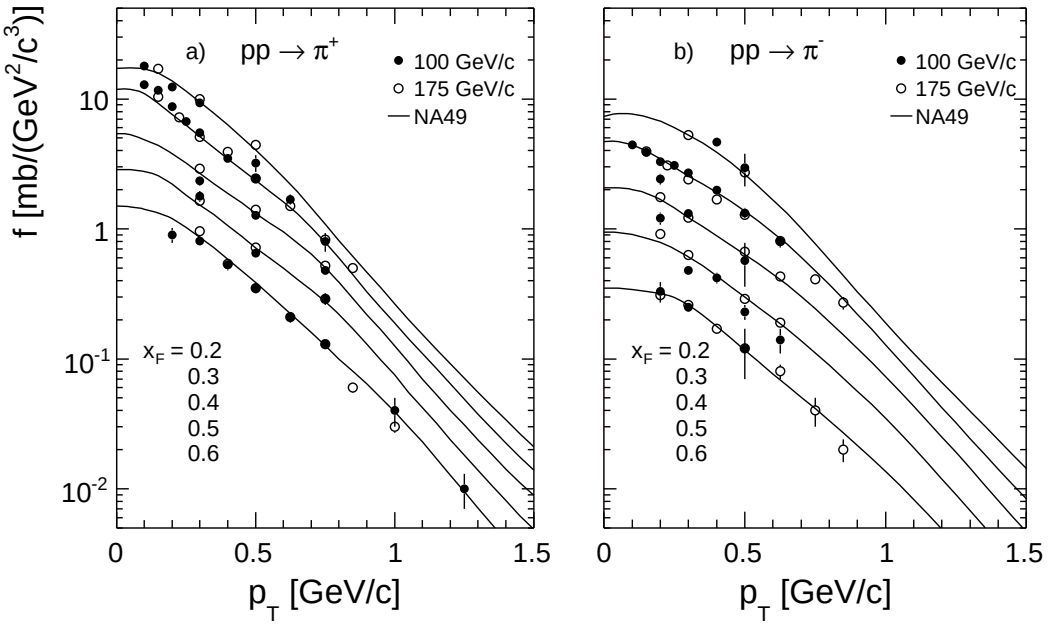

Figure 5.16: Comparison of the invariant cross section as a function of p_T at fixed x_F from NA49 (lines) with measurements from [21] at 100 and 175 GeV/c beam momentum for a) π^+ and b) π^-

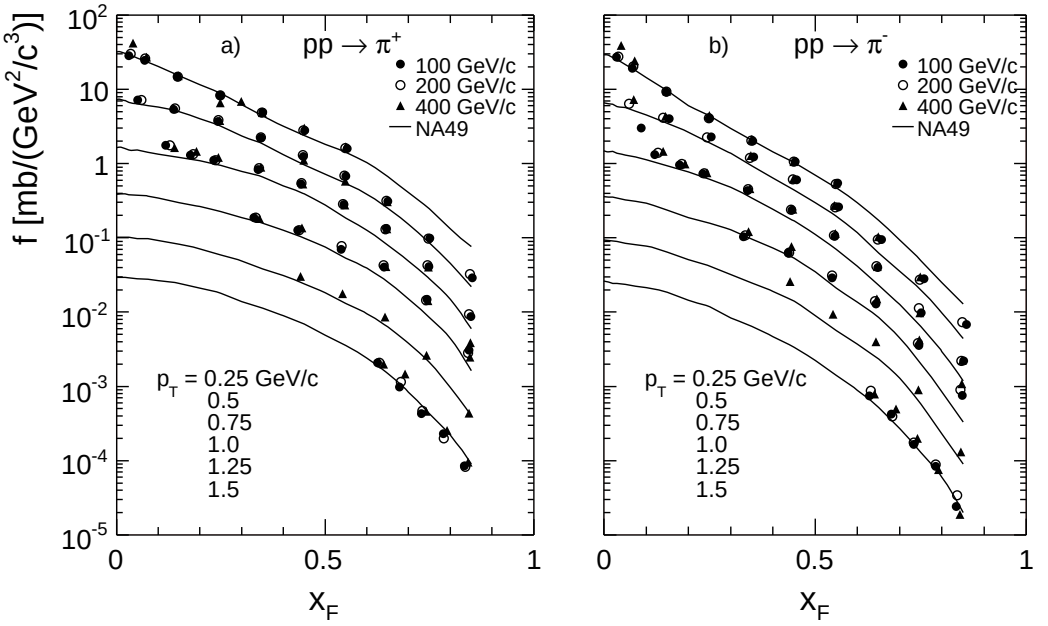

Figure 5.17: Comparison of the invariant cross section as a function of x_F at fixed p_T from NA49 (lines) with measurements from [20] at 100, 200 and 400 GeV/c beam momentum for a) π^+ and b) π^-

than 1% with an error of about 1% which is much less than the systematic errors of 2% (NA49) and 7% ([21]) quoted by the experiments. The agreement of the data within purely statistical fluctuations helps to exclude the systematic effects between the two measurements.

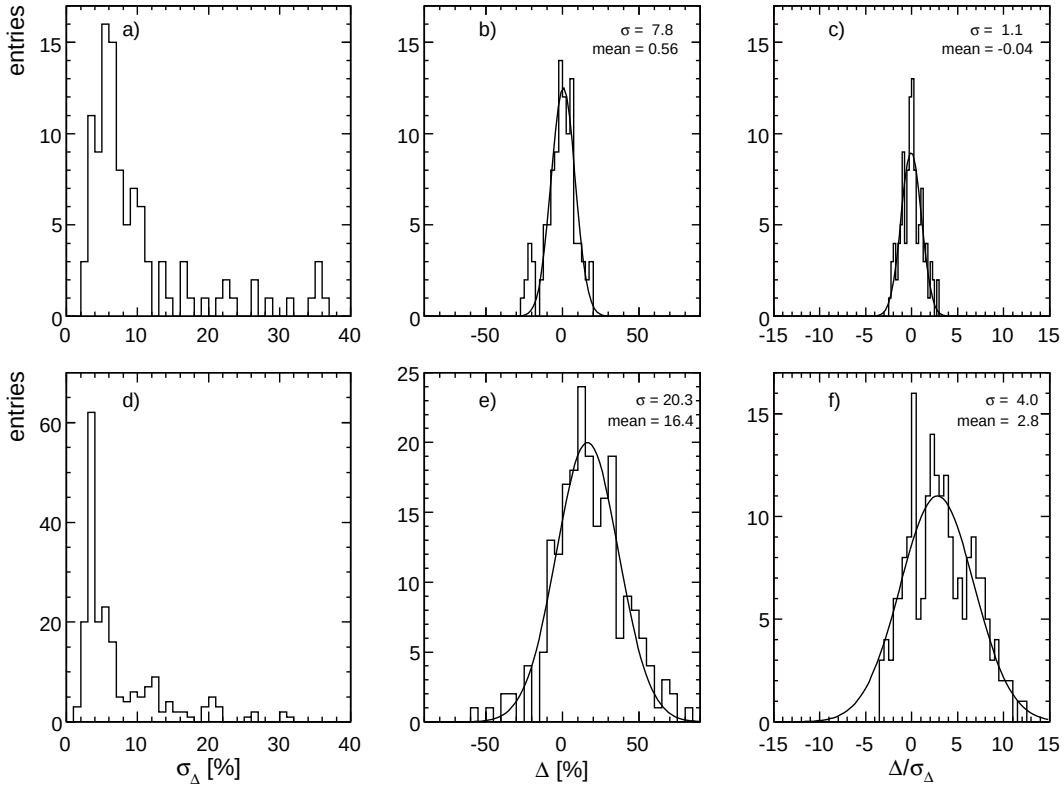

Figure 5.18: Statistical analysis of the difference of the measurements of [21] (upper three panels) and [20] (lower three panels) with respect to NA49: a) and d) error of the difference of the measurements; b) and e) difference of the measurements; c) and f) difference divided by the error

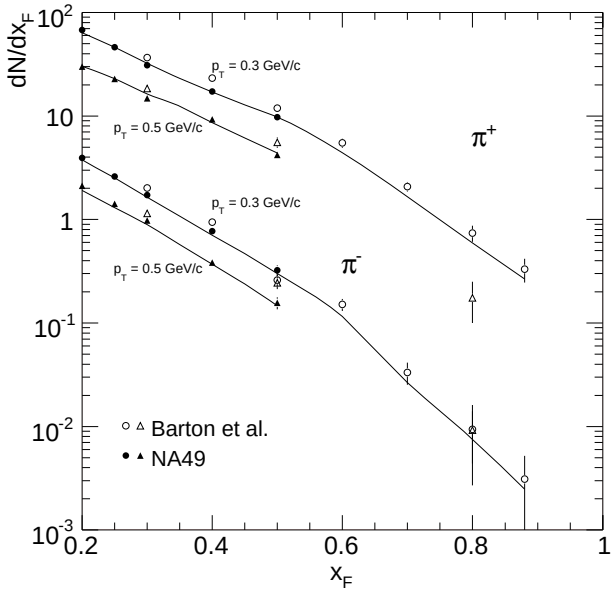

Figure 5.19: Comparison of the invariant cross section as a function of x_F at fixed p_T from NA49 (full symbols) with measurement from [35] (open symbols). The π^- data are multiplied by 0.1 to allow a separation from the π^+

The situation is less favourable with respect to the data [20]. Already in the direct data comparison, Fig. 5.17, large systematic deviations are clearly visible. The difference shown in Fig. 5.18e,f show very broad distributions as the normalized difference is off by nearly 3 standard deviation whilst the variance is around 4 units.

Concerning the p+C interactions, the only existing data set which can be directly compared to the NA49 results is that of Barton et al. [35]. The comparison is shown in Fig. 5.19.

For the 10 points which overlap with the NA49 data a clear upward deviation with an average of +25% or 3.6 standard deviations is evident. This deviation is somewhat hard to understand as these results come from a group which has published results on p+p interactions with the same apparatus [21] which show excellent agreement with NA49. Also the p+p reference data obtained in the framework of [35] are internally consistent, notwithstanding their sizable statistical errors, both with [21] and with NA49.

Nevertheless, it is possible, under the assumption that the large systematic difference has no dependence on p_T or x_F, to extend the interpolation of the NA49 data towards large x_F by imposing a 25% reduction on the Barton et al. data [35]. This extension is also indicated in Fig. 5.19 for $p_T = 0.3$ GeV/c.

5.5.2 Comparison of π^+/π^- ratio

A comparison of the π^+/π^- ratio in p+p collisions as a function of x_F between NA49 results and data from [21] and [20] is presented in Fig. 5.20 for several p_T values . In the upper four panels the π^+/π^- ratio measured by NA49 is compared with the ratio measurement of [21]. As expected from the comparison of invariant cross section the general agreement is satisfactory.

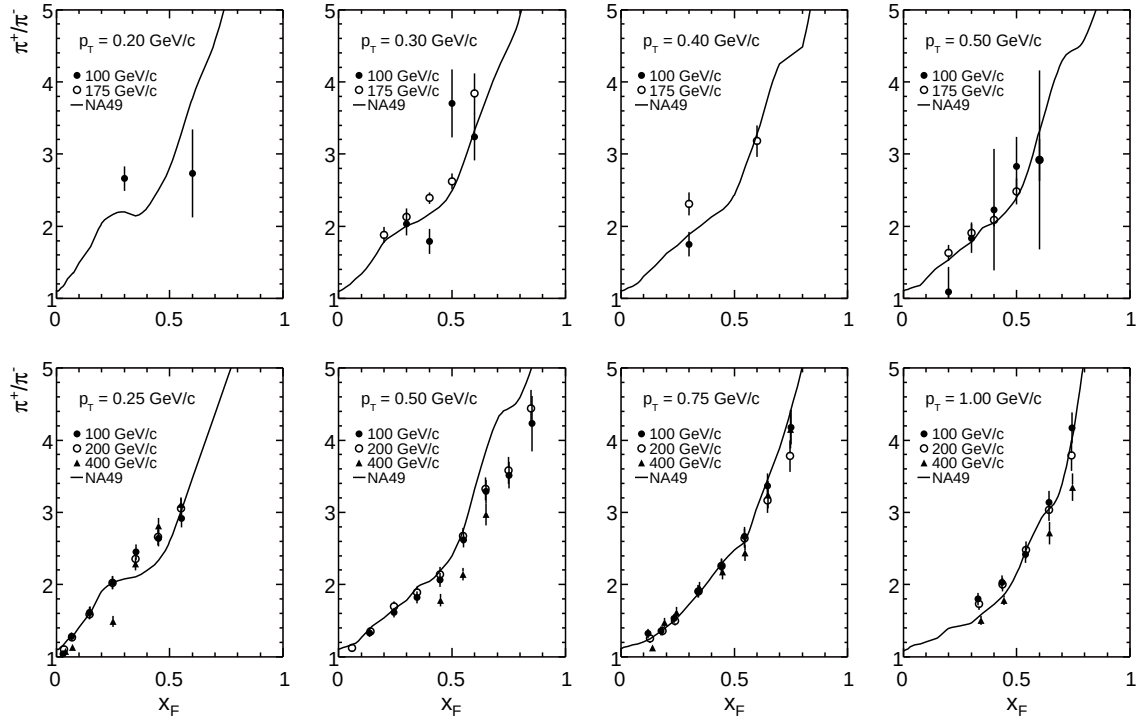

Figure 5.20: Comparison of the π^+/π^- ratio as a function of x_F at fixed p_T from NA49 (full symbols) with measurement from [21] (upper four panels) and [20] (lower four panels)

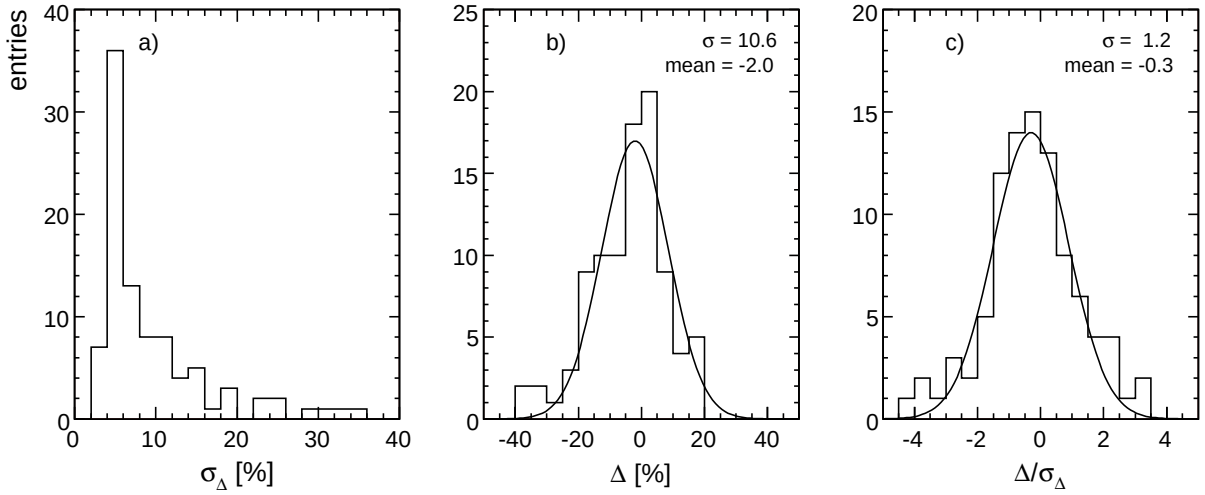

Figure 5.21: Statistical analysis of the difference of the of π^+/π^- ratio of [20] with respect to NA49: a) error of the difference of the ratio measurements; b) difference of the ratio measurements; c) difference divided by the error

It is however interesting to note that also data from [20] are in reasonable agreement with NA49 results as far as the ratios are concerned, which is clearly confirmed by the statistical analysis given in Fig. 5.21. This indicates that large systematic deviations observed in the cross sections cancel out in the ratios.

A similar situation is found in p+C data of Barton et al. [35] where the discrepancies in the cross sections cancel out and the π^+/π^- ratios are in very good agreement with the NA49 measurement. This is shown as a function of x_F in Fig. 5.22 at $p_T = 0.3$ GeV/c.

Since the Barton [35] data extend up to $x_F = 0.88$ at their measured transverse momenta, one can use the consistency of the π^+/π^- ratio to extend the NA49 data -

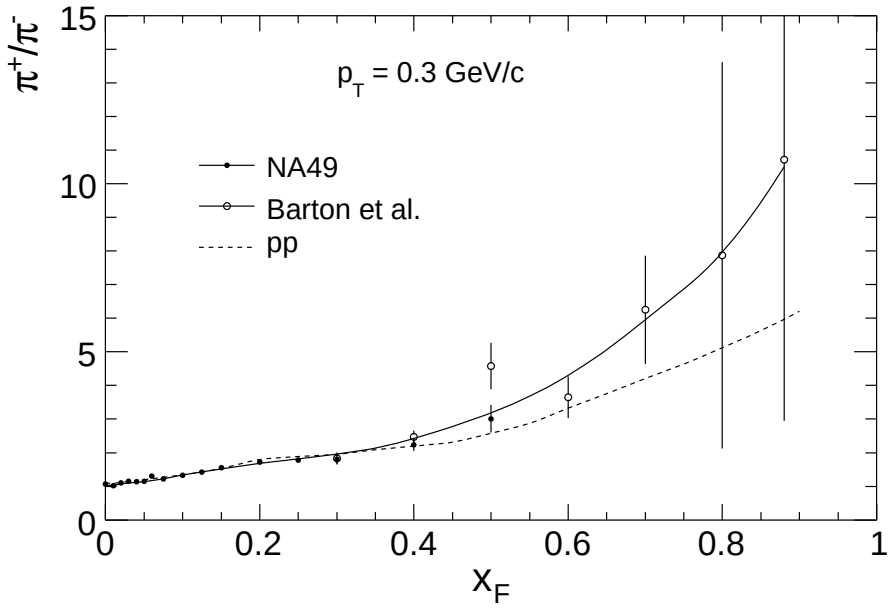

Figure 5.22: Comparison of π^+/π^- ratio as a function of x_F at fixed p_T from NA49 (full circles) with measurement from [35] (open circles). The dashed line represents the p+p data

albeit with large error bars - into the region of large x_F. This shows, a sizable increase of the charge ratio with respect to the p+p data also indicated in the Fig. 5.22.

5.5.3 Comparison of p+p data with Forward Production at ISR Energies and Extension of Data Interpolation for π^+

In the forward region for $x_F > 0.6$ the identification of the π^+ is difficult because of the dominant proton component. There are available large sets of ISR data [50–61] in the $\sqrt{s}$ range from 23 to 63 GeV. As the invariant cross section in the forward region is expected to be independent of the energy (Feynman scaling) the ISR measurements can be used to extend the NA49 results on π^+ to the same coverage as the π^- data. The π^+ cross sections have been published by CHLM Collaboration at $\sqrt{s} = 31$, 45 and 53 GeV [51], which cover the region $0.3 < x_F < 0.8$ and $0.2 < p_T < 2.5$ GeV/c, as well as the independent measurement at $\sqrt{s} = 45$ GeV [52] in the range $0.4 < x_F < 0.95$ and $0.35 < p_T < 1.45$ GeV/c. For π^- only measurements at $\sqrt{s} = 45$ GeV [52] and a set of data at one fixed angle [50] at $\sqrt{s} = 23$, 31, 45, 53 and 63 GeV are available.

The direct comparison of the ISR and NA49 data for π^- in the overlapping region is presented in Fig 5.23 showing the x_F distributions at fixed p_T. There is a very good agreement over the complete range of measurements from [52] (Fig 5.23a) which is confirmed by the statistical analysis in Fig. 5.24. The data from [50] are also in agreement with NA49 results (Fig 5.23b) with the exception of the their lowest energy at $\sqrt{s} = 23$ GeV which is above the NA49 data by about 25%.

The data for π^+ are summarized in Fig. 5.25. The ISR data of [51] obtained at $\sqrt{s} = 31$, 45, 53 GeV show good agreement (Fig. 5.25a) while the data of [52] from the same

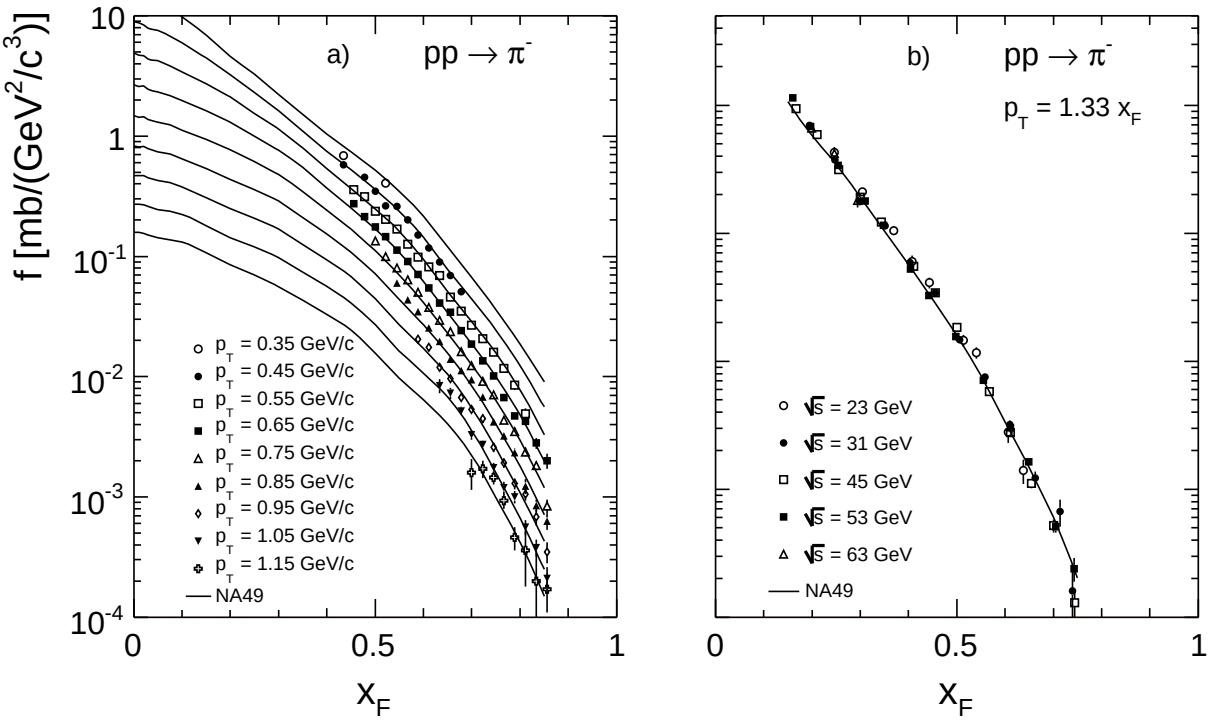

Figure 5.23: Comparison of invariant cross section as a function of x_F at fixed p_T measured by NA49 (lines) with measurements at a) $\sqrt{s} = 45$ GeV [52] and b) $\sqrt{s} = 23$, 31, 45, 53, 63 GeV [50]

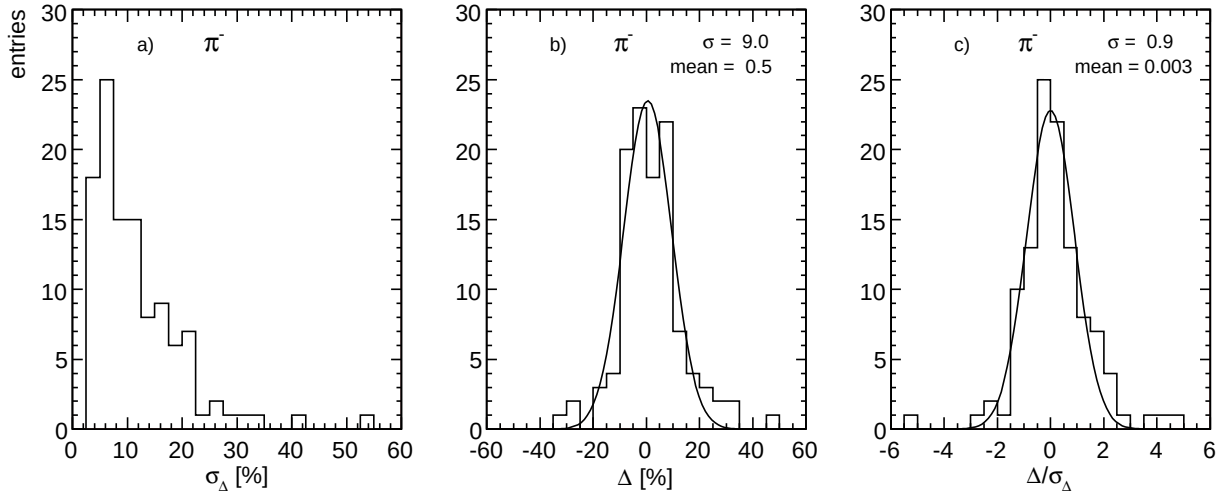

Figure 5.24: Statistical analysis of the difference of the measurements of [52] with respect to NA49: a) error of the difference of the measurements; b) difference of the measurements; c) difference divided by the error

collaboration show sizable upward shifts of about 20% in the x_F region where they overlap with the NA49 measurements (Fig. 5.25b). On the other hand this internal discrepancy vanishes at higher x_F values. Therefore the combined data of [51] and [52] have been used in order to extend the data parametrization of NA49 for π^+. The agreement with data

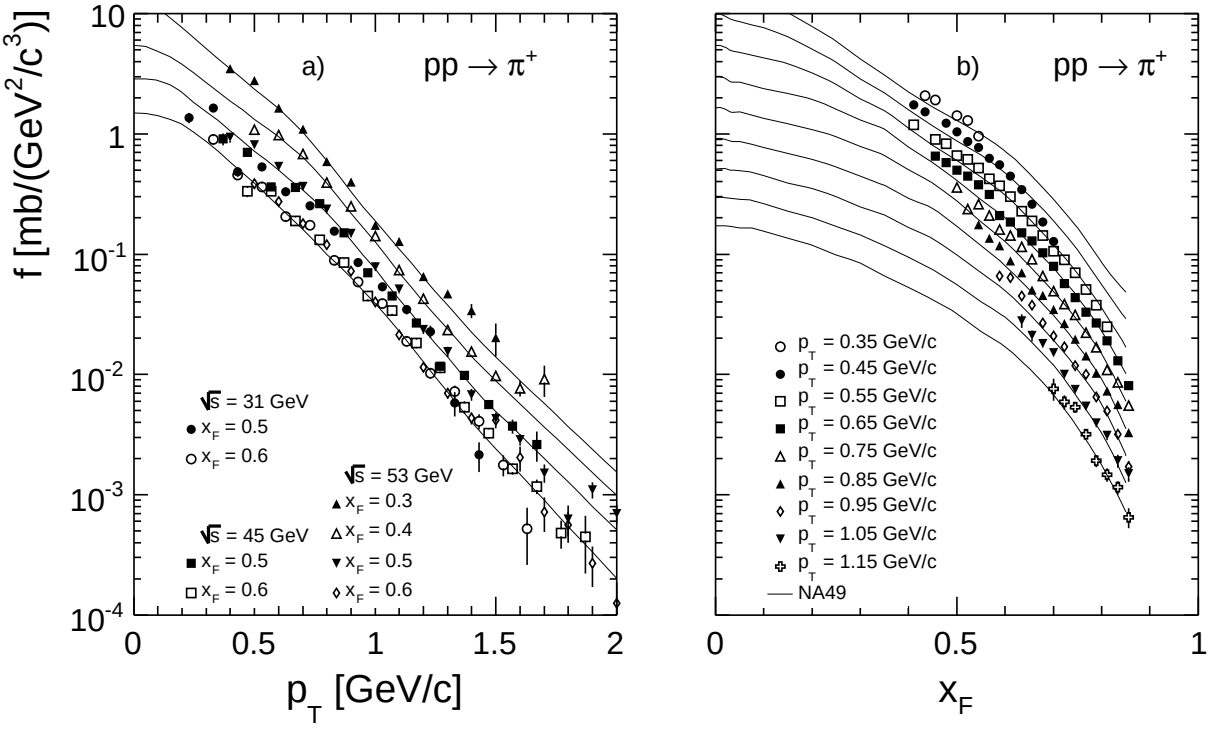

Figure 5.25: Comparison of invariant cross section as a function of a) p_T at fixed x_F published by [51] at $\sqrt{s}$ = 31, 45, 53 GeV and b) x_F at fixed p_T published by [52] at $\sqrt{s}$ = 45 GeV to NA49 measurements represented as lines

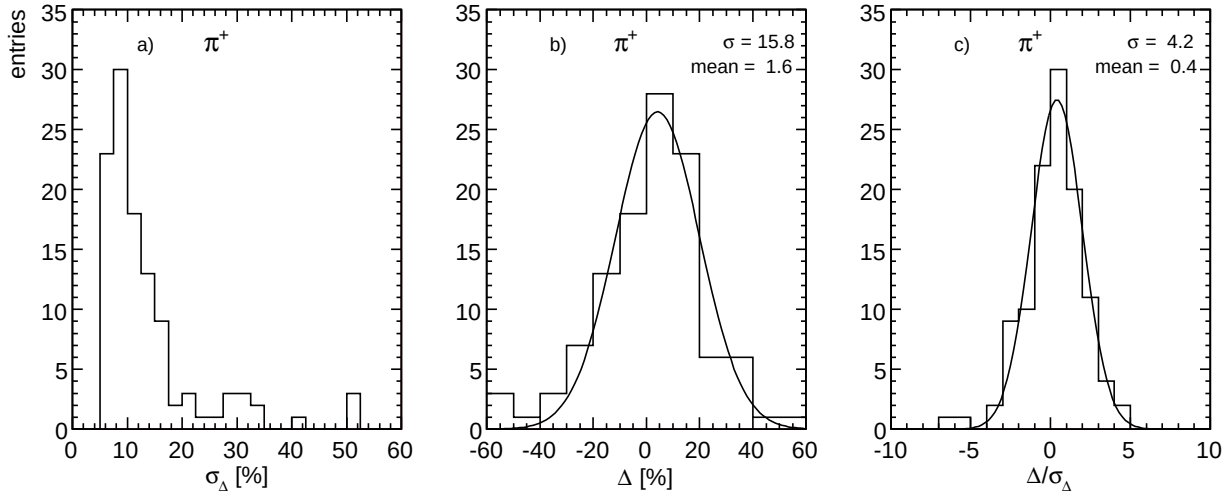

Figure 5.26: Statistical analysis of the difference of the measurements of [51] with respect to NA49: a) error of the difference of the measurements; b) difference of the measurements; c) difference divided by the error

of [51] is confirmed by the statistical analysis presented in Fig. 5.26.

The comparison of the data over the range of $\sqrt{s}$ from 17 to 63 GeV demonstrates Feynman scaling to the level of a few percent both for π^+ and π^- at $x_F > 0.4$.

Chapter 6

Integrated Distribution

6.1 p_T Integrated Distributions

The p_T integrated invariant and non-invariant yields are defined as:

$$\begin{aligned} dn/dx_F &= \pi/\sigma_{\text{inel}} \cdot \sqrt{s}/2 \cdot \int f/E \cdot dp_T^2 \\ F &= \int f \cdot dp_T^2 \\ dn/dy &= \pi/\sigma_{\text{inel}} \cdot \int f \cdot dp_T^2 \end{aligned} \tag{6.1}$$

where $f = E \cdot d^3\sigma/dp^3$ is the invariant cross section. The resulting integrated quantities are summarized in Tables 6.1 for p+p and 6.2 for p+C as a function of x_F and in Table 6.3 for both reactions as a function of y. The distributions are presented in Fig. 6.1 (p+p) and in Fig. 6.2 (p+C).

	π^+								π^-							
x_F	F	Δ	dn/dx_F	Δ	$\langle p_T \rangle$	Δ	$\langle p_T^2 \rangle$	Δ	F	Δ	dn/dx_F	Δ	$\langle p_T \rangle$	Δ	$\langle p_T^2 \rangle$	Δ
0.0	7.505	0.13	20.959	0.14	0.2590	0.06	0.1015	0.13	6.832	0.13	19.136	0.13	0.2579	0.06	0.1009	0.13
0.01	7.500	0.12	19.640	0.13	0.2664	0.06	0.1062	0.13	6.704	0.12	17.586	0.13	0.2659	0.06	0.1055	0.13
0.02	7.171	0.12	16.348	0.12	0.2811	0.06	0.1165	0.12	6.323	0.12	14.334	0.13	0.2838	0.06	0.1183	0.13
0.03	6.819	0.12	13.344	0.12	0.2962	0.06	0.1274	0.12	5.865	0.12	11.377	0.13	0.3018	0.06	0.1312	0.13
0.05	6.216	0.12	9.134	0.12	0.3276	0.06	0.1520	0.12	5.180	0.12	7.550	0.13	0.3357	0.06	0.1579	0.13
0.075	5.519	0.12	6.084	0.12	0.3571	0.06	0.1776	0.14	4.391	0.13	4.807	0.14	0.3683	0.06	0.1868	0.15
0.1	4.963	0.12	4.353	0.12	0.3763	0.07	0.1955	0.14	3.734	0.14	3.254	0.14	0.3912	0.07	0.2093	0.18
0.15	4.050	0.11	2.502	0.12	0.4010	0.07	0.2214	0.15	2.707	0.14	1.663	0.14	0.4240	0.07	0.2435	0.14
0.2	3.263	0.14	1.549	0.14	0.4170	0.08	0.2408	0.15	1.925	0.17	0.9091	0.17	0.4509	0.09	0.2728	0.17
0.25	2.619	0.20	1.007	0.20	0.4246	0.09	0.2520	0.19	1.437	0.24	0.5505	0.24	0.4625	0.12	0.2890	0.23
0.3	1.959	0.26	0.6325	0.26	0.4395	0.13	0.2697	0.24	1.042	0.35	0.3355	0.35	0.4750	0.17	0.3046	0.31
0.35	1.462	0.27	0.4061	0.27	0.4634	0.13	0.2932	0.23	0.7280	0.37	0.2020	0.37	0.4857	0.18	0.3184	0.31
0.45	0.8027	0.29	0.1745	0.29	0.4768	0.14	0.3112	0.24	0.3552	0.45	0.0772	0.45	0.4940	0.19	0.3312	0.33
0.55	0.4439	0.65	0.0792	0.65	0.4631	0.25	0.2964	0.50	0.1544	0.78	0.0275	0.78	0.4896	0.40	0.3232	0.74
0.65	0.2046	1.00	0.0309	1.05	0.4587	0.60	0.2915	1.15	0.0542	1.46	0.00820	1.46	0.4865	0.82	0.3269	1.58
0.75	0.0727	2.05	0.00955	2.10	0.4501	1.00	0.2804	1.75	0.0157	2.96	0.00205	2.96	0.4741	1.64	0.3068	3.05
0.85	0.0200	3.25	0.00232	3.35	0.4040	2.60	0.2314	3.50	0.00355	5.93	0.00041	5.93	0.4345	3.44	0.2602	6.25

Table 6.1: p_T integrated invariant cross section F [mb·c], density distribution dn/dx_F, mean transverse momentum $\langle p_T \rangle$ [GeV/c], mean transverse momentum squared $\langle p_T^2 \rangle$ [(GeV/c)^2] as a function of x_F for π^+ and π^- in p+p collisions at 158 GeV/c beam momentum. The statistical uncertainty Δ for each quantity is given in %

	π^+								π^-							
x_F	F	Δ	dn/dx_F	Δ	$\langle p_T \rangle$	Δ	$\langle p_T^2 \rangle$	Δ	F	Δ	dn/dx_F	Δ	$\langle p_T \rangle$	Δ	$\langle p_T^2 \rangle$	Δ
-0.05	64.312	0.57	13.211	0.57	0.3267	0.40	0.1533	0.80	60.470	0.57	12.401	0.57	0.3287	0.40	0.1543	0.80
-0.04	66.736	0.52	15.726	0.52	0.3114	0.31	0.1411	0.60	62.771	0.52	14.749	0.52	0.3141	0.31	0.1425	0.60
-0.03	69.546	0.48	19.030	0.48	0.2954	0.30	0.1287	0.55	65.076	0.48	17.768	0.48	0.2970	0.31	0.1294	0.55
-0.02	72.264	0.38	23.052	0.38	0.2801	0.28	0.1177	0.52	68.061	0.38	21.743	0.38	0.2796	0.30	0.1168	0.55
-0.01	73.693	0.34	26.993	0.34	0.2658	0.27	0.1077	0.50	69.751	0.33	25.747	0.33	0.2631	0.30	0.1049	0.54
0.0	71.923	0.32	28.088	0.32	0.2586	0.27	0.1030	0.48	69.484	0.30	27.364	0.30	0.2558	0.30	0.1008	0.54
0.01	70.586	0.32	25.756	0.32	0.2672	0.27	0.1088	0.50	66.470	0.31	24.424	0.31	0.2648	0.30	0.1062	0.55
0.02	66.086	0.32	20.903	0.32	0.2840	0.27	0.1210	0.50	60.877	0.32	19.247	0.32	0.2844	0.30	0.1206	0.55
0.03	61.594	0.33	16.683	0.33	0.3012	0.29	0.1339	0.55	55.378	0.35	14.938	0.35	0.3042	0.31	0.1352	0.58
0.04	57.541	0.35	13.389	0.35	0.3205	0.30	0.1491	0.60	50.685	0.37	11.757	0.37	0.3237	0.32	0.1506	0.62
0.05	54.137	0.35	10.981	0.35	0.3379	0.32	0.1637	0.62	47.027	0.38	9.516	0.38	0.3413	0.32	0.1649	0.62
0.075	46.426	0.35	7.067	0.35	0.3734	0.32	0.1957	0.62	38.142	0.38	5.790	0.38	0.3781	0.32	0.1993	0.62
0.1	40.396	0.35	4.904	0.35	0.3960	0.30	0.2182	0.58	31.456	0.38	3.803	0.38	0.4045	0.32	0.2268	0.62
0.125	35.101	0.37	3.531	0.37	0.4144	0.32	0.2375	0.65	25.590	0.42	2.561	0.42	0.4277	0.33	0.2525	0.65
0.15	30.875	0.38	2.648	0.38	0.4267	0.32	0.2520	0.65	21.385	0.47	1.826	0.47	0.4436	0.34	0.2708	0.70
0.2	23.488	0.50	1.5499	0.50	0.4489	0.37	0.2797	0.70	14.535	0.62	0.9555	0.62	0.4730	0.37	0.3053	0.70
0.25	18.174	0.65	0.9734	0.65	0.4607	0.41	0.2967	0.80	10.258	0.87	0.5475	0.87	0.4909	0.43	0.3308	0.85
0.3	13.327	0.87	0.5996	0.87	0.4755	0.44	0.3154	0.90	7.105	1.15	0.3190	1.15	0.4993	0.53	0.3425	1.10
0.4	7.207	1.15	0.2455	1.15	0.4912	0.61	0.3344	1.10	3.060	1.60	0.1041	1.60	0.5159	0.63	0.3664	1.15
0.5	3.943	1.60	0.1081	1.60	0.4714	0.90	0.3157	1.60	1.226	2.40	0.0336	2.40	0.5125	1.00	0.3620	2.00

Table 6.2: p_T integrated invariant cross section F [mb·c], density distribution dn/dx_F, mean transverse momentum $\langle p_T \rangle$ [GeV/c], mean transverse momentum squared $\langle p_T^2 \rangle$ [(GeV/c)^2] as a function of x_F for π^+ and π^- in p+C collisions at 158 GeV/c beam momentum. The statistical uncertainty Δ for each quantity is given in %

p+p			p+C		
	π^+	π^-		π^+	π^-
y	dn/dy	dn/dy	y	dn/dy	dn/dy
			-0.6	0.9795	0.9311
			-0.4	0.9994	0.9521
			-0.2	1.0120	0.9688
0.0	0.7418	0.6713	0.0	1.0010	0.9646
0.2	0.7327	0.6567	0.2	0.9796	0.9317
0.4	0.7113	0.6281	0.4	0.9373	0.8751
0.6	0.6894	0.6022	0.6	0.8941	0.8159
0.8	0.6618	0.5760	0.8	0.8448	0.7597
1.0	0.6334	0.5425	1.0	0.7898	0.6905
1.2	0.6015	0.4973	1.2	0.7291	0.6131
1.4	0.5614	0.4426	1.4	0.6611	0.5296
1.6	0.5102	0.3841	1.6	0.5807	0.4451
1.8	0.4509	0.3191	1.8	0.4942	0.3612
2.0	0.3863	0.2534	2.0	0.4069	0.2806
2.2	0.3186	0.1964			
2.4	0.2525	0.1462			
2.6	0.1924	0.1034			
2.8	0.1420	0.0703			
3.0	0.1018	0.0463			
3.2	0.0698	0.0298			
3.4	0.0449	0.0179			
3.6	0.0255	0.00966			
3.8	0.0133	0.00446			
4.0	0.00621	0.00179			
4.2	0.00247	0.000566			
4.4	0.000755	0.000141			
4.6	0.000208	0.0000351			
4.8	0.0000396	0.0000065			

Table 6.3: p_T integrated density distribution dn/dy as a function of y for π^+ and π^- in p+p and p+C collisions at 158 GeV/c beam momentum

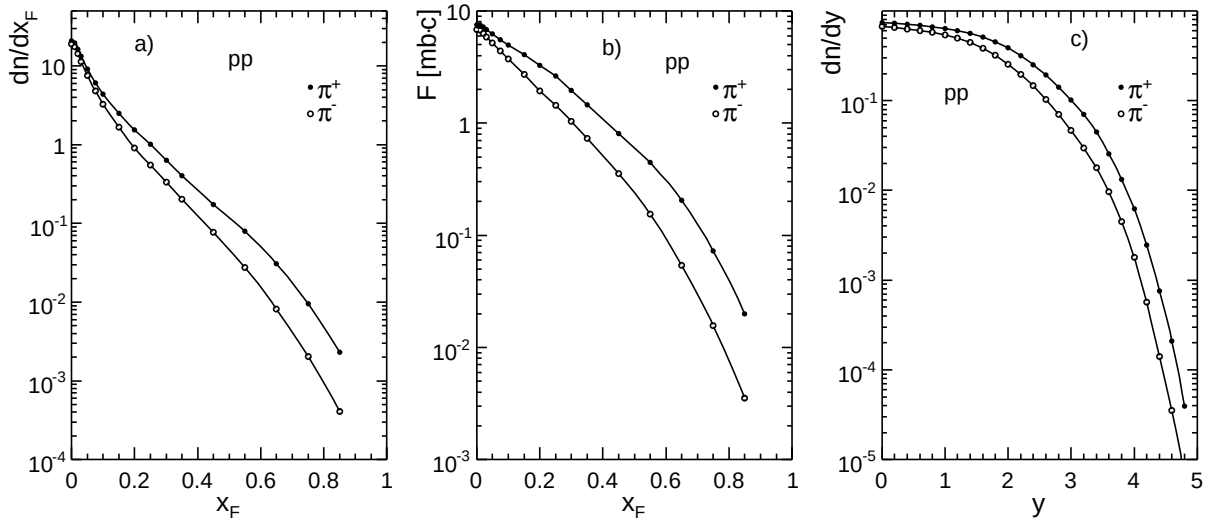

Figure 6.1: Integrated distributions of π^+ and π^- produced in p+p interactions at 158 GeV/c: a) density distribution dn/dx_F as a function of x_F; b) Integrated invariant cross section F as a function of x_F; c) density distribution dn/dy as a function of y

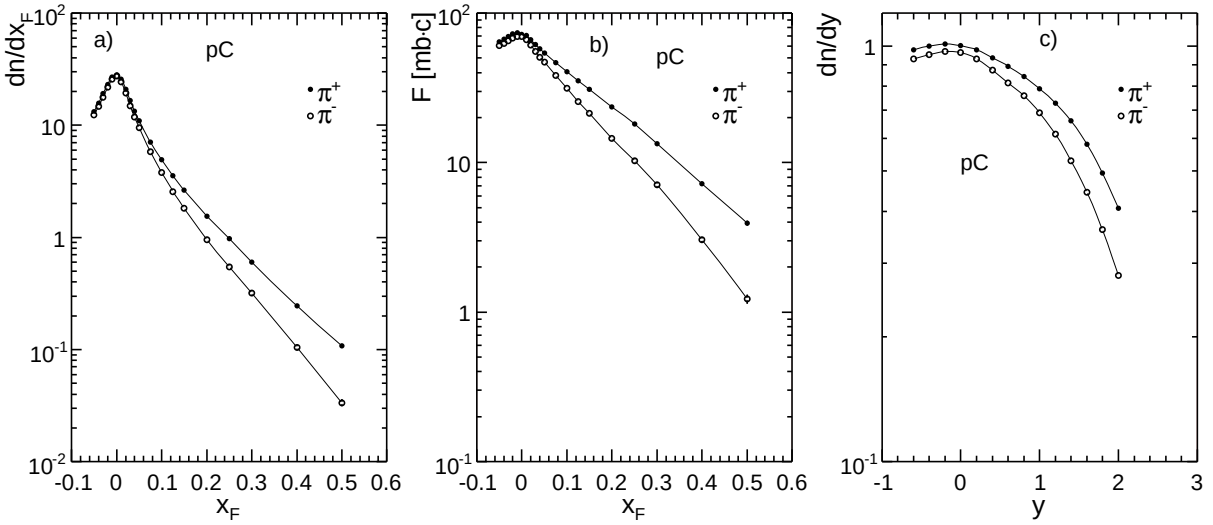

Figure 6.2: Integrated distributions of π^+ and π^- produced in p+C interactions at 158 GeV/c: a) density distribution dn/dx_F as a function of x_F; b) Integrated invariant cross section F as a function of x_F; c) density distribution dn/dy as a function of y

Other integrated quantities such as π^+/π^- ratio, the mean transverse momentum $\langle p_T \rangle$ and the mean transverse momentum squared $\langle p_T^2 \rangle$ again as a function of x_F are presented in Figs. 6.3 (p+p) and 6.4 (p+C). The first and second moments of the p_T distributions are larger for π^- than for π^+ in both reactions and there is a slight increase of this quantities in p+C collisions in comparison to p+p collisions. This increase is connected with the p_T enhancement at high transverse momentum in p+C interactions, see Ch. 8.

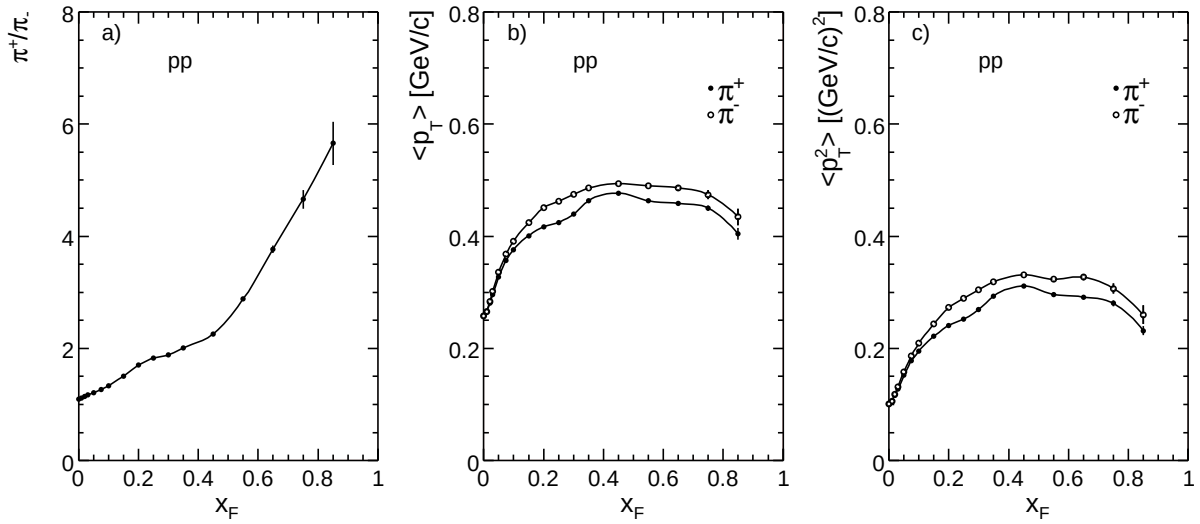

Figure 6.3: a) π^+/π^- ratio, b) mean p_T, and c) mean p_T^2 as a function of x_F for π^+ and π^- produced in p+p interactions at 158 GeV/c

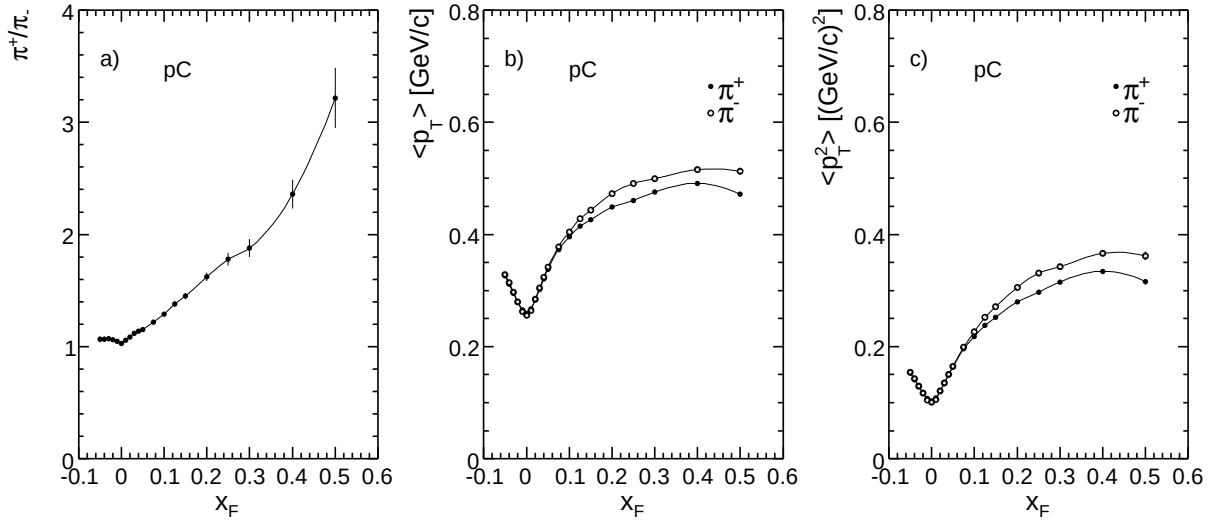

Figure 6.4: a) π^+/π^- ratio, b) mean p_T, and c) mean p_T^2 as a function of x_F for π^+ and π^- produced in p+C interactions at 158 GeV/c

6.2 Comparison to Other Experiments

The comparison in p+C with other experiments is not possible due to the absence of data with sufficient phase space coverage in transverse momentum allowing the integration of the quantities. Thus only NA49 results in p+p can be compared with available previous measurements.

In Fig. 6.5 is presented the comparison of p_T integrated invariant cross section from [21] with the NA49 measurement. Although the differential data are in very good agreement with each other (see Sect. 5.5.1), the p_T integrated distributions show sizable systematic deviations, as given in Fig. 6.5b. These deviations can be attributed to the incomplete phase space coverage of [21] which necessitates and extrapolation into the unmeasured

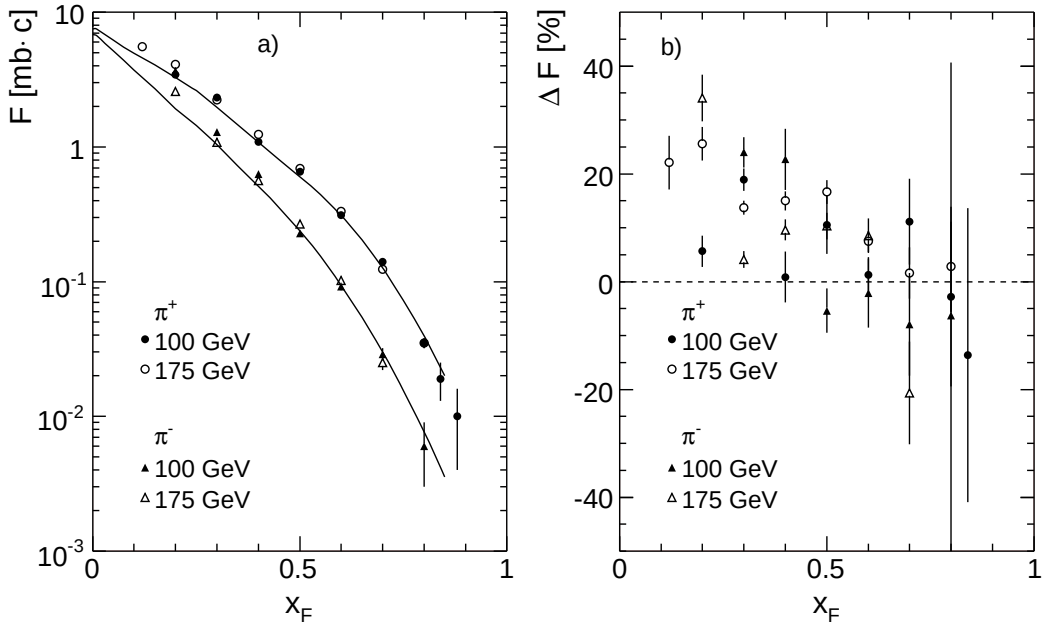

Figure 6.5: a) Comparison of p_T integrated invariant cross section F as a function of x_F for π^+ and π^- measured by [21] to NA49 results (presented with lines); b) deviation of the measurements of [21] from the NA49 results in percent

regions of p_T. The used exponential or Gaussian parametrization in [21] do not describe properly the p_T distributions, as was pointed out in Sect. 5.2, which leads to large deviations reaching more than 5σ.

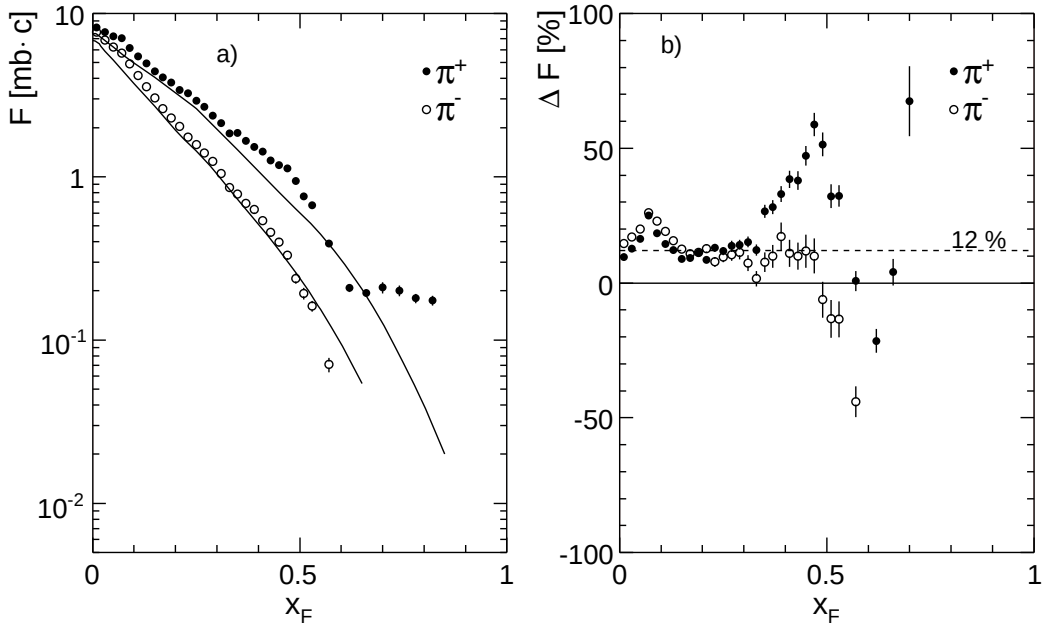

Figure 6.6: a) Comparison of p_T integrated invariant cross section F as a function of x_F for π^+ and π^- measured by [29] to NA49 results (presented with lines); b) deviation of the measurements of [29] from the NA49 results in percent

The EHS experiment which is directly comparable to NA49 in terms of phase space coverage and potential particle identification capability and which has accumulated a sizable data sample of 470k events at a beam momentum of 400 GeV/c has only published p_T integrated distributions of the invariant and non-invariant cross sections [29]. The comparison of invariant p_T integrated cross section as a function of x_F is presented in Fig. 6.6. As shown in Fig. 6.6b, an upward shift of about 12% is present up to $x_F \simeq 0.35$. This shift is not compatible with the precise fulfillment of x_F scaling exhibited by the ISR data (Sect. 5.5.3) in the same energy range. This indicates a normalization problem of the EHS data. Above $x_F = 0.35$, the EHS results show large systematic effects especially for the π^+ yields which can be attributed to misidentification of π^+.

A comparison of the p_T integrated π^+/π^- ratio with data from [21] and [29] and mean p_T^2 with [29] is shown in Fig. 6.7. The π^+/π^- ratios agree well. Only the measurement from [29] deviates for $x_F > 0.3$. The second moments of the p_T distributions show an upwards trend also below this x_F value which complies with the expected s-dependence of this quantity.

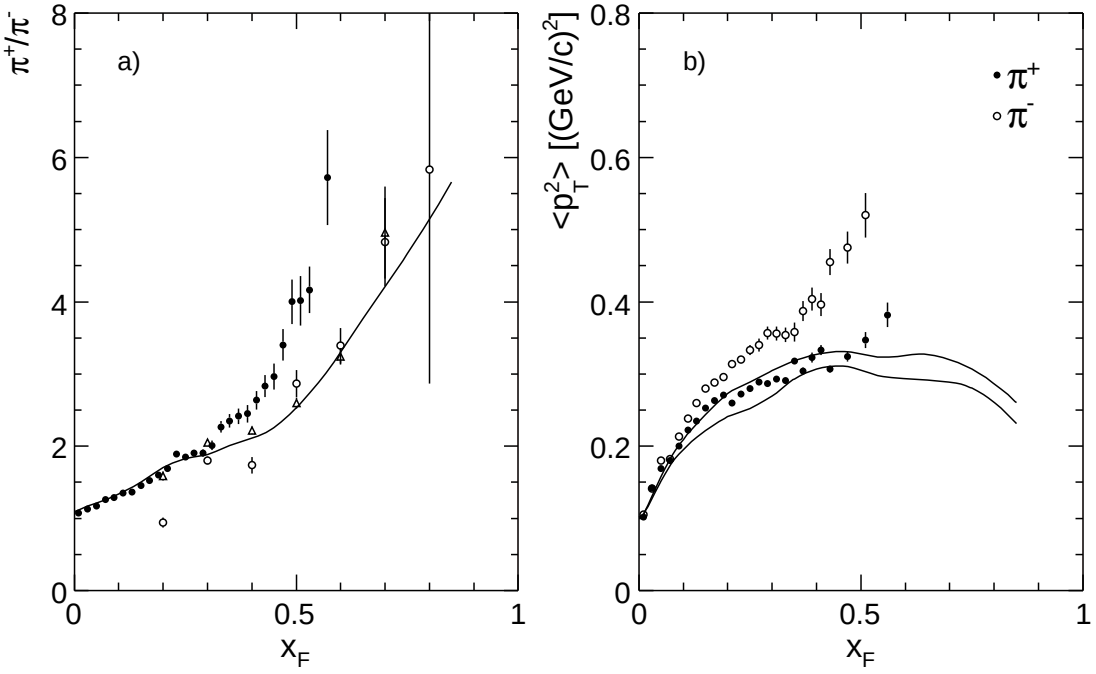

Figure 6.7: a) Comparison of p_T integrated π^+/π^- ratio as a function of x_F measured by [21] (open symbols) and [29] (full circles) to NA49 results (lines); b) comparison of the mean p_T^2 as a function of x_F for π^+ and π^- measured by [29] to NA49 results (lines)

Chapter 7

Longitudinal p_T-integrated dependence of pion production

The hadronization process in hadron-nucleus interactions consists of three distinct components:

- The projectile fragmentation which carries the imprint of multiple collisions in nuclear matter.
- The fragmentation of the participating target nucleons.
- The contribution from intranuclear cascading which is generated by the propagation and interaction of the participating nucleons and produced hadrons inside the nucleus.

The separation and quantification of these components in a model independent way is the main goal of this chapter. Such a separation was demonstrated by the NA49 experiment for the net proton production [17] exploring the baryon number conservation. In this case the pion projectile was used which didn't carry baryon number and thus measures directly the target component.

There is no such a conservation law for the pion production. In addition the target cascading part extends closer to the central region than for protons, up to x_F values of about -0.05. Both the target and the projectile components extend into the respective opposite hemispheres with a priori unknown ranges and shapes of the longitudinal momentum distributions which has to be determined experimentally. This extent is called feed-over.

For the present study the reference of the proton-carbon results to the elementary hadron-proton interactions is absolutely essential and most of the argumentation will be established in direct comparison to these processes, invoking isospin symmetry as an important constraint for the constitution of the target contribution. In this respect the inspection of two components in p+p reaction is necessary condition for the data interpretation.

7.1 Two-component picture in p+p collisions

The separation of the target and projectile components in p+p collisions is built around the three experimental facts:

- The absence of long-range two-particle correlations at $|x_F| > 0.2$.
- The presence of forward-backward multiplicity correlations at $|x_F| < 0.1$.
- The x_F dependence of the π^+/π^- ratio in $\langle\pi\rangle$+p collisions.

7.1.1 Long range two particle correlations

A precision study of forward-backward correlation in p+p collisions has been performed at the CERN ISR [19] for the different combinations of secondary identified particles. The correlation quotient Q is defined as:

$$Q(x_1, x_2) = \frac{g(x_1, x_2)}{f(x_1) \cdot f(x_2)} \sigma_{\text{trig}}, \tag{7.1}$$

where x_1 and x_2 are Feynman x of the two particles and f and g denote one and two-particle cross section, respectively. The correlation quotient Q is shown in Fig. 7.1 for several combination of secondary particles.

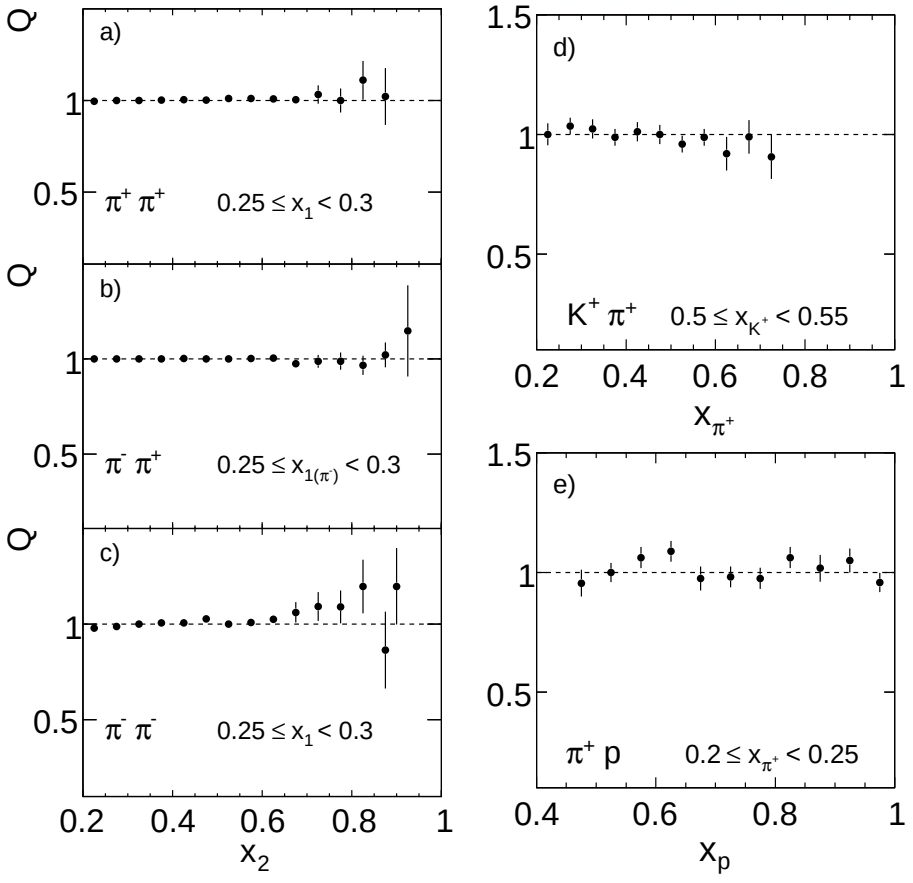

Figure 7.1: Forward-backward correlations in p+p collisions measured by [19] for: a) $\pi^+\pi^+$, b) $\pi^-\pi^+$, c) $\pi^-\pi^-$, d) $K^+\pi^+$, and e) π^+p

In the covered region of the experiment which is $|x_F| > 0.2$ for pions and $|x_F| > 0.4$ for protons and kaons no deviation of Q from unity is visible within the tight error bars. The only exception is the large x_F region where energy momentum conservation will impose some correlation of kinematic origin.

These measurements proof that there is no correlations between forward and backward hemispheres above the limit of $|x_F| = 0.2$.

7.1.2 Forward-backward multiplicity correlations

The experiment [19] does not cover the central rapidity area. This region has been studied by three bubble chamber experiments [31–33] at SPS energies and a streamer chamber experiment at ISR [34] by measuring the forward-backward multiplicity correlation without particle identification. The bubble chamber experiments cover the full x_F range by momentum measurement in the laboratory frame. The Lorentz transformation is made with assumption of pion mass which makes a certain but negligible bias in determination of the central region. The experiment [34] has no momentum measurement and determines the pseudo-rapidity η by the angle measurement.

The forward-backward multiplicity correlation are quantified by plotting the dependence of mean backward charged multiplicity $\langle n_b \rangle$ on the forward charged multiplicity n_f.

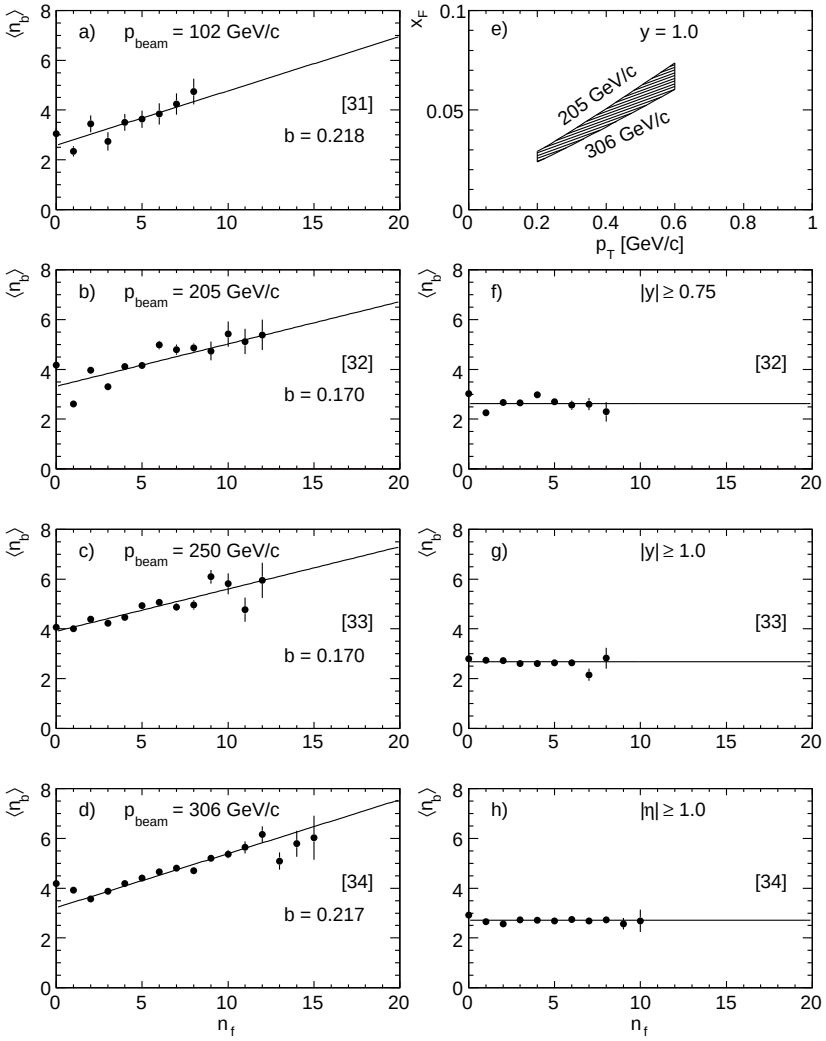

Figure 7.2: Forward-backward multiplicity correlations, a) to d) experimental data and fits, [31–34]; f) to h) correlation with rapidity selection as given, [32–34]; d) x_F as a function of p_T at $y = 1$ for beam momentum between 205 and 306 GeV/c

This dependence measured by experiments [31–34] is presented in Fig. 7.2.

All of the experiments find a linear correlation of the type

$$\langle n_b \rangle = a + b \cdot n_f \tag{7.2}$$

with the values of the slope parameter b ranging from 0.17 to 0.22 for $\sqrt{s}$ between 14 and 24 GeV, Fig. 7.2a-d. These results do not contradict the measurements from [19] as here also the central region contributes. In fact the observed multiplicity correlations vanish when the central region is excluded ($|y| > 1$ or $\eta > 1$), as shown in Fig. 7.2f-h. These cuts around the mean transverse momentum corresponds to x_F between 0.04 and 0.06 which is well below the lower x_F limit of [19].

It can be concluded from the above results that feed-over range of produced pions into the opposite hemisphere is limited to about $|x_F| \sim 0.05$ at average transverse momentum. The feed-over contains between 17 and 21 % of all pions. There is no further long-range correlation beyond this limit.

7.1.3 π^+/π^- ratio in π+p collisions

Additional information about range and shape of the feed-over can be extracted from the π^+/π^- ratio in $\langle\pi\rangle$+p collisions, where $\langle\pi\rangle$+p indicates the average of π^++p and π^-+p interactions. The advantage of forming $\langle\pi\rangle$ projectile is that it is isospin symmetric which leads to the fact that π^+/π^- ratio will be exactly equal to unity for the whole projectile fragmentation. Therefore by measurement of the π^+/π^- ratio as a function of x_F one can obtain directly the extent and the shape of the pion feed-over into the forward hemisphere using the deviation of the ratio from unity.

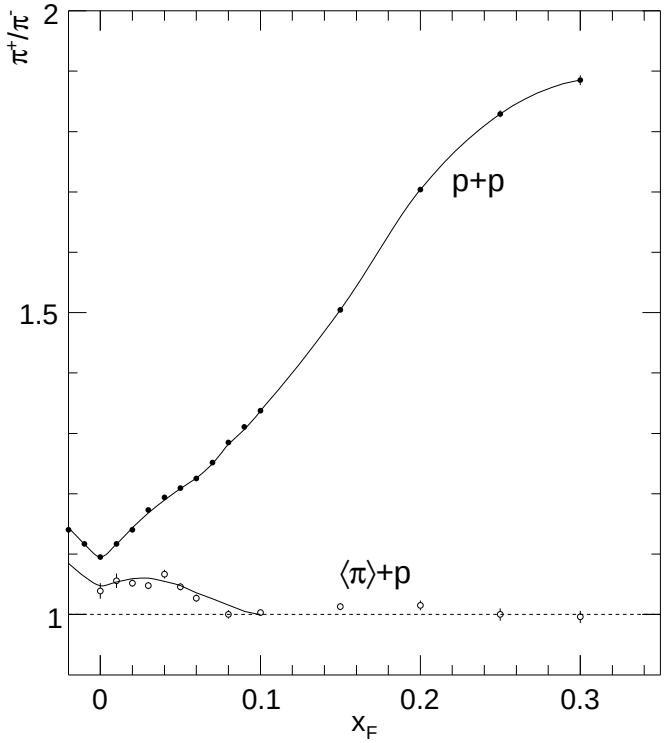

Figure 7.3: π^+/π^- ratio as a function of x_F in p+p and $\langle\pi\rangle$+p

The π^+/π^- ratio in π^++p and π^-+p collisions has been measured by NA49 detector. It has been shown that isospin symmetry is fulfilled for $x_F > 0.1$ in these reactions [18], i.e. π^+ and π^- interchange their yields by switching from π^+ to π^- projectile. In the resulting π^+/π^- ratio most of the corrections drop out and the only exception is the feed-down from the weak decay of the proton target fragmentation. Its contribution to π^+/π^- ratio in the forward region is less 0.5% and it has been corrected for.

The measured π^+/π^- ratio in $\langle\pi\rangle$+p collisions is presented in Fig. 7.3 together with the ratio in p+p reactions.

The π^+/π^- ratio reaches unity at $x_F \sim 0.08$ and stays constant at this value up to the limit of the data extraction at $x_F = 0.3$. The same ratio in p+p collisions, also presented in Fig. 7.3, strongly increases with x_F which reflects the presence of proton projectile. The approach of the charge ratio to unity in $\langle\pi\rangle$+p reaction is not smooth but shows a local maximum at $x_F \sim 0.04$.

7.1.4 Extraction of target and projectile components in p+p collisions

The two-component picture of pion production in p+p can be constructed based on the experimental results presented in the previous three sections. The two components correspond to target and projectile contribution. These components are independent which means that target fragmentation does not depend on the projectile particle and vise-versa and they have to fulfill the following conditions:

- The target and projectile components must be equal at $x_F = 0$ for symmetry reasons.
- The components feed-over into the opposite hemisphere with the maximum extent of $x_F = 0.1$, see Sect. 7.1.3.
- The feed-over is at the level of about 19% of the total yield per component, see Sect. 7.1.2.

The discussion can be simplified by using the p_T integrated charge-averaged longitudinal momentum distribution $\langle\pi\rangle$, defined as:

$$\langle\pi\rangle = \frac{1}{2}\left[\left(\frac{dn}{dx_F}\right)^{\pi^+} + \left(\frac{dn}{dx_F}\right)^{\pi^-}\right], \tag{7.3}$$

which allows to exclude the isospin dependence.

The x_F dependence of the two components, satisfying the above constraints, for $\langle\pi\rangle$ in p+p collisions is shown in Fig. 7.4 together with the measured total inclusive yield.

The observed structure in π^+/π^- ratio in $\langle\pi\rangle$+p collisions around $x_F = 0.04$ (Fig. 7.3) suggests slightly different shape of the feed-over curve for π^+ and π^-. In fact there is no a priori knowledge of the behaviour of the two charges in the feed-over region. In Fig. 7.5 is shown the contribution of the target component relative to the total inclusive yield for π^+ and π^-.

The assumed different behaviour of π^+ and π^- leads to increase of the π^+/π^- ratio into the feed-over region. This prediction is shown with lines in Fig. 7.6 for p+p interactions in forward hemisphere where the π^+/π^- ratio from the target component is much larger than that from the projectile component. The above description gives a simultaneous explanation of the slight shoulder and the structure observed at $x_F \sim 0.04$ in both reactions p+p and $\langle\pi\rangle$+p. This corresponds to long-range charge correlation within the

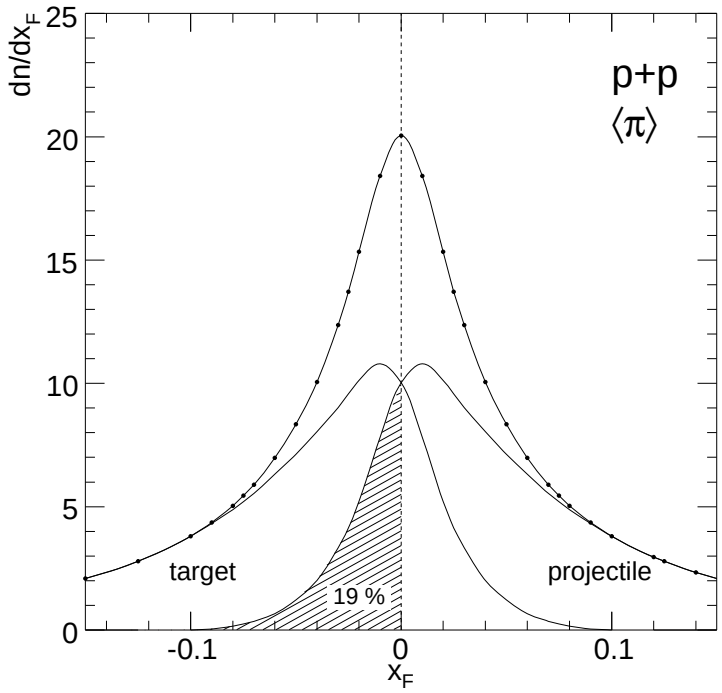

Figure 7.4: Two-component picture of charge-averaged pion production in p+p collisions, showing the symmetric contribution from the target and projectile and their sum corresponding to the data

target and projectile contribution with the respective incoming hadron. This correlation will present an interesting challenge for microscopic production models, in particular for those based on string fragmentation ideas, as the memory of the original parton charge tends to be quickly lost along the string [62].

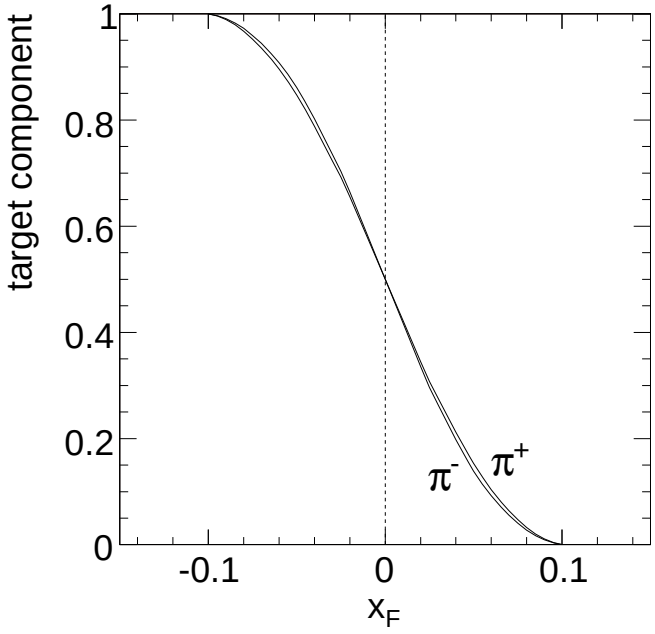

Figure 7.5: Target component contribution of π^+ and π^- with respect to the total yield

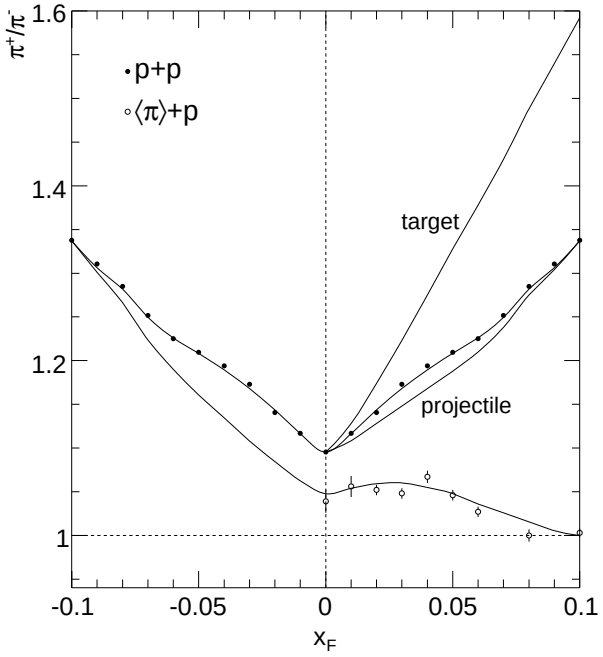

Figure 7.6: π^+/π^- ratio in p+p and $\langle\pi\rangle$+p with corresponding predictions for the proton target and proton projectile components

7.1.5 Comparison to feed-over in net baryon production

The two-component nature of the net baryon production has been also extracted by NA49 data from p+p and $\langle\pi\rangle$+p reactions. The advantage of the net baryon production is the conservation of the baryon number which allows to measure the target contribution directly by using baryon number free projectile. It has been shown that the pion induced interactions and the forward-backward baryon correlation in p+p give the consistent results [14]. The feed-over distribution has been measured directly in three different ways. The result is summarized in Fig. 7.7a.

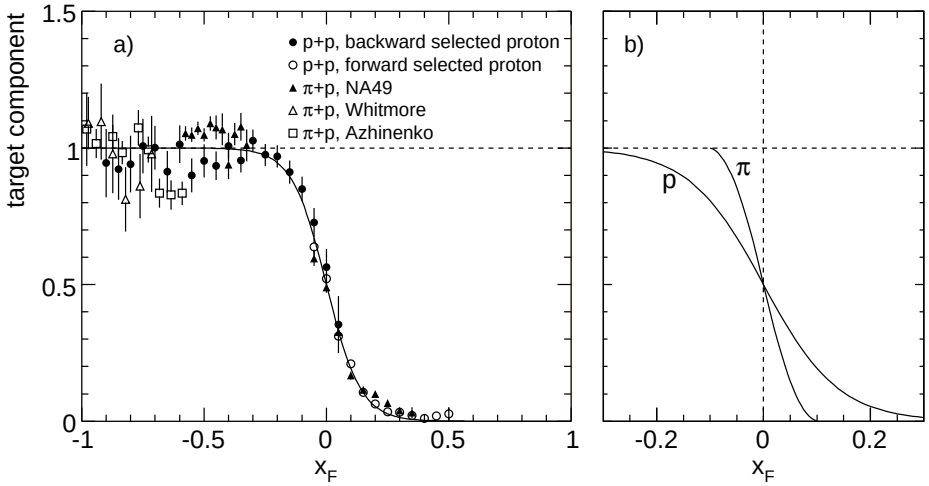

Figure 7.7: a) Target component for net protons measured with different methods and b) target components of $\langle\pi\rangle$ and net protons

In Fig. 7.7b the comparison of pion feed-over to net proton feed-over is presented. There is a clear difference between the feed-over range which indicates a strong mass dependence.

7.2 Nuclear aspects

The most important quantity which defines the nuclear parameters is the nuclear density distribution $\rho(r)$. A very distinct assumption about this quantity has to be made to determine the probability distribution of multiple collisions, $P(\nu)$, where ν is the number of collisions which the projectile undergo inside the nucleus. Other quantities of principle interest are the mean number of collisions $\langle\nu\rangle$ and the proton-nucleus total inelastic cross section, or rather its evolution with subsequent collisions.

7.2.1 Nuclear density distribution

The experimental information about nuclear density distribution of Carbon nucleus is available from the electron scattering [63, 64] which measure the charge distribution of the nucleons inside the nucleus. This is not identical to the density $\rho(r)$ as the spatial distribution has to be unfolded. An additional problem can be the possible different distribution of protons and neutrons. To overcome all these uncertainties in the density distribution six different parametrizations were used [65]:

1. Woods-Saxon
2. Single Gaussian

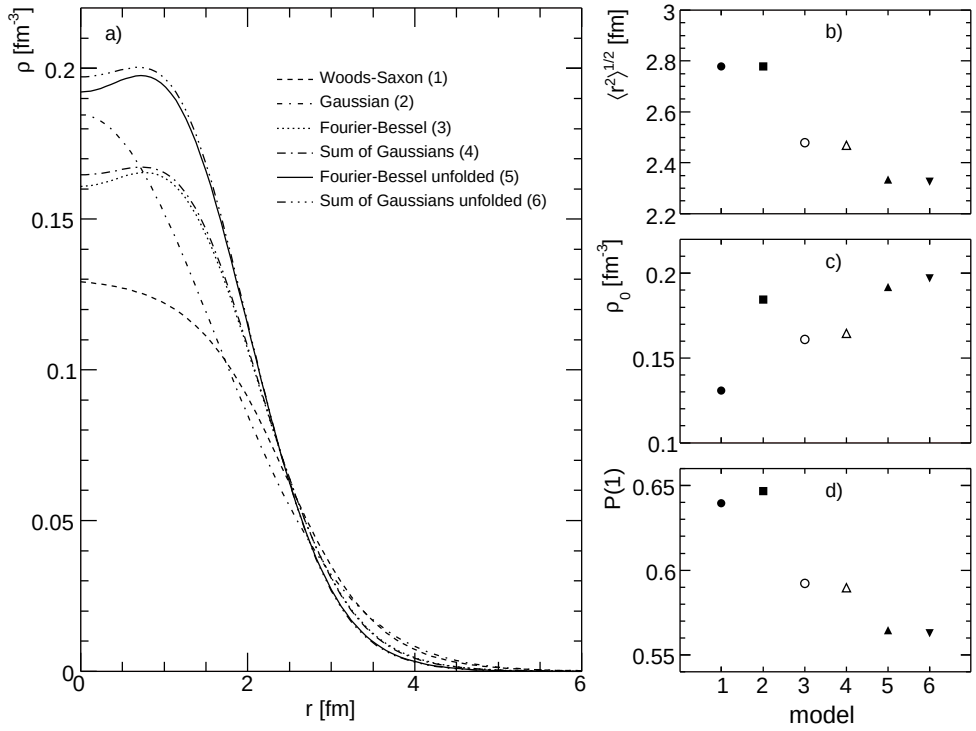

Figure 7.8: a) Nuclear density parametrizations; b) rms radius; c) nuclear density at $r = 0$; d) probability for single collision

3. Fourier-Bessel
4. Sum of Gaussians
5. Fourier-Bessel unfolded for proton charge distribution
6. Sum of Gaussians unfolded for proton charge distribution

The nuclear density $\rho(r)$ for the six parametrizations as a function of the radius are presented in Fig. 7.8, where also the resulting nuclear parameters like the rms radius, central nuclear density $\rho(r = 0)$ and probability for single collision P(1) are given. The first two options are known to disagree with the experiment. From the other parametrizations it can be concluded that rms radius is between 2.3 and 2.5 fm and the probability for the single collision is between 0.56 and 0.6. The latter quantity shows the fraction of the interactions which are identical to the "trivial" proton-nucleon collisions.

7.2.2 Mean number of collisions, total inelastic cross section

Mean number of collisions can be obtained in a simple geometrical manner, as shown in Fig. 7.9. Let's assume that we have distributed randomly A circular disks each with surface S. The area covered by one layer of disks is denoted with S_1, by two layers with S_2, by three layers with S_3 etc. Then scanning the plane with random projectile the mean hit number of layers is defined by the formula:

$$\langle \nu \rangle = \frac{S_1 + 2S_2 + 3S_3 + \ldots + AS_A}{S_1 + S_2 + S_3 + \ldots + S_A}. \tag{7.4}$$

The total area covered by the disks represents the total inelastic cross section σ^{pA} and the total surface of the disks $A\sigma^{\mathrm{pp}}$.

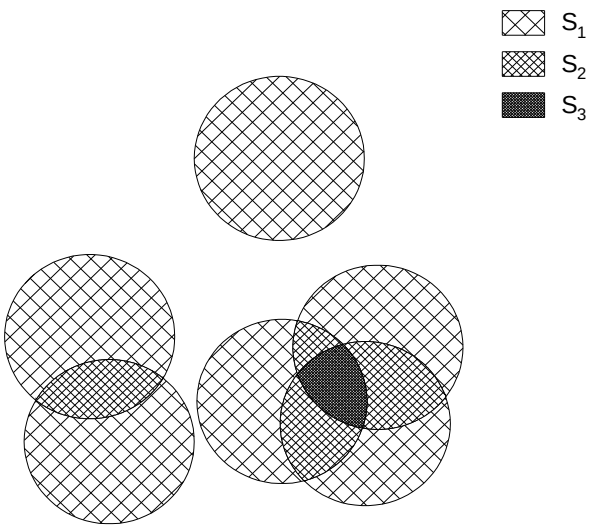

Figure 7.9: Schematic view of the superposition of nucleon-nucleon cross sections in a nuclear environment

$$\sigma^{\mathrm{pA}} = S_1 + S_2 + S_3 + \ldots + S_A \tag{7.5}$$

$$A\sigma^{\mathrm{pp}} = S_1 + 2S_2 + 3S_3 + \ldots + AS_A. \tag{7.6}$$

Then the mean number of collisions can be written as:

$$\langle \nu \rangle = \frac{A\sigma^{\mathrm{pp}}}{\sigma^{\mathrm{pA}}}. \tag{7.7}$$

which in case of carbon nucleus corresponds to the mean number of collisions $\langle \nu \rangle = 1.68$.

In the case of p+A collisions this formula is valid if the elementary proton-nucleon cross section is the same in each successive hit. Therefore any experimental verification of the correctness of Eq. 7.7 will provide an important constraint on the evolution of the cross section with the number of collisions.

Under the above assumption, the distribution of the number of collisions $P(\nu)$ has been determined via Monte Carlo calculation [65], using the six parametrization discussed in Sect. 7.2.1. The resulting $P(\nu)$ for the different parametrizations are presented in Fig 7.10a. In Fig 7.10b-d are given the calculated total inelastic cross section, mean number of collisions and mean number of collisions for $\nu \geq 2$.

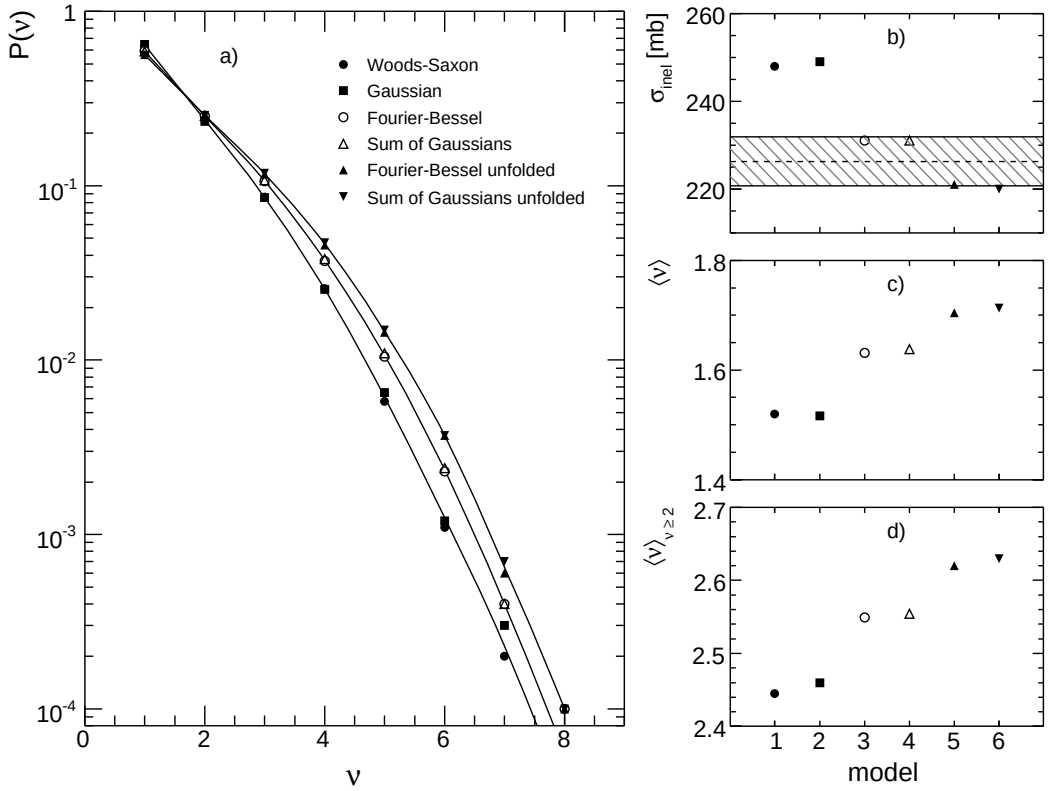

Figure 7.10: a) Probability of ν collisions for different nuclear density parametrizations; b) inelastic cross section. The dashed line indicates the NA49 result with the error margin (shaded area); c) mean number of collisions; d) mean number of collisions for $\nu \geq 2$

The measured total inelastic cross section by NA49 is 226.3 mb $\pm$ 2% (see Table 4.1) which gives constraint on the nuclear density distribution and favours the parametrizations (5) and (6).

7.3 Two-component picture of pion production in p+C collisions

Two-component picture in p+C collisions will be constructed based on the two-component picture in p+p interactions developed in Sect. 7.1. In order to quantify the superposition several straight-forward assumptions have to be made:

- Concerning the feed-over shape and x_F range both the target and projectile components will follow the same mechanism as extracted for the elementary collisions.
- The target component will be multiplied with the mean number of projectile collisions $\langle\nu\rangle$. Here the underlying assumption is that any subsequent collision leads to the same density distribution.
- As was mentioned above due to the isoscalar nature of Carbon nucleus, the target component for both π^+ and π^- is build up as:

$$\left(\frac{dn}{dx_F}\right)^{\pi^\pm}_{\text{target}}(x_F) = \frac{1}{2}\left(\frac{dn}{dx_F}\right)^{\pi^+,\text{pp}}_{\text{target}}(x_F) + \frac{1}{2}\left(\frac{dn}{dx_F}\right)^{\pi^-,\text{pp}}_{\text{target}}(x_F), \tag{7.8}$$

  which results as necessary in a π^+/π^- ratio of unity over the full x_F range.
- The projectile component carries the full imprint of $\langle\nu\rangle$ which makes it impossible to be predicted. For this reason it will be constructed the same as in p+p collisions:

$$\left(\frac{dn}{dx_F}\right)^{\pi^\pm}_{\text{proj}}(x_F) = \left(\frac{dn}{dx_F}\right)^{\pi^\pm,\text{pp}}_{\text{proj}}(x_F), \tag{7.9}$$

  with the aim to be extracted by inspecting the deviation of this simple relation from the data.

With these assumptions, a predicted pion yield in p+C interactions can be obtained as follows:

$$\left(\frac{dn}{dx_F}\right)^{\pi^\pm}_{\text{pred}}(x_F) = \langle\nu\rangle\left(\frac{dn}{dx_F}\right)^{\pi^\pm}_{\text{target}}(x_F) + \left(\frac{dn}{dx_F}\right)^{\pi^\pm}_{\text{proj}}(x_F). \tag{7.10}$$

7.4 Comparison of two-component picture in p+C reaction with the data

To simplify the comparison of the above prediction with the data the following two ratios are formed:

$$R(x_F) = \frac{(dn/dx_F)^{\text{pC}}(x_F)}{(dn/dx_F)^{\text{pp}}(x_F)} \tag{7.11}$$

$$R_{\text{pred}}(x_F) = \frac{(dn/dx_F)_{\text{pred}}(x_F)}{(dn/dx_F)^{\text{pp}}(x_F)}, \tag{7.12}$$

where $(dn/dx_F)^{\text{pC}}(x_F)$ and $(dn/dx_F)^{\text{pp}}(x_F)$ are measured yields in p+C and p+p collisions respectively, and $(dn/dx_F)_{\text{pred}}(x_F)$ is the predicted by two-component picture yield, Eq. 7.10.

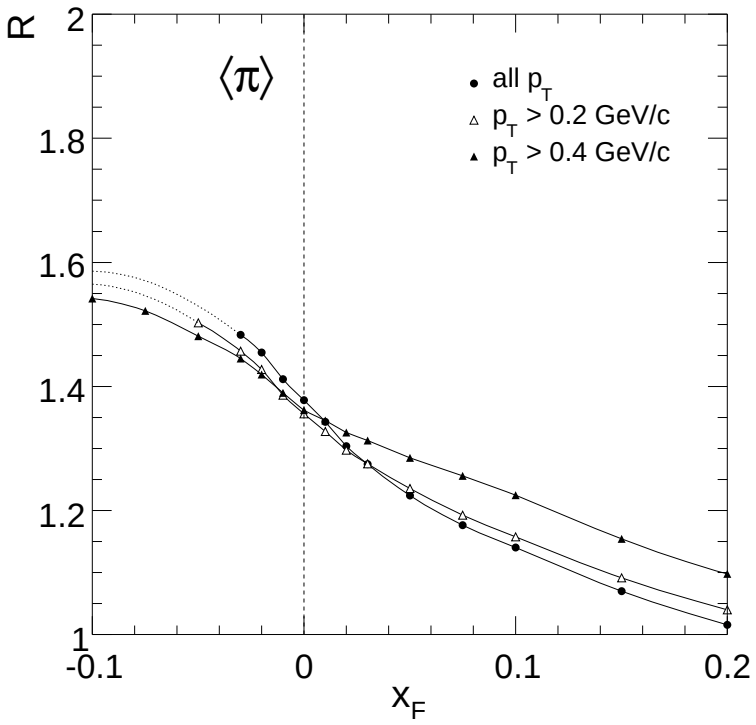

Figure 7.11: Ratio $R(x_F)$ in the central region as a function of x_F for the charge-average pion $\langle\pi\rangle$ obtained with lower integration limits at p_T = 0, 0.2 and 0.4 GeV/c. The dotted lines indicate the extrapolation

7.4.1 Average charge

Since the acceptance of the NA49 detector in the backward region has a limitation to x_F = -0.03 for the complete integration of the p_T distribution (see Fig. 3.5), an extrapolation of $R(x_F)$ to x_F = -0.1 concerning the lowest p_T range, has been performed. The validity of the extrapolation towards x_F = -0.1 has been tested by studying the sensitivity of the integrated yields to a lower p_T cut off. The measured ratio $R(x_F)$ in the central region obtained with the lower integration p_T limit at 0, 0.2 and 0.4 GeV/c is presented in Fig. 7.11. For the latter value the full region down to x_F = -0.1 is experimentally available. It appears that change of the ratio in the backward region with increasing the p_T cut-off is on the percent level and therefore can be regarded as a second order effect.

The measured ratio $R(x_F)$ extrapolated down to x_F = -0.1 is presented in Fig. 7.12. The upper limit of the data at x_F = 0.5 is due to the limited statistics in p+C event sample. The predicted ratio $R_{\rm pred}(x_F)$ by the two-component picture is also shown in Fig. 7.12 for the three values of mean number of collisions $\langle\nu\rangle$ = 1.5, 1.6 and 1.7.

Several interesting features has emerged by comparing the measured ratio $R(x_F)$ at backward, central and forward region with the predicted ratio $R_{\rm pred}(x_F)$:

- In the backward hemisphere at x_F towards -0.1 the ratio $R(x_F)$ reaches a value of about 1.6. Here the total contribution to the yield comes from the target component (Fig. 7.4) and this factor of 1.6 will be measurement of the mean number of projectile collisions $\langle\nu\rangle$ in Carbon nucleus (Eq. 7.10). The extracted in this way $\langle\nu\rangle$ = 1.6 is significantly below (4σ) the value of 1.68 predicted in Sect. 7.2.2.

- In the central region at x_F = 0 the measured value is 1.38 which is slightly above

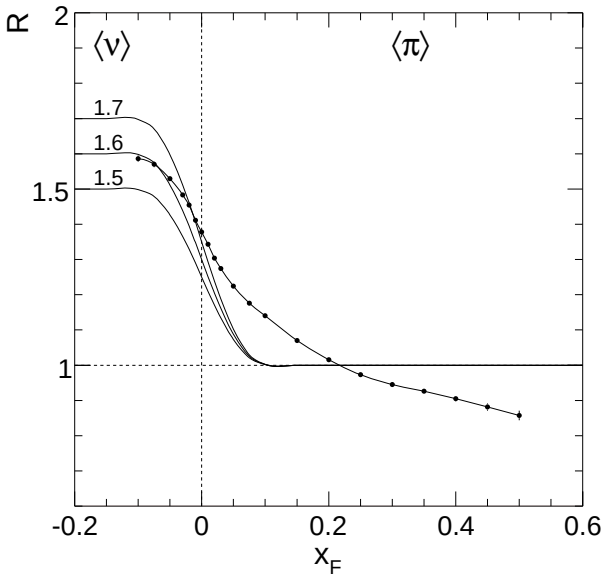

Figure 7.12: Ratio $R(x_F)$ as a function of x_F for the charge-average pion $\langle\pi\rangle$ (full circles) in comparison with $R_{\rm pred}$ for three different $\langle\nu\rangle = 1.5$, 1.6 and 1.7 (lines)

the straight-forward prediction of two-component picture $(\langle\nu\rangle + 1)/2$, indicating an enhancement of the projectile component.

- In the forward region up to $x_F \sim 0.2$ the measured ratio $R(x_F)$ is bigger than predicted ratio $R_{\rm pred}(x_F)$ and become smaller above this x_F value. The decrease of baryon production in p+A in comparison with p+p in the far forward hemisphere is well known phenomenon in projectile fragmentation. Here this decrease is observed in pion production which can be called "pion stopping".

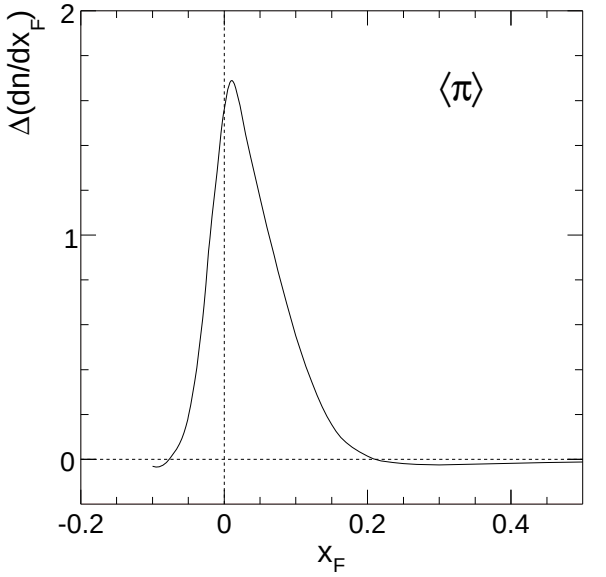

Figure 7.13: Difference between measured ratio $R(x_F)$ and predicted $R_{\rm pred}(x_F)$ as a function of x_F for $\langle\pi\rangle$

The increased particle density in the x_F region between -0.1 and 0.2 is due to the superposition of both target and projectile components. With the assumption that target component in p+C collisions is equal to $\langle\nu\rangle \cdot (dn/dx_F)^{\mathrm{pp}}_{\mathrm{target}}$ the enhancement of the projectile component will be given as difference between R and R_{pred}. This deviation is shown in Fig. 7.13. Integrating this density difference results in total projectile pion yields enhancement of about 10% of p+C reaction compared to p+p collisions.

7.4.2 Charge dependence

The measured ratio $R(x_F)$ separately for π^+ and π^- with lower integration limits at $p_T = 0$, 0.2, 0.4 GeV/c is plotted in Fig. 7.14. Again, as in the case of average pion yield, the change of ratio in the backward region is at the level of a few percent which confirms validity of the extrapolation.

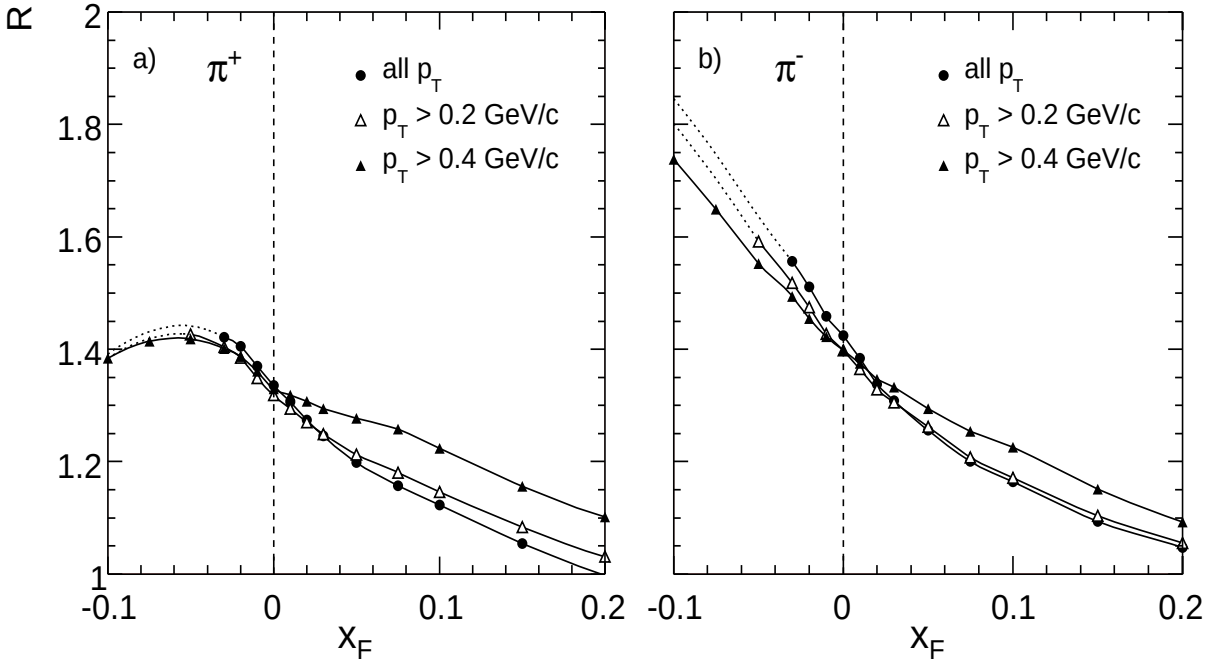

Figure 7.14: Ratio $R(x_F)$ in the central region as a function of x_F obtained with lower integration limits at $p_T = 0$, 0.2 and 0.4 GeV/c for a) π^+ and b) π^-. The dotted lines indicate the extrapolation

The comparison of the ratio $R(x_F)$ for the charged pions with the predicted by two-component picture $R_{\mathrm{pred}}(x_F)$ is shown in Fig. 7.15. Clearly both charges approach the prediction for mean number of collisions $\langle\nu\rangle$ of 1.6 in the backward region. In the central region up to $x_F \sim 0.2$ the measurement is above the prediction, and for larger x_F become smaller.

The behaviour of the charges is evidently different in the backward hemisphere as well as in the forward. The bigger increase in the backward region for π^- is directly related to the target. Due to isospin symmetry of the Carbon nucleus the production of positive and negative pions is equal. This effect enhances more the π^- and less the π^+ yield from the target relative to the p+p interactions. As for π^+ a local maximum of R around x_F = -0.05 is followed by decrease towards lower x_F, for π^- a steady increase of R in the same region is observed. In the forward region for $x_F > 0.3$ the ratio R decreases more

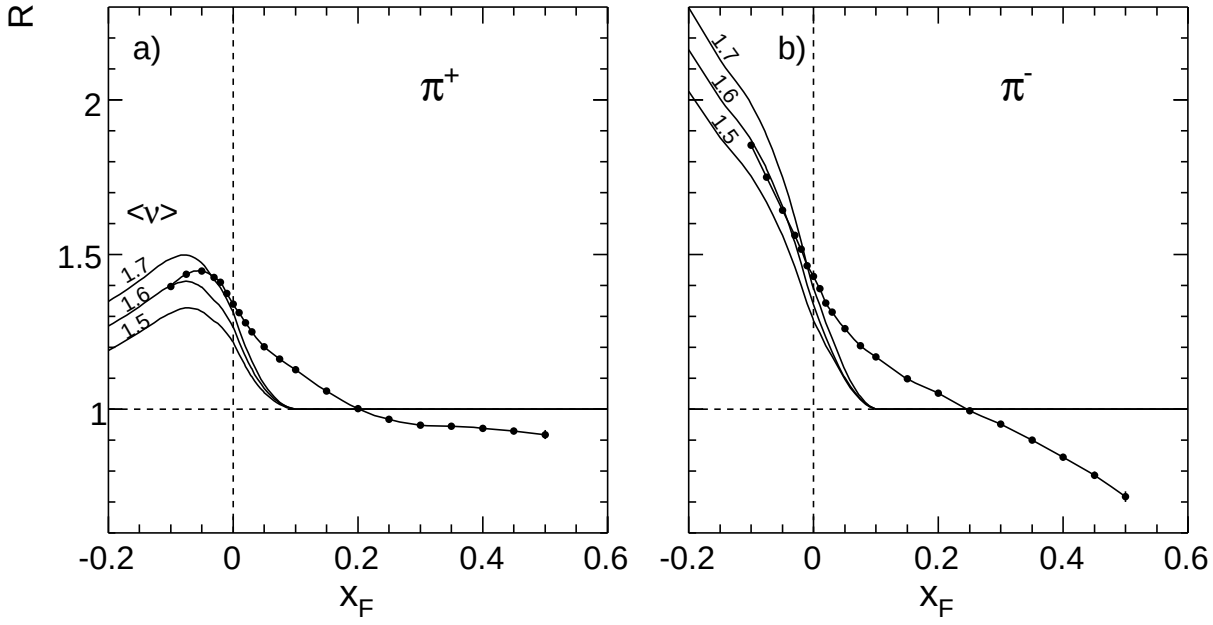

Figure 7.15: Ratio $R(x_F)$ as a function of x_F in comparison with $R_{\rm pred}(x_F)$ for three different $\langle\nu\rangle$ = 1.5, 1.6 and 1.7 (lines) for a) π^+ and b) π^-

rapidly for π^- than for π^+ which is a signal for the important differences of the projectile fragmentation mechanism between the two charges.

7.4.3 π^+/π^- ratio

The π^+/π^- ratio in p+C and p+p interactions as a function of x_F is shown in Fig. 7.16. An enlarged view of the central and backward x_F regions is also presented in Fig. 7.16b for different p_T cut-offs in the transverse momentum integration, giving further support to the extrapolation used at low p_T.

In the backward hemisphere the π^+/π^- ratio in p+C collisions approaches unity as it is expected from the isospin symmetry in the target fragmentation region. In the forward hemisphere the ratio is close to the one measured in p+p interactions which is signal for domination of the projectile fragmentation. The behaviour of the π^+/π^- ratio for $x_F <$ -0.1 and $x_F > 0.1$ complies well with prediction from two-component picture in the sense that π^+/π^- ratio tends to 1 in the region of prevailing target contribution (see Eq. 7.8) and it is similar to the ratio observed in p+p reaction in the region where the projectile contribution dominates (see Eq. 7.9). However the ratio does not behave in a smooth fashion but show detailed deviation from the first-order expectation. The approach to unity at negative x_F shows a local maximum at $x_F \sim$ -0.04 which is similar to that observed in $\langle\pi\rangle$+p interactions at the same positive x_F (see Sect. 7.1.3), corresponding in both cases to isoscalar fragmentation region. In the forward hemisphere the π^+/π^- ratio is not identical to the ratio in p+p collisions, as it is smaller for $x_F < 0.3$ and bigger for larger x_F values. These deviations indicate a modification of the projectile charge ratio in multiple collision processes both in forward and backward hemispheres.

The deviation of the projectile charge ratio from the one measured in p+p collisions can be extracted by using the two-component picture developed in Sect. 7.3 which explicitly contains π^+/π^- ratio equals to 1 for the target component. The resulting

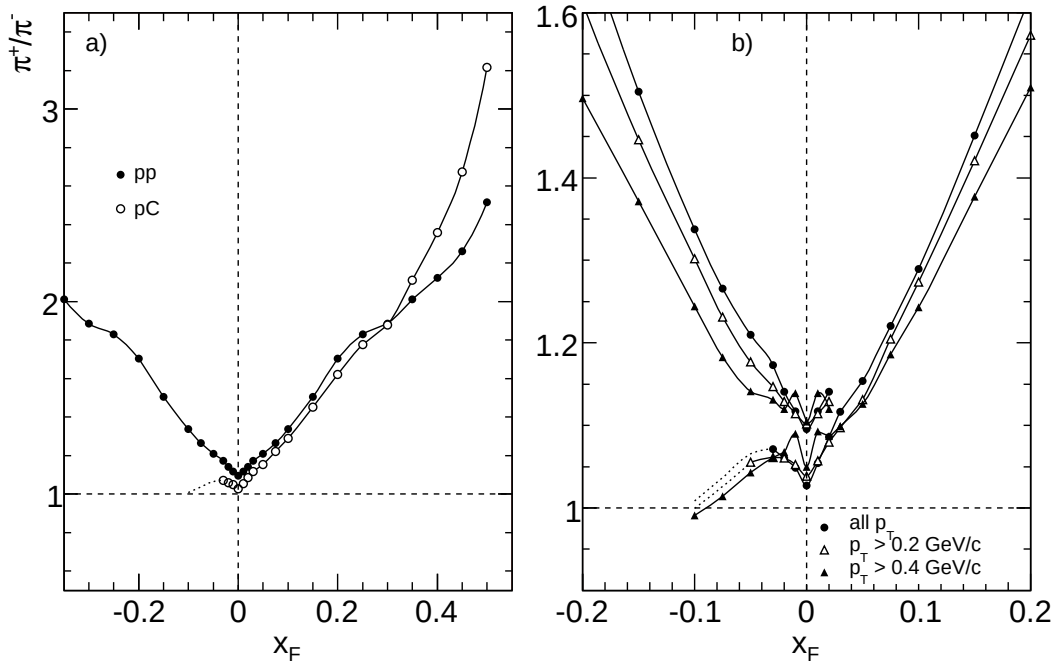

Figure 7.16: p_T integrated π^+/π^- ratio as a function of x_F in p+p and p+C interactions a) without p_T cut off and b) with p_T cut off included where the data points in p+p collisions are plotted only up to $x_F = 0.02$

$(\pi^+/\pi^-)^{\mathrm{pC}}_{\mathrm{proj}}/(\pi^+/\pi^-)^{\mathrm{pp}}_{\mathrm{incl}}$ ratio is presented in Fig. 7.17.

There is stronger increase of the charge ratio in the projectile feed-over region than

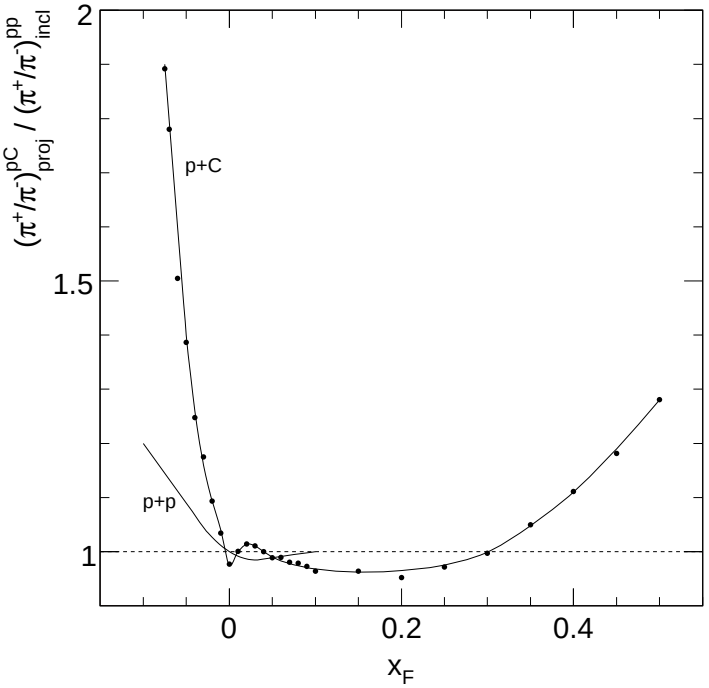

Figure 7.17: Charge ratio of the projectile component in p+C divided by the inclusive ratio in p+p collisions

in elementary collisions also shown in Fig. 7.17 for comparison. In the forward region for x_F between 0.1 and 0.25 the ratio decreases with about 4% followed by increase above $x_F = 0.3$. This shape of the ratio shows that there is a charge correlation between the far forward and feed-over region of the projectile fragmentation. Due to the small contribution in absolute yields from these areas, the decrease of the charge ratio in the intermediate region is imposed by the charge conservation in view of the increased projectile multiplicity.

7.5 Intranuclear cascading

Up to now the discussion was concentrated in the projectile and target components. In proton-nucleus collisions there is a third component, called intranuclear cascading, which is due to the propagation and interaction of the participating nucleons and fragmentation products inside the nucleus. The cascading products will have typically small momentum in the rest frame of the target, i.e. the laboratory frame. For pions low $p_{\rm lab}$ correspond to $x_F \sim$ -0.15, as expected from mass ratio m_π/m_p. The kinematic situation for pions in (x_F,p_T) plane is depicted in Fig. 7.18 where with lines are indicated the constant total momentum $p_{\rm lab}$ and constant polar angle $\Theta_{\rm lab}$ in the laboratory frame. The intranuclear cascading can contribute in the forward region only if the pion lab momentum is large.

The hatched area in central and forward region in Fig. 7.18 represents the cov-

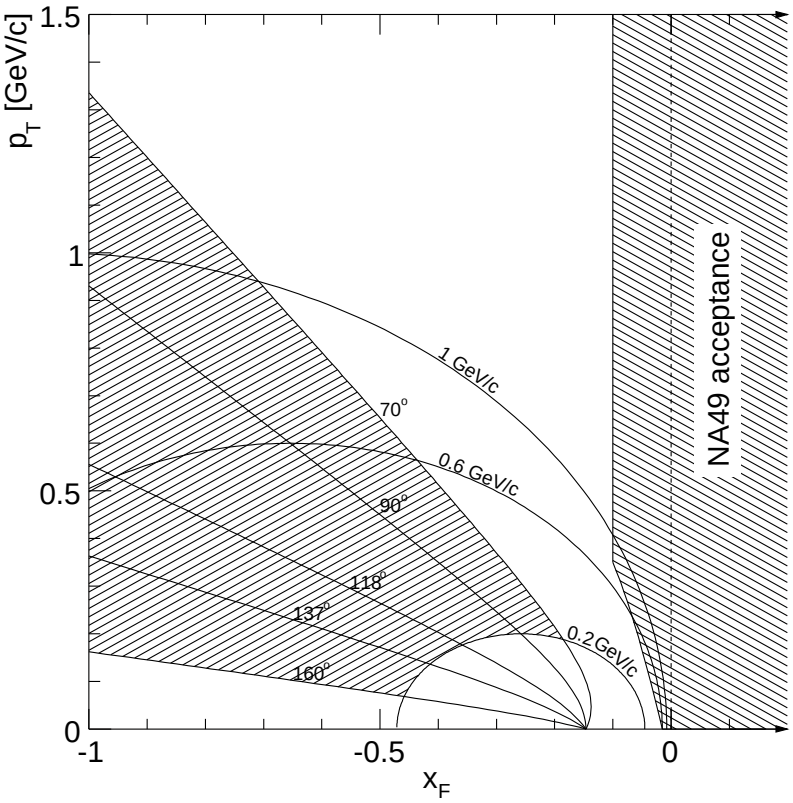

Figure 7.18: Kinematics in the backward region. With lines are indicated the constant total momentum $p_{\rm lab}$ (0.2, 0.6 and 1 GeV/c) and constant polar angle $\Theta_{\rm lab}$ (70°, 90°, 118°, 137°, 160°). The shaded areas represent the coverage of [36] (far backward region) and NA49 (central and forward region)

ered phase space by NA49. The acceptance limit of NA49 experiment corresponds to $p_{\rm lab} \sim 0.6$ GeV/c. At this momentum the intranuclear pion production yield is strongly reduced and a very small if any cascading contribution can be expected. This contribution can be quantified using measurement by Nikiforov et. al. [36]. This experiment at Fermilab at 400 GeV/c beam momentum covers the backward region as indicated with the second hatch area in Fig. 7.18, see also Fig. 1.2a. The measurement has been performed at fixed lab angle $\Theta_{\rm lab}$ between 70 and 160 degrees, leaving a small uncovered region with respect to the NA49 acceptance.

In order to quantify the cascading contribution the cross sections obtained in [36] are related to the isospin average prediction for the target fragmentation developed in Sect. 7.3. This is possible since no contribution from projectile hadronization can be expected in covered region. The data of [36] were corrected for the feed-down of week decays. The feed-down correction has been applied following the methodology developed for the NA49 data, see Sect. 4.4.6. With corrected in this way cross section the following ratio is formed:

$$R_{\rm casc} = \frac{(Ed^3\sigma/dp^3)_{\rm Nikiforov}}{(Ed^3\sigma/dp^3)_{\rm pC}} \tag{7.13}$$

The $R_{\rm casc}$ is plotted in Fig. 7.19 for the five measured angles as a function of the p_T.

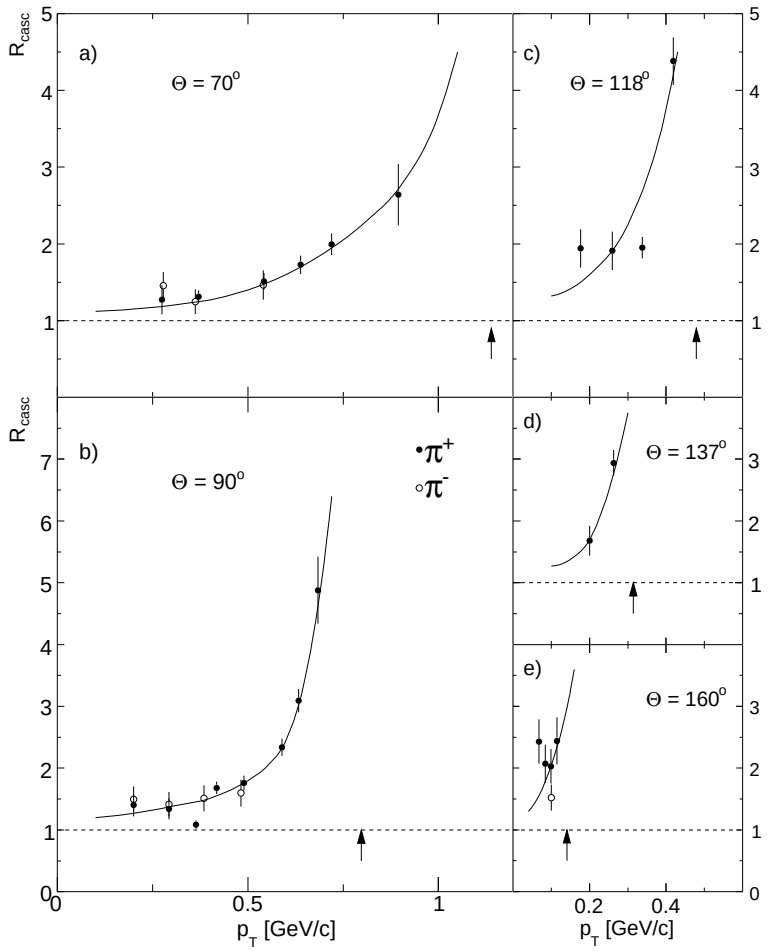

Figure 7.19: $R_{\rm casc}$ for different fixed lab angles $\Theta_{\rm lab}$ measured by [36]. The arrows indicate the p_T value at which x_F of -0.85 is reached

It increases strongly with p_T for all angles. This is due to the increase of $|x_F|$ along the lines of constant $\Theta_{\rm lab}$ which is accompanied with increasing domination of the cascading products in the far backward hemisphere. In fact the cascading products are found at $x_F <$ -1 which is not accessible for the target fragmentation and therefore the ratio $R_{\rm casc}$ tends to diverge at this limit. The arrows given in Fig. 7.19 indicate the p_T value at each angle where $x_F =$ -0.85 is reached.

The p_T dependence at fixed $\Theta_{\rm lab}$ can be transformed into a x_F dependence at fixed p_T. The result is shown in Fig. 7.20.

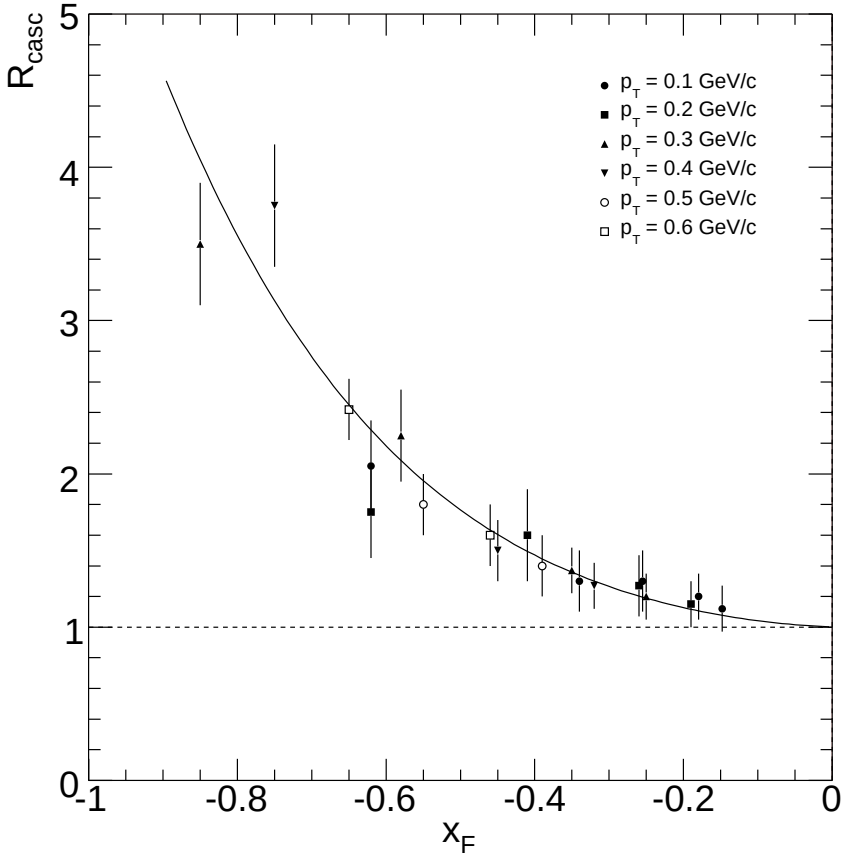

Figure 7.20: $R_{\rm casc}$ obtained from [36] as a function of x_F

Within the errors of the data points, the x_F dependence can be parametrized with a single curve, independent of p_T, which converges to $R_{\rm casc} = 1$ at $x_F = 0$. This convergence is also justified by the fact that relatively large momentum $p_{\rm lab}$ is needed to approach $x_F = 0$, see Fig. 7.18. As the ratio $R_{\rm casc}$ gives the excess of the cascading production with respect to the target fragmentation, it may be argued that contribution from cascading at $x_F =$ -0.1 is on the level of few percent only. The fact that acceptance of the NA49 detector at this x_F is limited to $p_T = 0.4$ GeV/c further reduces the possible contribution to the NA49 data. The extrapolation into unmeasured region performed in Sect. 7.4, which takes into account only target contribution, is justified in this way. It has to be mentioned that in the region $x_F <$ -0.1 and $p_T < 0.2$ GeV/c the π^+/π^- ratio will be effected by the final-state Coulomb interaction with the spectator nucleons in the nucleus [66–69]. However this effect is expected to be small for the Carbon nucleus.

The two-component picture developed in preceding section takes into account only target and projectile contribution. The prediction in Sect. 7.3 now has to be completed

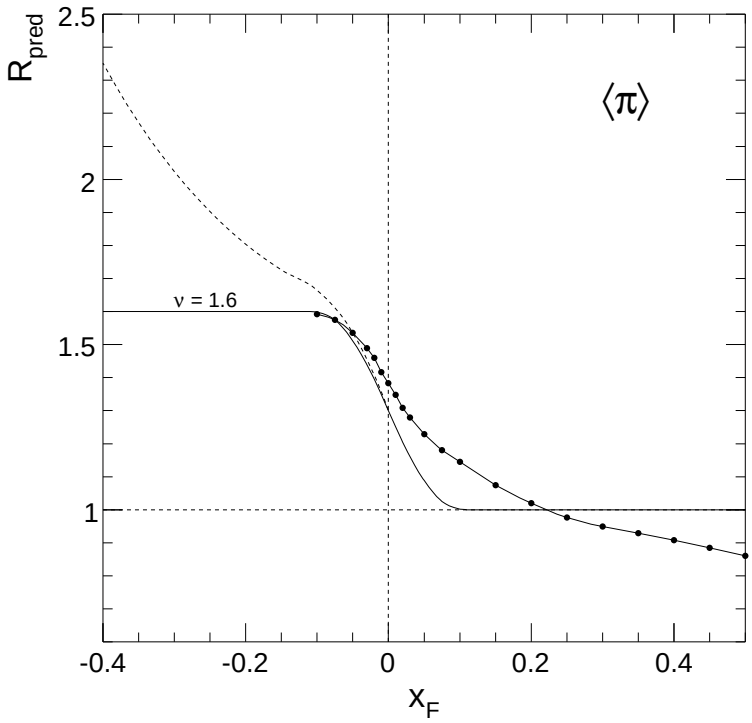

Figure 7.21: $R_{\rm pred}$ as a function of x_F, giving the data points together with the target contribution at $\langle\nu\rangle = 1.6$ (full line) and adding the intranuclear cascading part (broken line)

with cascading contribution as quantified in Fig. 7.20. The result for the charge-averaged pion is shown in Fig. 7.21. Here the intranuclear cascading contribution is added to presented in Fig. 7.4.1 predicted yield from target and projectile fragmentation for mean number of collisions $\langle\nu\rangle = 1.6$. The overall ratio $R_{\rm pred}$ exhibits a smooth increase from far forward to far backward region of x_F. This is in agreement with pseudo-rapidity η ratio

$$R(\eta) = \frac{(dn/d\eta)^{\rm pA}(\eta)}{(dn/d\eta)^{\rm pN}\eta} \tag{7.14}$$

observed in emulsion measurement [70] at 200 and 800 GeV/c beam momentum, where almost linear increase of $R(\eta)$ is found, from values below 1 in forward rapidity to values in excess of 2 in the far backward hemisphere.

Chapter 8

Transverse dependence

The p_T dependence will be studied in this chapter in terms of double inclusive cross section $f(x_F, p_T)$, defined with Eq. 4.5.

8.1 Cross section ratio with respect to elementary collisions

The presence of the Carbon nucleus and the corresponding two-component hadronization mechanism suggest that the straight-forward cross section ratio

$$R(x_F, p_T) = \frac{f^{\mathrm{pC}}(x_F, p_T)}{f^{\mathrm{pp}}(x_F, p_T)} \tag{8.1}$$

is probably not the best choice for comparison of p+C with elementary p+p collisions in the full x_F scale. There are two important and well quantified overall phenomena which should be taken out in this comparison:

- The target pile-up corresponds to $\langle\nu\rangle$ participating nucleons which will results in overall upward shift of $R(x_F, p_T)$ in the region below $x_F = 0.1$ depending on the relative target contribution.
- Due to the isoscalar nature of the Carbon nucleus the π^+ and π^- yields from the target contribution are equal which is not the case for the projectile fragmentation.

In order to characterize the projectile-connected p_T dependence a definition of the cross section ratio that takes direct reference to the two-component superposition, has been chosen:

$$R_{p_T}(x_F, p_T) = \frac{f^{\mathrm{pC}}(x_F, p_T)}{f_{\text{two-comp}}(x_F, p_T)} \tag{8.2}$$

where $f_{\text{two-comp}}(x_F, p_T)$ is defined as:

$$f_{\text{two-comp}}(x_F, p_T) = t(x_F)\left(\frac{1}{2}f^{\mathrm{pp}}_{\pi^+}(x_F, p_T) + \frac{1}{2}f^{\mathrm{pp}}_{\pi^-}(x_F, p_T)\right) + p(x_F)f^{\mathrm{pp}}(x_F, p_T), \tag{8.3}$$

with $f^{\mathrm{pp}}(x_F, p_T)$ denoting the double differential pion cross section in p+p interactions and R_{p_T}, f^{pC}, $f_{\text{two-comp}}$ and f^{pp} to be regarded separately for π^+ and π^- mesons. The functions $t(x_F)$ and $p(x_F)$ describe the relative contribution from target and projectile fragmentation to the total pion yield in the two-component picture, as presented in Fig. 8.1.

These functions fulfill the following conditions:

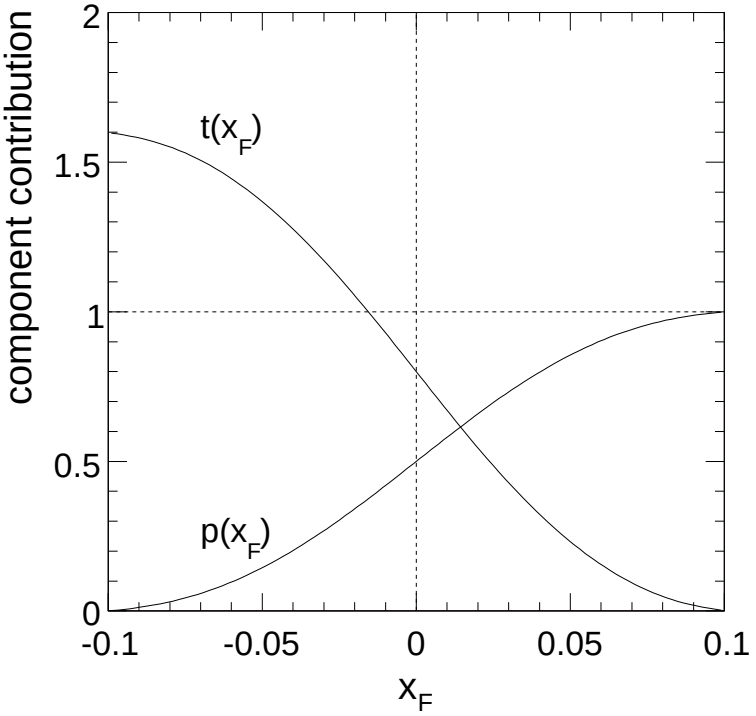

Figure 8.1: Target $t(x_F)$ and projectile $p(x_F)$ contributions to the pion yield in the two-component picture, with $t(x_F) = 1.6p(-x_F)$

- $t(x_F)$ ensures that target contribution amounts to $\langle\nu\rangle$ times average pion yield at x_F = -0.1 and vanishes at $x_F = 0.1$.
- $p(x_F)$ is 1 above $x_F = 0.1$ and determines the total pion yield in this region and reaches 0 at x_F = -0.1.

Therefore the constructed in this way ratio R_{p_T} contains the features of the superposition of elementary components in p+C collisions and addresses specifically the modifications due to the projectile fragmentation. This ratio is shown in Fig. 8.2 for three x_F values for both π^+ and π^-. The full lines represent the ratio R_{p_T} resulting from the interpolation developed in Sect. 5.1. As expected, complex p_T and x_F dependence emerge. The arrows indicate the mean transverse momentum $\langle p_T\rangle$. The p_T range around this value governs the p_T integrated yield and it reproduces the features of this quantity with respect to elementary collisions as elaborated above, namely the ratio is bigger than 1 below $x_F = 0.2$, crosses 1 around this value and further decreases below 1 for larger x_F values.

A second region of interest is the behaviour at high p_T values. A significant increase of R_{p_T} at high p_T with respect to the $\langle p_T\rangle$ is observed for the full x_F scale as can be seen from Fig. 8.3, where the overview of R_{p_T} for the entire covered x_F range is presented.

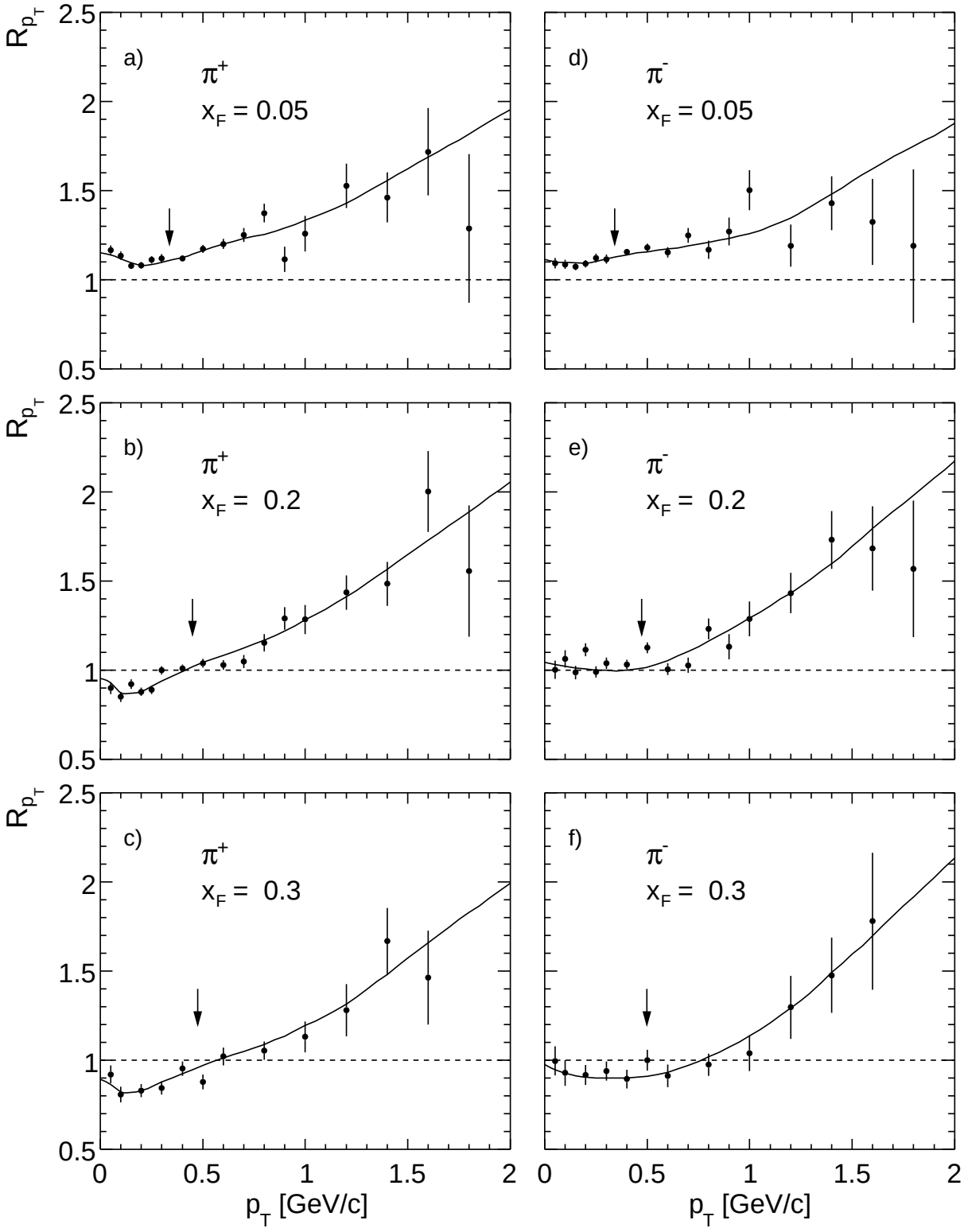

Figure 8.2: Ratio R_{p_T} as a function of p_T at three x_F values for a),b) and c) π^+, and d),e) and f) π^-. The arrows indicate $\langle p_T \rangle$ for given x_F

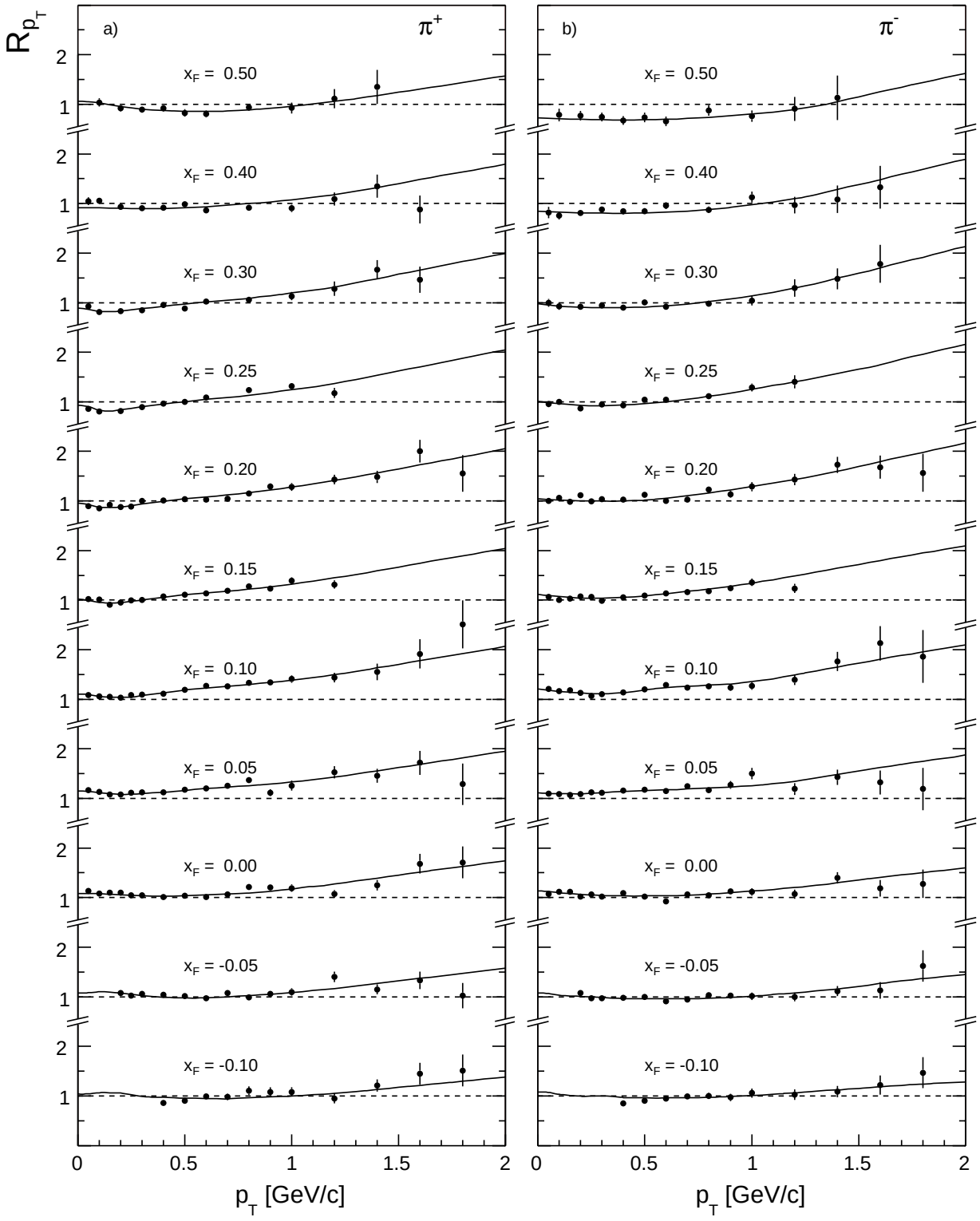

Figure 8.3: Ratio R_{pT} as a function of p_T at fixed x_F for a) π^+ and b) π^-

8.2 Definition of p_T enhancement

As was mentioned in the previous section the ratio R_{p_T} shows an increase at high p_T with respect to the $\langle p_T \rangle$ for each x_F, see Fig. 8.3. This increase can be quantified by introducing the measured enhancement factor $E^m_{p_T}(p_T)$:

$$E^m_{p_T}(p_T, x_F) = \frac{R_{p_T}(p_T, x_F)}{R_{p_T}(\langle p_T \rangle, x_F)}. \tag{8.4}$$

This definition relates the ratio R_{p_T} at any p_T to its value at mean transverse momentum for fixed x_F and the chosen reference quantity $R_{p_T}(\langle p_T \rangle)$ has the behaviour of the p_T integrated observables and the detailed structures present at low p_T (see Sect.5.2) averaged out in the reference. The x_F dependence of $E^m_{p_T}$ is shown in Fig. 8.4 for four p_T values extending up to the experimental limit of 1.8 GeV/c.

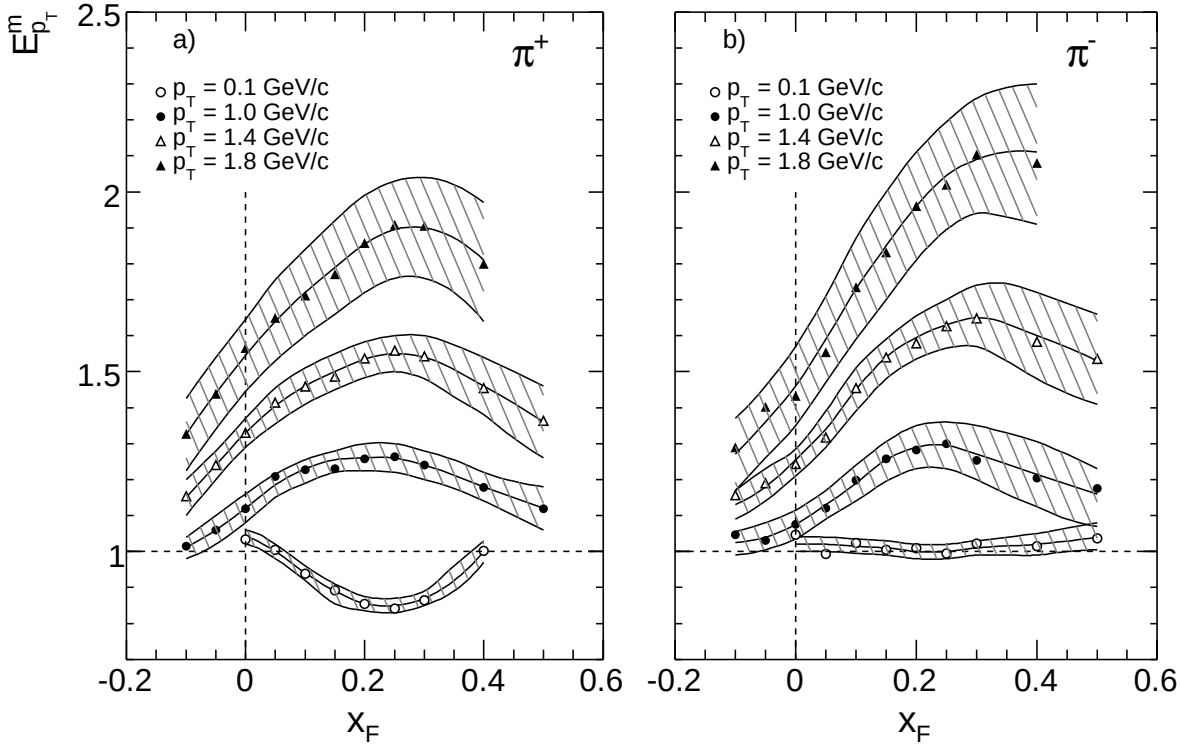

Figure 8.4: The p_T enhancement as a function of x_F at several fixed p_T values for a) π^+ and b) π^-. The shaded regions mark the error margins connected to the interpolation scheme developed in Sect. 5.2

The shaded areas in Fig. 8.4 correspond to the error margins connected with the interpolation procedure. The enhancement factors $E^m_{p_T}$ increase from values close to unity at low p_T to about 2 at $p_T = 1.8$ GeV/c. The detailed x_F dependence of $E^m_{p_T}$ is different for π^+ and π^- especially at low p_T. Nevertheless some common features are observed, namely at p_T above the mean, the enhancement factor increases from the acceptance limit at x_F = -0.1 through $x_F = 0$ towards forward hemisphere. It reaches maximum at about $x_F = 0.2 \div 0.3$ and this maximum has larger values and it moves more forward for the higher p_T. The $E^m_{p_T}$ decreases in very forward region and tends to 1 due to the vanishing contribution from multiple collisions.

8.3 High p_T phenomena

In the connection with the forthcoming discussion the term "high p_T" needs some clarification.

In a first instance, it seems to be generally accepted that hadron production in the region of $p_T \sim 2$ GeV/c is already govern by the hard parton-parton scattering. This expectation was developed in connection with ISR data [71, 72] and is still widely used in the interpretation of very recent RICH results [73, 74].

In the second instance, the early discovery of an "anomalous" p_T enhancement in proton-nucleus collisions, so-called Cronin effect [25], in a corresponding region of transverse momentum, seems to point into the same direction. In fact the only attempt at understanding of the Cronin effect is based on multiple partonic scattering [75–79] which can not be confirmed with the available experimental information.

Here the notion "high p_T" will be used to mark the measurement limit of 1.8 GeV/c in the transverse momentum of NA49 experiment in p+C interaction.

8.3.1 Anomalous nuclear enhancement

The anomalous nuclear enhancement was first quantified via A-dependence of the hadronic cross section, parametrized as:

$$\sigma^{\mathrm{pA}} \sim A^{\alpha(p_T)} \sigma^{\mathrm{pp}} \tag{8.5}$$

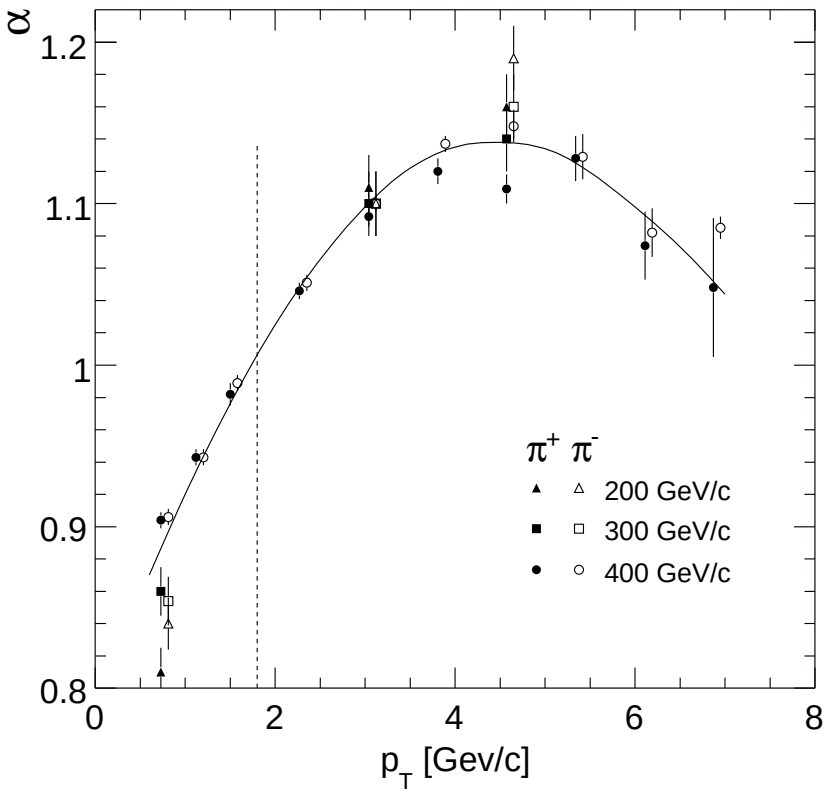

Figure 8.5: The exponent α as a function of p_T for π^+ and π^- at three different beam momentum measured by [25]. The corresponding x_F range for each energy is given. The dashed line corresponds to p_T limit of the NA49 data

The dependence of the parameter α on transverse momentum is shown in Fig. 8.5 for π^+ and π^- at beam momentum of 200, 300 and 400 GeV/c. The exponent $\alpha(p_T)$ shows steep increase between 0.8 and 0.9 at low transverse momentum to a maximum of about 1.15 at $p_T \sim 4$ GeV/c, followed by decrease up to measurement limit. The scarce data and the sizable errors at 200 and 300 GeV/c do not exclude s-dependence. There is a difference between π^+ and π^-, as α is slightly larger for negative than for positive pions. The NA49 measurement limit, indicated in Fig 8.5 with dashed line, is in the half way between the low p_T and saturation value of α. By chance at p_T =1.8 GeV/c α is close to 1 which is believed to be characteristic of hard scattering [25].

The pion cross section measured by [25] in proton interactions with Be, Ti and W nucleus may be interpolated to Carbon and hence compared to the NA49 results. This comparison as a function of p_T at $x_F = 0$ for average pion $\langle\pi\rangle$ is presented in Fig. 8.6.

At 200 GeV/c beam momentum, which is in the immediate vicinity of the NA49 energy range, there is only one point to be compared directly. The good consistency with the largest data sample at 400 GeV/c beam momentum is rather unexpected due to the strong non-scaling behaviour of the s-dependence at this p_T range. It has to be recalled that data of [25] are obtained at fixed lab angle of 77 mrad which leads to an s-dependent spread of the corresponding x_F values between -0.05 and +0.15. In view of the strong x_F dependence of the pion cross section in the neighbourhood of $x_F = 0$ the small difference in this variable results in non-negligible systematic deviations at the level of precision of the present study. Including however the quoted by [25] normalization uncertainties of

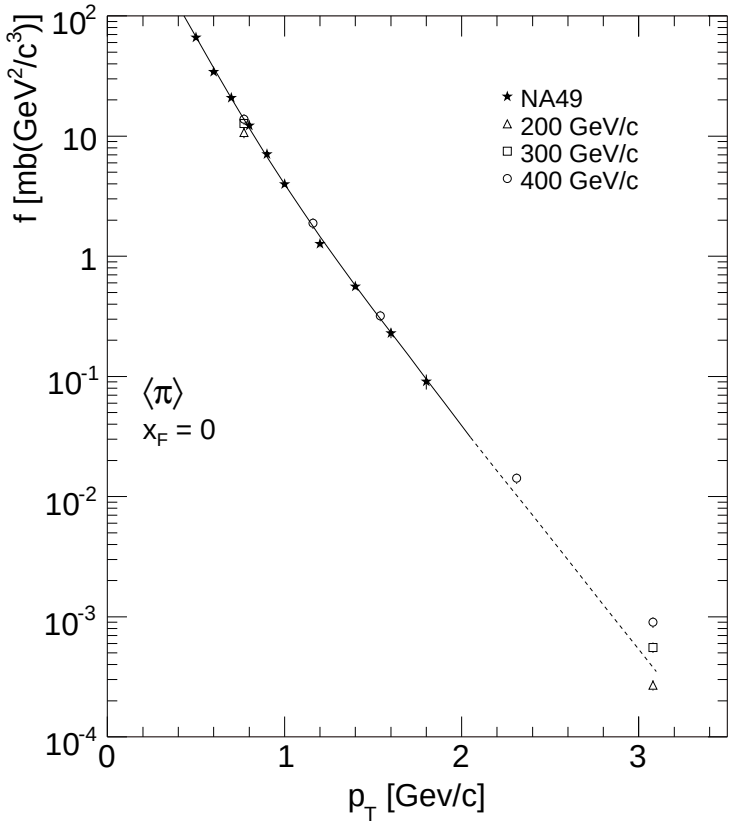

Figure 8.6: Comparison of the cross section for $\langle\pi\rangle$ as a function of p_T at $x_F = 0$ measured by [25] and interpolated to Carbon with p+C results from NA49

20% and the sizeable statistical errors, the consistency of the data may be considered as satisfactory.

8.3.2 High p_T enhancement

The NA49 measurement spans a large x_F range and it may be claimed that it permit systematic study of x_F dependence of Cronin effect, as data [25] cover only small central region.

Inspection of Fig. 8.4 shows that in central region does not take a special role, as the enhancement rises smoothly through $x_F = 0$ and reaches a maximum at about $x_F = 0.3$. Another important feature of the enhancement is that in tends to unity in both directions, $x_F <$ -0.1 and $x_F > 0.4$.

The approach to unity in the backward region is indeed expected where the projectile component vanishes with respect to the target contribution. In the two-component picture the participant target nucleons should not show anomalous behaviour at high p_T and the target enhancement $E_{p_T}^{\text{target}}$ must be equal to one over the full x_F range.

In the far forward region the pion yield from multiple collisions is progressively suppressed and the contribution from single collisions grow as x_F approaches 1. As $E_{p_T}^{m}$ from single collision is one, the enhancement will tends to unity at large x_F.

8.3.3 Enhancement of the projectile component

In the framework of the two-component picture the high p_T enhancement can be addressed to the multiple collisions of the projectile. The enhancement of the projectile component can be extracted by writing down the measured enhancement as composition of the target $E_{p_T}^{\text{target}}$ and projectile $E_{p_T}^{\text{proj}}$ components:

$$E_{p_T}^{m} = \frac{t(x_F)E_{p_T}^{\text{target}} + r_{\text{proj}}E_{p_T}^{\text{proj}}}{t(x_F) + r_{\text{proj}}} \tag{8.6}$$

where $r_{\text{proj}} = (dn/dx_F)_{\text{proj}}^{\text{pC}}(\langle p_T\rangle)/(dn/dx_F)^{\text{pp}}(\langle p_T\rangle)$. Here $t(x_F)$ denotes the relative target contribution as a function of x_F. The range of target-projectile feed-over at high p_T is larger than at low transverse momentum and it reaches $x_F \sim \pm 0.3$. The p_T enhancement at $p_T = 1.8$ GeV/c is shown in Fig. 8.7a, where the smooth extrapolation out of the measured range is indicated with dashed lines. Function $t(x_F)$ together with the relative projectile contribution $p(x_F)$ are presented in Fig. 8.7b. The shapes are constructed by the boundary conditions $p(-0.3) = t(0.3) = 0$, $p(x_F > 0.3) = 1$ and $t(x_F < -0.3) = \langle\nu\rangle$, and the symmetry conditions $p(0) = 0.5$ and $t(0) = \langle\nu\rangle/2$. Taking into account that target enhancement factor $E_{p_T}^{\text{target}} = 1$ the enhancement of the projectile component can be written from Eq. 8.6 as:

$$E_{p_T}^{\text{proj}} = \frac{1}{r_{\text{proj}}}\left(E_{p_T}^{m}(t(x_F) + r_{\text{proj}}) - t(x_F)\right) \tag{8.7}$$

The x_F dependence of $E_{p_T}^{\text{proj}}$ is shown in Fig. 8.8. As an important consequence of this decomposition is that measured enhancement at $x_F = 0$ is not fully representative of this phenomenon. It is substantially increased by taking out the "inert" target component in p+A interactions. This is very important for understanding of nuclear enhancement in the symmetric A+A collisions, where the target and projectile equally contribute. From this consideration alone must be expected that measured nuclear enhancement in A+A

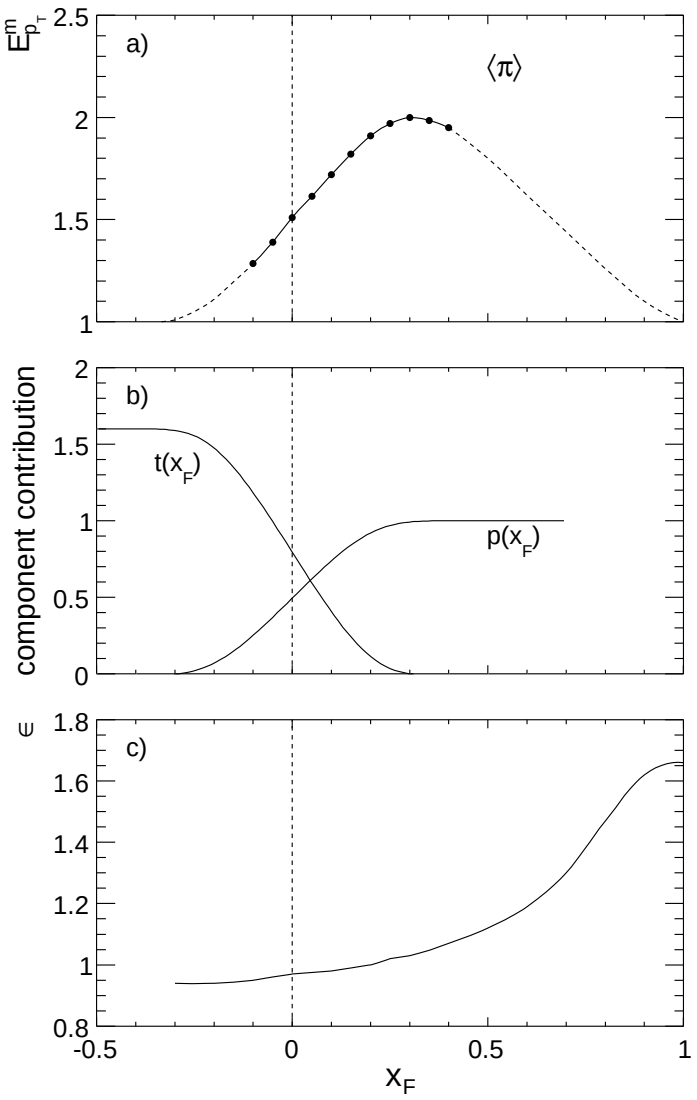

Figure 8.7: a) The enhancement factor $E^m_{p_T}$ as a function of x_F, b) target and projectile contributions as a function of x_F at $p_T = 1.8$ GeV/c, and c) efficiency function ϵ multiplying the relative contribution from single collisions as a function of x_F

collisions must be bigger than in p+A collisions. If however the projectile component is properly extracted the enhancement should tend to be equal at equal mean number of collisions $\langle\nu\rangle$ per projectile participant, unless new physics phenomena are present in A+A interactions.

8.3.4 Enhancement of the projectile component from multiple collisions

The large probability of single collision $P(1)$ in minimum bias p+C interactions, which is about 0.6, gives a strong influence on the measured p_T enhancement, as enhancement from such interactions should be equal to one. This influence with x_F can be described by a multiplicative weight function $\epsilon(x_F)$ which is shown in Fig. 8.7c. This function approaches value of $1.6 \sim 1/P(1)$ for $x_F \to 1$ and reduces to ~ 0.9 in the backward region. Using this function the enhancement of the projectile component from multiple collisions can be expressed as:

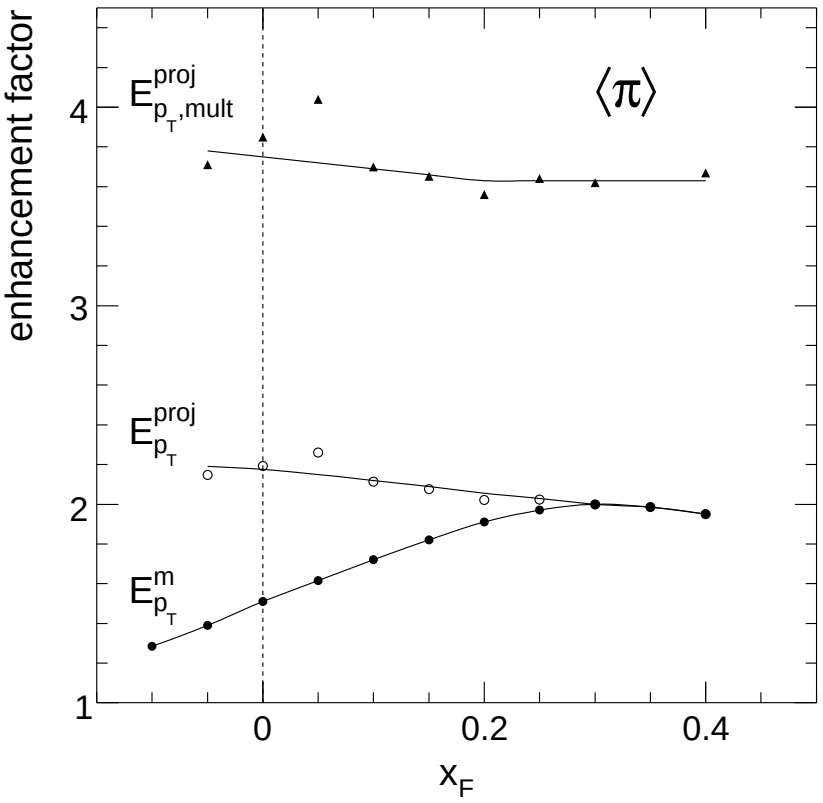

Figure 8.8: The enhancement factors E^m_{pT}, $E^{\rm proj}_{p_T}$, $E^{\rm proj}_{p_T,\nu\geq 2}$ as a function of x_F at $p_T = 1.8$ GeV/c

$$E^{\rm proj}_{p_T,{\rm mult}} = \frac{E^{\rm proj}_{p_T}(x_F) - P(1)\epsilon(x_F)}{1 - P(1)\epsilon(x_F)} \tag{8.8}$$

The application of Eq. 8.8 results in a further increase of the p_T enhancement over the full x_F range, as can be seen from Fig. 8.8.

8.4 A look into resonance decay

The production and decay of resonances plays a very important role in soft hadronic processes. Here only some basic mechanisms which are of straight-forward kinematic origin will be discussed.

8.4.1 Inclusive pion production from ρ and Δ^{++} decays

In Sect. 5.2 was pointed out that local structures have emerged in all inclusive distributions, in the x_F as well as in the p_T dependences. These structures are significantly different for π^+ and π^- and they are more pronounced in p+p than in p+C interactions. Similar structures have been first observed at CERN PS in 1974 [80] and discussed in relation to resonance decay. In fact, by using measured inclusive cross section for the low-mass mesonic and baryonic resonances ρ and Δ^{++} such structures are readily predicted if the mass distribution of these resonances is properly taken into account. The known charge dependence of mesonic and baryonic resonance production in p+p collisions reflects to a distinct difference between π^+ and π^- as observed in the data. An example

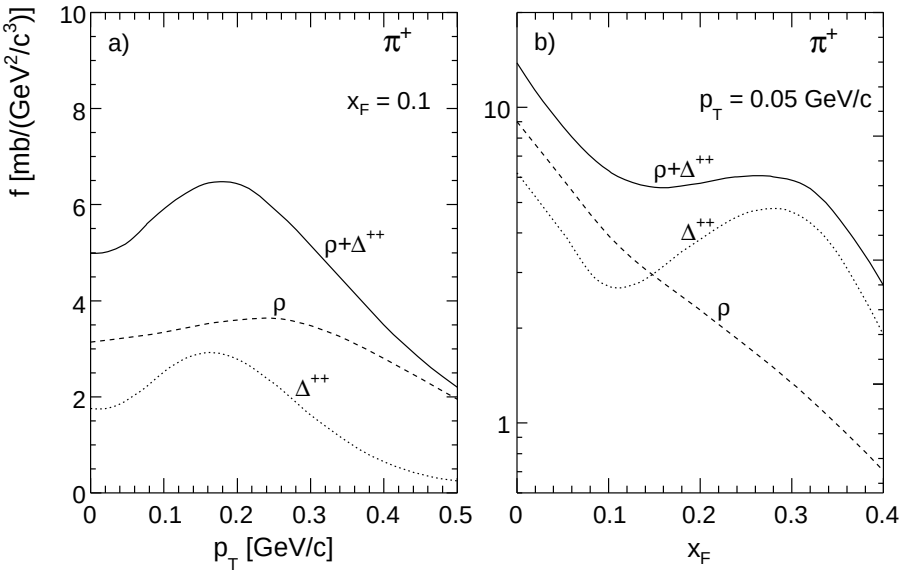

Figure 8.9: Monte Carlo study of a) p_T distribution at $x_F = 0.1$ and b) x_F distribution at $p_T = 0.05$ GeV/c for π^+ resulting from ρ and Δ^{++} in p+p interactions

of p_T dependence at fixed x_F and x_F dependence at fixed p_T of pions produced from ρ and Δ^{++} decay are presented in Fig. 8.9, showing that the salient features of the data are predicted already from very restricted set of resonances.

8.4.2 Two-component picture in connection to Δ^{++} decay

The Δ^{++} resonance has well enough determined x_F and p_T inclusive distributions [29, 81] for the current purposes. The p_T integrated x_F distribution of Δ^{++} is presented in Fig. 8.10 where also the constructed projectile and target components are shown.

The decay proceeds via a channel $\Delta^{++} \rightarrow \mathrm{p} + \pi^+$. The p_T integrated x_F distribution

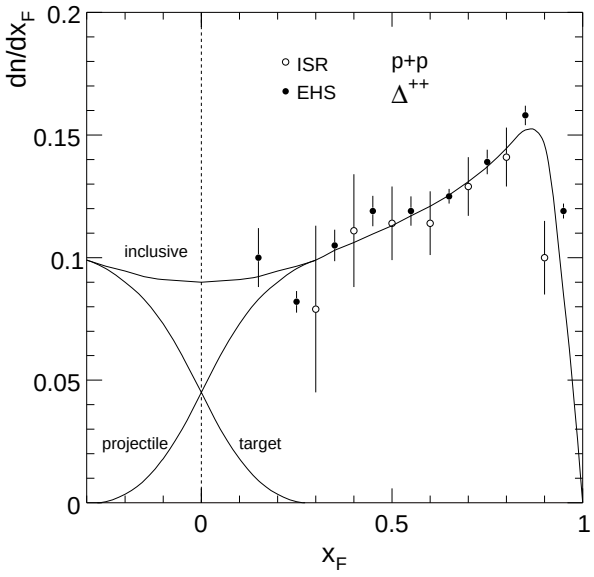

Figure 8.10: Two-component picture for Δ^{++}

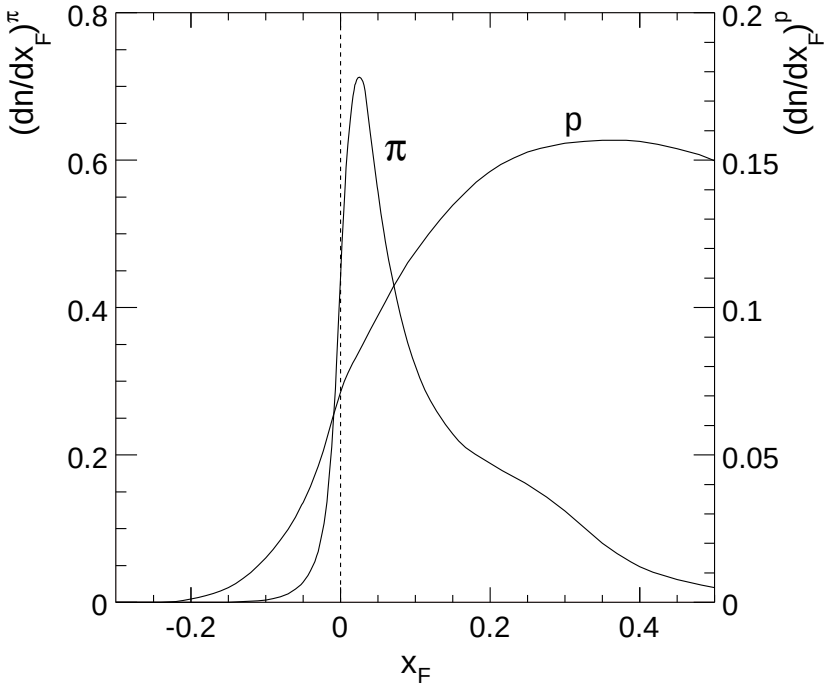

Figure 8.11: p_T integrated x_F distributions of protons and pions produced from Δ^{++} decay

of the projectile component of the decay products is shown in Fig. 8.11.

A first observation is that overall shape of the distribution is very similar to the inclusive one Fig. 7.4, although there are deviations in detail, as can be expected from the single low-mass resonance. This similarity especially concerns the pion feed-over into the target hemisphere.

A second observation concerns the difference of the feed-over between pion and proton. This difference has been already mentioned in Sect. 7.1.5, see Fig. 7.7.

This effect is connected to the mass dependence and is straight-forward consequence of the Lorentz transformation between the resonance rest frame and cms of the collision. The energy factor of this transformation is:

$$E = \sqrt{m_{\rm sec}^2 + q^2} \tag{8.9}$$

where $m_{\rm sec}$ is the decay particle mass and q is given by

$$q = \frac{1}{2m_{\rm res}}\sqrt{(m_{\rm res}^2 - (m_\pi + m_p)^2)(m_{\rm res}^2 - (m_\pi - m_p)^2)}. \tag{8.10}$$

At the nominal Δ^{++} mass q is equal to 0.229 GeV/c which much less than the proton mass. Therefore, in contrast to the pion, the proton receives a major fraction of the resonance momentum in the cms of the interaction.

A third observation is connected to p_T dependence of pions produced via Δ^{++} decays. The x_F distributions at several fixed p_T value are shown in Fig. 8.12 which distributions are obtained by studying Δ^{++} decay in bins of transverse momentum. The distributions are normalized to unity at $x_F = 0$ in order to calibrate the strong p_T dependence of the cross section. Clearly there is a steady increase of the feed-over range with increasing of the transverse momentum. At the upper p_T limit of the NA49 data of 1.8 GeV/c the shape of the pion feed-over approaches the one measured for the proton.

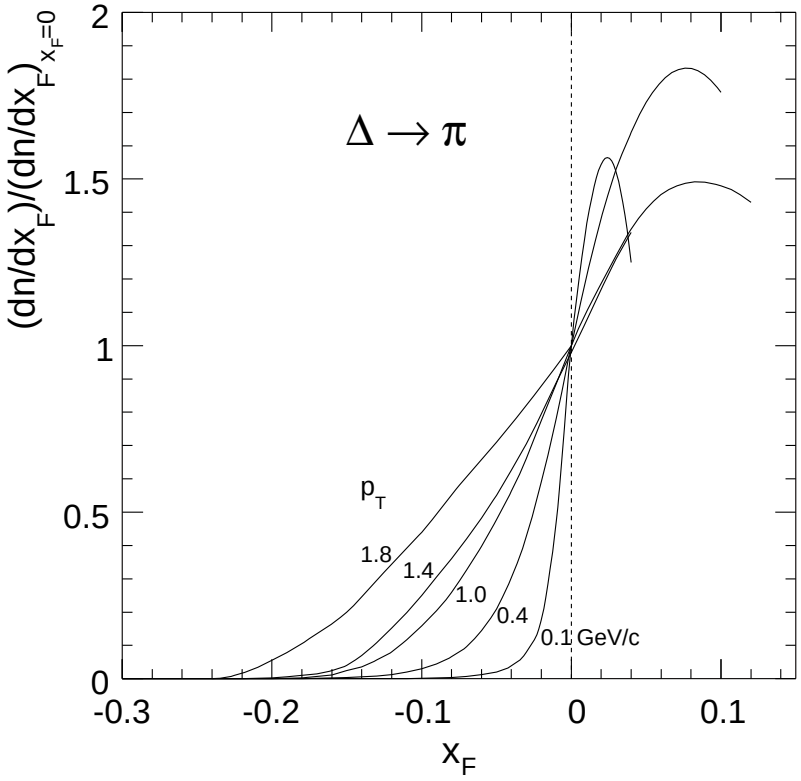

Figure 8.12: Pion feed-over from Δ^{++} decay for different values of p_T

This third observation follows again the resonance kinematics. Low mass secondaries with large transverse momentum are produced when the resonance mass is in the tail of the Breit-Wigner distribution, as in the case of $\Delta(1232)$ these are values well above 2 GeV/c^2. Correspondingly the decay momentum q (Eq. 8.10) of the decay is in the order of 1 GeV/c which in turn reduces the mass dependence(Eq. 8.9) and increases the feed-over range. It is therefore mandatory to take proper into account the resonance mass distribution. This shows that resonance decay is very important source of "high p_T" particles. In fact by using a sum of 13 measured resonances it has been demonstrated for p+p collisions [82] that inclusive pion distribution from two body decays saturate yields up to $p_T = 3$ GeV/c and beyond over the full x_F range. A modification of the resonance spectrum towards higher masses in multiple collisions would be sufficient to also describe the anomalous nuclear enhancement in this p_T range, at SPS energies, without invoking partonic or perturbative effects.

Chapter 9

Summary

The NA49 experiment is built for investigation of the hadronic interactions, ranging from elementary hadron-proton through hadron-nucleus to nucleus-nucleus interactions. It features large acceptance and particle identification via specific energy loss measurement. This combined with the large statistical samples for different reactions allows for model independent study of the hardon production. In this thesis the inclusive pion production in p+p and minimum bias p+C collisions at 158 GeV/c beam momentum is presented.

The results come from samples of 4.8 million events in p+p collisions and 377 000 events in p+C collisions. The data cover range of $0 < p_T < 2$ GeV/c and $0 < x_F < 0.85$ in p+p interactions, and $0 < p_T < 1.8$ GeV/c and $-0.1 < x_F < 0.5$ in p+C interactions. Systematic and statistical uncertainties in p+p collisions are well below 5%, as in p+C collisions statistical uncertainties are on the level of few percent and systematic errors are less than 8%. The high precision of the data allows for the first time to observe local structures in the data. These structures are more pronounced in p+p collisions than in p+C collisions and are more expressed for π^+ than for π^-. They are present in both x_F and p_T distributions in this way not allowing a simple analytic parametrization. The existence of the structures is a direct manifestation of resonance decays.

The above mentioned local structures are also present in the y distributions. The high precision of the data shows that m_T distribution at $y = 0$ can not be described with constant inverse slope T which contradicts the expectation for particle emission from a thermal source.

The p_T integrated quantities, like invariant and non-invariant yields as a function of x_F, first and second moments of the p_T distributions have been obtained. The first and second moments increase in p+C collisions compare to p+p interactions.

An extensive comparison of the NA49 results with the existing data has been made. The p+p data show a very good agreement with measurements from [21], concerning the double differential cross section, while large systematic deviations (up to 4σ) have been found in comparison with [20]. In p+C case also an average deviation of 25% (3.6σ) between NA49 and [35] results have been found. In two later cases the discrepancy is not present in π^+/π^- ratio which indicate normalization problems in the old measurements. Although the good agreement between NA49 and [21] results for the differential data, a large discrepancies (up to 5σ) are observed concerning the p_T integrated yields. These discrepancies can be attributed to the limited p_T coverage of the [21] which requires extrapolation in order to integrate. This again shows that the simple Gaussian or exponential parametrization, as used by [21], do not describe well the p_T distributions.

The measurement of the trigger cross section and estimation of the trigger losses and elastic contribution allow to derive the total inelastic cross section σ_{inel}. The obtained

results, $\sigma_{\rm inel}^{\rm pp} = 31.46$ mb and $\sigma_{\rm inel}^{\rm pC} = 226.3$ mb, in both reactions p+p and p+C are in very good agreement with the existing measurements.

The detailed study of the p_T integrated distributions as well as the p_T dependences in the p+C collisions in relation to p+p interactions leads to the number of conclusions:

- It is clearly established that p+p reaction is composition of two independent components: projectile fragmentation and target fragmentation.
- In addition to these two components there a third component in p+C collisions, intranuclear cascading, generated by the propagation and interaction of the participating nucleons and secondary hadrons inside the nucleus.
- In both reaction the components have been isolated and quantified.
- Intranuclear cascading governs the far backward region and decreases towards $x_F = 0$. Its contribution at x_F = -0.1 is at the level of only few percent to the total pion yield.
- The target and projectile components overlap in a limited range around $x_F = 0$. The extent of this range depends on particle type (its mass) and transverse momentum. It is limited to $|x_F| = 0.1$ for the p_T integrated pion yield and to $|x_F| = 0.25$ for $p_T = 1.8$ GeV/c.
- Due to the forward-backward symmetry in the p+p case the target component at given x_F has to be equal to projectile component at reflected with respect to 0 x_F value, i.e. $t(x_F) = p(-x_F)$.
- The total pion yield from target component in p+C collisions corresponds on average to 1.6 participant target nucleons which is significantly below (4σ) the expectation from measured nuclear parameters. Target fragmentation in this case reveals a detailed charge dependence, reflecting the isospin composition of the carbon nucleus.
- The π^+/π^- ratio approaches 1 at x_F = -0.1 which is expected for isoscalar Carbon nucleus. This approach is not smooth but a local maximum appears at $x_F \sim$ -0.04. A similar maximum has been observed in the forward region in $\langle\pi\rangle$+p reaction. This structure indicates slight but significant difference in the feed-over shape for π^+ and π^-.
- The projectile interacts on average $\langle\nu\rangle$ inside the nucleus which leads to deviation in practically all measured quantities in comparison to elementary collisions.
- The total projectile pion yield in p+C reaction increases by about 10% in comparison to p+p collisions. This increase is concentrated around $x_F = 0$.
- Above $x_F \sim 0.2$ pion yield in p+C interactions decreases steadily with respect to elementary collisions. This decrease has a specific charge dependence.
- A detailed p_T dependence of the projectile component in p+C collisions in comparison to p+p collisions has been established. Around mean transverse momentum this comparison is characterized by important, charge dependent structures. A general increase with transverse momentum is observed for multiple collisions.
- This increase is quantified by an enhancement factor which has a strong x_F dependence. The enhancement factor is corrected for the target contribution and single collisions which don't contribute to the enhancement.
- The relation to the anomalous nuclear enhancement (Cronin effect) is established and it is demonstrated that a new assessment of this phenomenon is mandatory from a purely experimental point of view.
- The resonance decays are very important for pion production, including "high p_T".

Chapter 10

Summary of the main achievements and results of the present study

The main results presented in the thesis can be summarized as follows:

1. dE/dx calibration of the TPCs in p+C collisions has been performed which includes corrections of the measured cluster charges for time dependence, track angles, drift lengths, magnetic effects and sector constants, and forming of the truncated mean value for each measured track.

2. Data sets of inclusive double differential cross sections of pions in p+p and minimum bias p+C collisions as a function of x_F and p_T at 158 GeV/c beam momentum have been obtained. These data sets are unprecedented in terms of phase space coverage and precision.

   Measured cross sections in p+p reaction cover range of $0 < p_T < 2$ GeV/c and $0 < x_F < 0.85$. The data are obtained by a sample of 4.8 million inelastic events. The statistical and systematic uncertainties are well below 5% which allows for the first time to observe local structures in both x_F and p_T distributions.

   In p+C reaction a sample of 377 000 inelastic events has been used. The data cover phase space ranging from 0 to 1.8 GeV/c in p_T and from -0.1 to 0.5 in x_F. The statistical uncertainties are on the level of few percent and systematic errors are less than 8%. As in p+p case local structures are found.

   The measured cross sections have been parametrized as a function of x_F and p_T. These parametrizations have been used for determination of p_T integrated yields quantities, like invariant and non-invariant yields as a function of x_F, first and second moments of the p_T distributions.

3. The double differential cross sections and p_T integrated yields has been compared with available measurements. Systematic deviations (up to 5σ) between the NA49 data and some of the previous results have been found.

4. The total inelastic cross section in p+p and p+C reactions have been measured:

$$\begin{aligned} \sigma_{\text{inel}}^{\text{pp}} &= 31.46\ mb \pm 1\% \\ \sigma_{\text{inel}}^{\text{pC}} &= 226.3\ mb \pm 2.5\%, \end{aligned}$$

   which are in good agreement with previous results.

5. The p_T integrated distributions of pions in p+C collisions as a function of x_F have been studied in comparison to p+p interactions. The following conclusions can be drawn:

   – It has been clearly established that pion fragmentation in p+p reaction is composition of two independent components: projectile fragmentation and target fragmentation. These components have been isolated and quantified. They overlap in the central region as the overlapping range is limited to $|x_F| = 0.1$.

   – In addition to these two components there is a third component in p+C collisions, intranuclear cascading, generated by the propagation and interaction of the participating nucleons and secondary hadrons inside the nucleus. These components have been isolated and quantified.

   – In p+C collisions the π^+/π^- ratio reaches one at x_F = -0.1 which can be expected from the isoscalar nature of carbon nucleus.

   – The measured total pion yield from the target fragmentation in p+C collisions corresponds on an average to 1.6 participating nucleons. This value is significantly below (4σ) the expected mean number of collisions of 1.68 from measured nuclear parameters.

   – The ratio between p_T integrated yield in p+C and p+p collisions for charged pions reveals a charge dependence, reflecting the isospin composition of the nucleus.

   – Above $x_F \sim 0.2$ pion yield in p+C interactions decreases steadily with respect to elementary collisions.

6. The pion production in p+C collisions have been studied as a function of p_T in comparison to p+p interaction. The results can be summarized as follows:

   – A general increase at high p_T in p+C collisions is observed for the full x_F range. This increase is quantified by an enhancement factor which has a strong x_F dependence. The enhancement factor is corrected for the target contribution and single collisions which don't contribute to the enhancement.

   – The anomalous nuclear enhancement (Cronin effect) is measured as a function of x_F for the first time. It is demonstrated that new approach to this phenomenon is mandatory from a purely experimental point of view.

Acknowledgements

I would like to thank my Supervisor Assoc. Prof. Dr. Leandar Litov for his enormous support, patience and help throughout the time of my graduate study. I also appreciate very much his goodwill and priceless assistance during the months of completion of the presented work, as well as the great effort he invested in helping me to consolidate my thesis into a reasonable shape. I want to thank Dr. L. Litov for the warm friendly atmosphere that he created in our common work.

My warmest thanks go to Prof. Matey Mateev who together with my Supervisor have given me the opportunity to participate in an international collaboration and work at CERN. I want to express my deep gratitude to Prof. Mateev for his inspiring guidance, inestimable help during my study. I am also very thankful to his continuous support during all the years of working together.

I wish to express my gratitude to Dr. Hans Gerhard Fischer for continuous scientific support, very interesting and challenging discussions. As a leader of NA49 proton group he has created an incredible working atmosphere. Without his valuable advices this work will not be possible.

I am very thankful to other members of proton group, especially Siegfried Wenig, Dezso Varga, Ondrej Chvala, Andrzej Rybicki, Latchezar Betev and Zoltan Fodor for their help and support at any stage of this work.

I am very grateful to all the members of the High Energy Physics group in the University of Sofia for their help, patience and wonderful atmosphere. Special thanks to Venelin Kozhuharov, Zhechka Toteva and Georgi Petrov. They always help me when I needed.

I want to thank to my family and friends, especially to my parents for their moral support and patience.

List of Figures

List of Tables

Bibliography

[1] C. Alt et al., *Inclusive production of charged pions in p+p collisions at 158 GeV/c beam momentum*, Eur. Phys. J. **C45** (2006) 343

[2] C. Alt et al., *Inclusive production of charged pions in p+C collisions at 158 GeV/c beam momentum*, Eur. Phys. J. **C49** (2007) 897

[3] G. Barr et al., *Charged pion production in p+C collisions at 158 GeV/c beam momentum: discussion*, Eur. Phys. J. **C49** (2007) 919

[4] S. Afanasiev et al. [NA49 Collaboration], Nucl. Instrum. Meth., **A430** (1999) 210

[5] K. Fiałkowski and W. Kittel, Rep. Prog. Phys. **46** (1983) 1283

[6] C. Bovet et al., Yellow Report CERN 81-13 (1982)

[7] I. Otterlund et al., Nucl. Phys. **B198** (1987) 407

[8] A. Ferrari et al., Z. Phys. **C71** (1996) 75

[9] M. K. Hegab and J. Hüfner, Nucl. Phys. **A384** (1982) 353

[10] K. Braune et al., Z. Phys. **C13** (1982) 191

[11] L. Landau, *On the energy loss of fast particles by ionization*, J. Phys, USSR, 8, (1944) 201

[12] G. Veres, *Baryon Momentum Transfer in Hadronic and Nuclear Collisions at the CERN NA49 Experiment*, PhD thesis

[13] A. Rybicki, *Charged hadron production in elementary and nuclear collisions at 158 GeV/c*, PhD thesis

[14] D. Varga, *Study of Inclusive and Correlated Particle Production in Elementary Hadronic Interactions*, PhD. Thesis (2003) Eötvös Loránd University, Budapest

[15] I. Lehraus, R. Matthewson, W. Tejessy *dE/dx measurement in Ne, Ar, Kr, Xe and pure hydrocarbons*, Nucl. Instrum. Meth. **200** (1982) 199-210

[16] H. Fischle et al., Nucl. Instrum. Meth. **A301** (1991) 202

[17] H. G. Fischer et al., Nucl. Phys. **A715** (2003) 118

[18] H. G. Fischer et al., Heavy Ion Phys. **17** (2003) 369

[19] G. J. Bobbink et al., Nucl. Phys **B204** (1982) 173

[20] J. R. Johnson et al., Phys. Rev. Lett. **39** (1977) 1173
J. R. Johnson et al., Phys. Rev. **D17** (1978) 1292

[21] A. E. Brenner et al., Phys. Rev. **D26** (1982) 1497

[22] Y. Cho et al., Phys. Rev. Lett. **31** (1973) 413

[23] J. Erwin et al., Phys. Rev. Lett. **33** (1974) 1352

[24] W. M. Morse et al., Phys. Rev. **D15** (1977) 66

[25] D. Antreasyan et al., Phys. Rev. **D19** (1979) 764

[26] D. Brick et al., Z. Phys. **C13** (1982) 11

[27] J. L. Bailly et al., Z. Phys. **C35** (1987) 309

[28] M. Adamus et al., Z. Phys. **C39** (1988) 311

[29] M. Aguilar-Benitez et, al., Z. Phys. **C50** (1991) 405

[30] C. M. Bromberg et al., Nucl. Phys. **B107** (1976) 82

[31] C. M. Bromberg et al., Phys. Rev. **D9** (1974) 1864

[32] T. Kafka et al., Phys. Rev. Lett. **34** (1975) 687

[33] V. V. Aivazyan et al., Z. Phys. **C42** (1989) 533

[34] S. Uhlig et al., Nucl. Phys. **B132** (1978) 15

[35] D. Barton et al., Phys. Rev. **D27** (1983) 2580

[36] N. A. Nikiforov et al., Phys. Rev. **C22** (1980) 700

[37] A. Carroll et al., Phys. Rev. Lett. **33** (1974) 928

[38] A. Carroll et al., Phys. Lett. **61B** (1976) 303

[39] G. Bellettini et al., Nucl. Phys. **79** (1966) 609

[40] A. Carroll et al., Phys. Lett. **B80** (1979) 319

[41] B. Bobchenko et al., Sov. J. Nucl. Phys **30** (1979) 805

[42] S. Denisov et al., Nucl. Phys. **B61** (1973) 62

[43] A. Ashmore et al., Phys. Rev. Lett. **5** (1960) 576

[44] T. Sjostrand, Comp. Phys. Commun. **135** (2001) 238

[45] E. E. Zabrodin et al., Phys. Rev. **D52** (1995) 1316

[46] V. Blobel et al., Nucl. Phys. **B69** (1974) 454

[47] D. Brick et al., Nucl. Phys. **B164** (1980) 1

[48] T. Susa et al. [NA49 Collaboration], Nucl. Phys. **A698** (2002) 491

[49] S. Erhan et al., Phys. Lett. **85B** (1979) 449

[50] M. G. Albrow et al., Nucl. Phys. **B56** (1973) 333

[51] M. G. Albrow et al., Nucl. Phys. **B73** (1974) 40

[52] J. Singh et al., Nucl. Phys. **B140** (1978) 189

[53] A. Bertin et al., Phys. Lett. **38B** (1972) 260

[54] A. Bertin et al., Phys. Lett. **42B** (1972) 493

[55] M. Banner et al., Phys. Lett. **41B** (1972) 547

[56] L. G. Ratner et al., Phys. Rev. **D9** (1974) 1135

[57] P. Capiluppi et al., Nucl. Phys. **B70** (1974) 1

[58] M. G. Albrow et al., Phys. Lett. **42B** (1972) 279

[59] B. Alper et al., Nucl. Phys. **B100** (1975) 237

[60] K. Guettler et al., Phys. Lett. **64B** (1976) 111

[61] M. Banner et al., Nucl. Phys. **B126** (1977) 61

[62] R. D. Field and R. P. Feynman, Nucl. Phys. **B136** (1978) 1

[63] E. A. J. M. Offermann et al., Phys. Rev. **C44** (1991) 1096

[64] I. Sick, Phys. Lett. **116B** (1982) 212

[65] A. Rybicki, H.Niewodniczański Institute of Nuclear Physics, Internal Report No 1976/PH, http://www.ifj.edu.pl/publ/reports/2006/

[66] J. Burfening et al., Phys. Rev. **75** (1949) 382

[67] H. Yagoda, Phys. Rev. **85** (1952) 891

[68] E. M. Friedländer, Phys. Lett. **2** (1962) 38

[69] N. I. Kostanashvili et al., Sov. J. Nucl. Phys. **13** (1971) 715

[70] A. Abduzhamilov et al., Phys. Rev. **D39** (1989) 86

[71] M. Della Negra et al., Nucl. Phys. **B127** (1977) 1

[72] R. P. Feynman et al., Phys. Rev. **D18** (1978) 3320

[73] J. J. Gaardhøje et al., Eur. Phys. J. **C43** (2005) 287

[74] B. Z. Kopeliovich et al., Phys. Rev. **C72** 054606

[75] J. Kühn, Phys. Rev. **D13** (1976) 2948

[76] A. Krzywicki et al., Phys. Lett. **B85** (1979) 407

[77] M. Lev and B. Petersson, Z. Phys. **C21** (1983) 155

[78] A. Accardi, hep-ph/0212148 (2003)

[79] B. Kopeliovich et al., Phys. Rev. Lett. **88** (2002) 232303

[80] U. Amaldi et al., Nicl. Phys. **B86** (1975) 403

[81] A. Breakstone et al., Z. Phys. **C21** (1984) 321

[82] H. G. Fischer et al., CERN/SPSC 2005-035

[83] D. Drijard et al., Nucl. Instrum. Meth. **225** (1984) 367